INFORMATION TO USERS

UNIVERSITY of CALIFORNIA
Santa Barbara

Dissipation of THz frequency intersubband plasmons in quantum wells

A dissertation submitted in partial satisfaction of the
requirements for the degree of

Doctor of Philosophy

in

Physics

by

Jon Brett Williams

Committee in charge:

Professor Mark Sherwin, Chair
Professor John Ruhl
Professor Leon Balents

December 2000
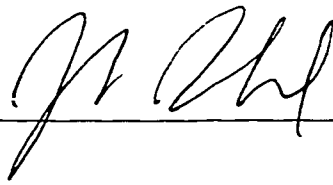
UMI Number: 3020316

UMI®
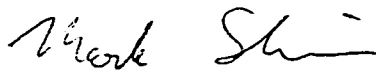
The dissertation of Jon Brett Williams is approved:

_____

_____

_____
Chair

December 2000

Dissipation of THz frequency intersubband plasmons in quantum wells

Copyright 2000

by

Jon Brett Williams

To Laura

Acknowledgements

The author's thesis advisor, Professor Mark Sherwin, is thanked for his support and guidance, and for always acting in the best interests of his students.

Thanks to the people who taught me when I first started in the lab, especially Keith Craig. I also enjoyed working in the lab with Frank Hegmann, Bryan Cole, and Tom King, even if they are un-American and probably communists.

Thanks to Mark Su for many stimulating conversations, some of which related to physics.

Many late nights in the lab were made possible by deliveries from Rusty's Pizza Parlor (564-1111).

Thanks to the staff of the Physics department and the Quantum Institute, especially Glenn "Brainwashed by Microsoft" Schiferl, Mike Wrocklage, Dave Enyeart, Dean White, Kathy Upton, Shilo Creek, Brian Wolf, Jeff Gramme, Sara Kazeroni, and Stacey Sauber.

Thanks to Ken Campman, Kevin Maranowski, Christoph Kadow and Professor Art Gossard, for providing me with samples and for useful discussions about my results. Thanks to Carey Cates for giving me several chunks of her wide quantum well wafer for the measurements described herein.

To the new generation of students, Kohl Gill, Nathan Jukam, Matt Doty, and Sam Carter: good luck, and don't spend as long in grad school as I did.

Thanks to Mom, Dad, and Robin for their love and encouragement throughout my life.

Finally, thanks to Laura Brugman. I could write another dissertation about what she means to me... but one is enough.

.

Curriculum Vitæ

Jon Brett Williams

Personal

Born

May 19, 1972

Washington, D.C.

Education

1985–1989

Foothill High School

Santa Ana, California

1989–1993

B.S. in Physics

University of California

Irvine, California

Professional

1993–1994

Teaching Assistant, Dept. of Physics

University of California, Santa Barbara

1994–2000

Research Assistant, Dept. of Physics

University of California, Santa Barbara

Publications

K. Craig, B. Galdrikian, J. N. Heyman, A. G. Markelz, J. B. Williams, M. S. Sherwin, K. Campman, P. F. Hopkins, and A. C. Gossard. Undressing a collective intersubband excitation in a quantum well. *Physical Review Letters* **76**, 2382 (1996).

J. N. Heyman, K. Unterrainer, K. Craig, J. Williams, M. S. Sherwin, K. Campman, P. F. Hopkins, A. C. Gossard, B.

N. Murdin, and C. J. G. M. Langerak. Far-infrared pump-probe measurements of the intersubband lifetime in an Al-GaAs/GaAs coupled-quantum well *Applied Physics Letters* **68**, 3019 (1996).

F. A. Hegmann, J. B. Williams, B. Cole, M. S. Sherwin, J. W. Beeman, and E. E. Haller. Time-resolved photoresponse of a gallium-doped germanium photoconductor using a variable pulse-width terahertz source. *Applied Physics Letters* **76**, 262 (2000).

J. B. Williams, K. Craig, M. S. Sherwin, K. Campman, and A. C. Gossard. Measurements of far-infrared intersubband absorption linewidths in GaAs/AlGaAs quantum wells as a function of temperature and charge density. *Physica E* **2**, 177 (1998).

J. B. Williams, M. S. Sherwin, K. D. Maranowski, C. Kadow, and A. C. Gossard. Linewidth of THz intersubband transitions in GaAs/AlGaAs quantum wells. *Proceedings of SPIE* **3617**, 126 (1999).

J. B. Williams, M. S. Sherwin, K. D. Maranowski, C. Kadow, and A. C. Gossard. Linewidth and Dephasing of THz-Frequency Collective Intersubband Transitions in a GaAs/AlGaAs Quantum Well. *Physica E* **7**, 204 (2000).

B. E. Cole, J. B. Williams, M. S. Sherwin, and C. R. Stanley. Coherent Optical Manipulation of Semiconductor Quantum

Bits. In preparation.

J. B. Williams, M. S. Sherwin, K. D. Maranowski. and A. C. Gossard. Dissipation of intersubband plasmons in wide quantum wells. In preparation.

Field of Study

Major Field: Experimental Condensed-Matter Physics

Study of intersubband transitions in quantum wells.
Professor Mark Sherwin

Abstract

Dissipation of THz frequency intersubband plasmons in quantum wells

by

Jon Brett Williams

In a doped quantum well, confinement of electrons breaks the continuum of conduction band states into subbands. The optically-excited intersubband (ISB) excitation is known to be a collective mode of the 2D electron gas (2DEG), the ISB plasmon. The ISB plasmon can be thought of as a coherent superposition of single-particle intersubband excitations, with an energy renormalized from the bare intersubband spacing by Coulomb and exchange effects. In the absence of processes like phonon emission, which remove energy from the electron gas, the width of a homogeneously-broadened ISB absorption line is solely determined by the rate at which the collective mode dissipates into other modes of the 2DEG. Both disorder and a recently proposed intrinsic viscosity of the 2DEG are expected to contribute to the ISB plasmon's dissipation.

For GaAs quantum wells with transitions in the THz, far below the optical phonon energy, the ISB linewidth should be dominated by dissipation. This dissertation describes measurements of the linewidth and mobility of THz-frequency ISB excitations in GaAs quantum wells as a function of the charge density and electric field. The field-dependence indicates that the absorption line is homogeneously broadened, and thus determined by scattering. Surprisingly, the linewidth and the mobility respond differently to the same scattering mechanisms. The linewidth is dominated by interface roughness scattering, while the mobility is dominated by bulk impurity scattering. A new microscopic theory of the linewidth agrees well with the data.

Contents

Chapter 1

Introduction and motivations

Semiconductor heterostructures are artificial solid structures grown one atomic layer at a time by molecular beam epitaxy. By alternating the composition of the layers as the growth proceeds, one can tailor the electronic structure of the solid. Thus one has the unique ability to create solids which have electronic behavior which is not otherwise found in nature. Semiconductor heterostructures have found widespread practical applications, for example ultrafast transistors, lasers, and infrared detectors. There is also some promise that heterostructure lasers and detectors may be made to operate in the THz, where existing technology is relatively crude and new devices are needed.

The heterostructure also is an ideal system for studying some basic physics. It is known that electronic intersubband excitations are a collective phenomenon, and the collective nature influences the optical properties of the system. One can vary the conditions in a heterostructure by application of gate voltages, adding or removing charge and changing the shape of the electronic wavefunctions by application of an electric field, all in a single sample. This gives us a lot of knobs to turn, so to speak, and means that we can really give many-body theory a thorough experimental test.

This chapter gives just enough of an introduction to the experimental system and the basic physics to put the thesis work in context and motivate the rest of

1
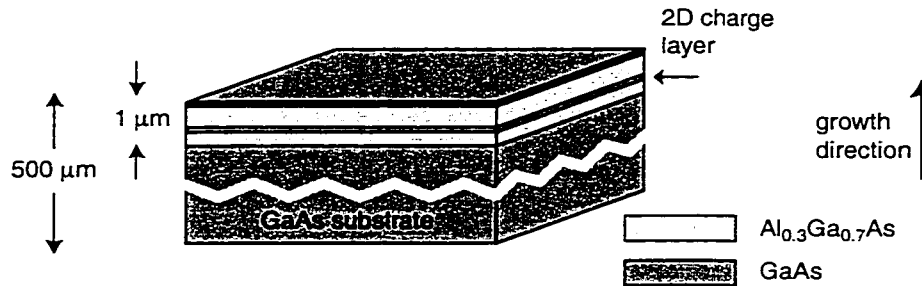
Figure 1.1: An MBE-grown sample.

the thesis.

1.1 Sample growth

The samples studied were grown by molecular beam epitaxy (MBE) in Professor Gossard's group here at UCSB. This growth technique allows one to engineer the electronic behavior of the solid by growing samples one atomic layer at a time, varying the composition as the growth proceeds (see Figure 1.1). Growers can make samples with a spatially varying bandgap and doping profile, which has led to the invention of many useful devices, and to the discovery of interesting new physics.

A very basic type of device grown by MBE is the semiconductor quantum well, in which a lower bandgap material is sandwiched between two layers of larger bandgap. This "quantum well" acts as a one-dimensional potential well. The sample may be doped, so that electrons added to the conduction band are confined to the quantum well.

1.2 Basic physics

Excess electrons in the conduction band fall in to the attractive potential of the quantum well. The electrons feel the potential of each atom in the lattice,
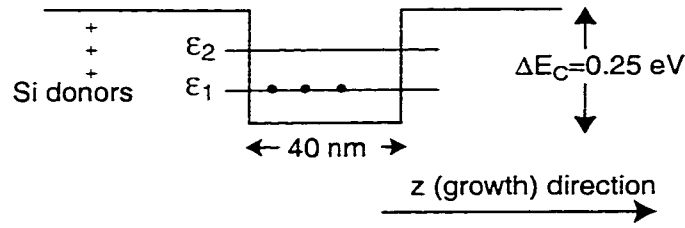
Figure 1.2: Energy levels in the 1D well

of course, but the validity of the envelope function approximation allows the details of the lattice structure to be swept under the rug [3]. In this approximation, the electrons behave as though they only experience the one-dimensional potential given by the position-dependent conduction band edge, and the details of the underlying crystal lattice only manifest themselves in an effective electron mass, m^*. Neglecting electron-electron interactions, a single electron obeys the Schrödinger equation of the form

$$\left[-\frac{\hbar^2}{2m^*}\nabla^2 + V(z) \right] \psi(x,y,z) = E\psi(x,y,z)$$

The z-dependent part of this equation can be separated from the in-plane part. The electron wavefunction is given by

$$\psi(x,y,z) = e^{i\mathbf{k}\cdot\mathbf{r}}\chi_n(z)$$

where $\mathbf{r}$ is the in-plane position vector, $\mathbf{k}$ is the in-plane wavevector, and $\chi_n(z)$ is the eigenfunction (with quantum number n and eigenvalue ε_n as shown in Figure 1.2) of the z-dependent part of the one-dimensional Schrödinger equation. The single-electron states thus have energies given by:

$$E_{n,k} = \frac{\hbar^2 k^2}{2m^*} + \varepsilon_n$$

The set of all states with the same quantum number n is called a subband (see Figure 1.3).
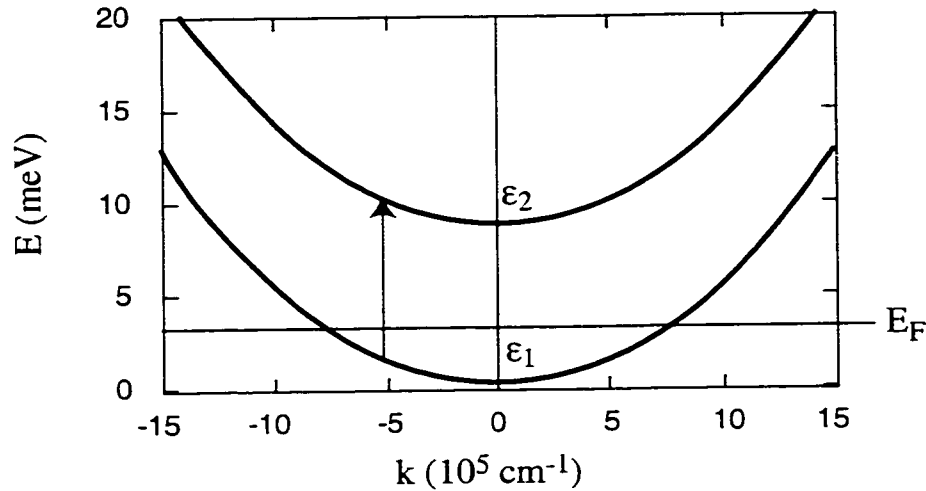
Figure 1.3: Electronic subbands

1.3   Intersubband transitions

One can excite electronic transitions between subbands of different index n by driving the electrons with a light field polarized in the growth direction. A typical absorption spectrum is plotted in Figure 1.4. Infrared photons have small wavevector, and thus excite transitions with essentially zero momentum change. The energy of the transition, in the absence of electron-electron interactions, is given by the subband spacing. It turns out that when an infrared photon is absorbed, a collective excitation is created rather than a single particle excitation. This collective mode is known as the intersubband plasmon, which is a coherent superposition of single-particle intersubband excitations. The absorption thus has a peak at the plasmon energy, which is blue-shifted from the bare intersubband splitting (by an amount called the depolarization shift).

Theoretical work in understanding the physics of intersubband plasmons is ongoing. One aspect that is not yet understood is what determines the absorption linewidth. The measurements described in this dissertation indicate that the ab-
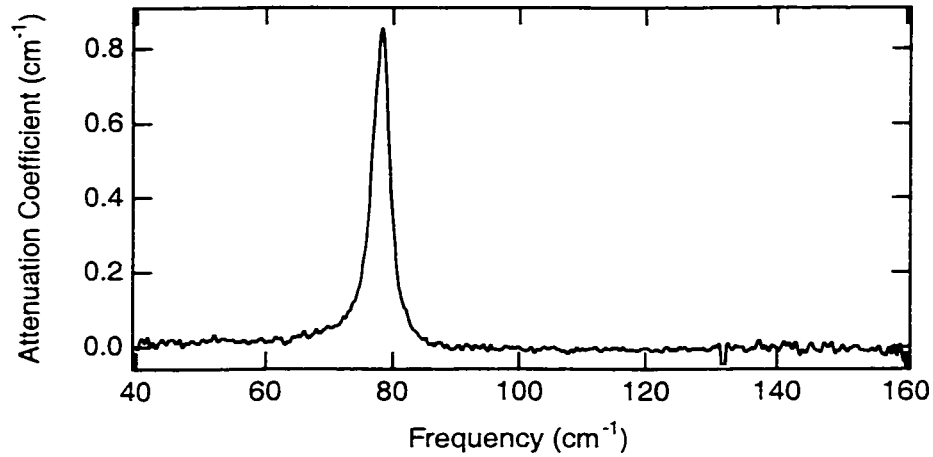
Figure 1.4: Typical absorption spectrum.

sorption line is homogeneously broadened (i. e. not due to sample inhomogeneities), and therefore the linewidth tells us something intrinsic about the nature of collective electronic excitations.

Specifically, the homogeneous linewidth is proportional to the rate at which the intersubband plasmon relaxes. This relaxation may be either by an inelastic process that takes energy out of the electron gas, e. g. phonon emission, or by an elastic process in which the plasmon dissipates into other modes of the electron gas. The term "dissipation" is used here to mean this process of elastic relaxation.

This dissertation describes detailed measurements of the linewidth as a function of the charge density and electric field. The density and field were independently varied in backgated samples. These measurements allow one to examine how the linewidth was affected by types of disorder in the system. The disorder in the well is primarily due to roughness at the interfaces and to bulk impurities distributed throughout the well. The degree of disorder experienced by an electron thus depends on its position in the well. The shape and location of the electron distribution is changed by the application of an electric field. Thus, by varying the electric field,

the effects of disorder were examined. To compliment the mobility measurements, the mobility was calculated and compared to the data.

A new microscopic theory of the linewidth has been developed by Carsten Ullrich and Giovanni Vignale [20, 19]. The measured linewidths have been used by Carsten and Giovanni to test their theory.

1.4 Applications

ISB transitions are the basis of several types of devices with important practical applications, for example the quantum well infrared photodetector (QWIP) and the quantum cascade laser. These devices currently operate in the mid-IR, but work is in progress to make similar devices which work at THz frequencies [18, 5. 2, 17, 23]. An important parameter of all of these ISB-transition based devices is the linewidth of the transition. For detectors, the linewidth affects the resolution and the bandwidth. For lasers, the linewidth is inversely proportional to the peak gain. So a better understanding of what broadens the line, and how to control the linewidth, will help designers optimize device performance.

Chapter 2

Basic physics of the intersubband excitation

This chapter extends the discussion of the previous chapter, to discuss the physics in enough detail that we can understand the results and their significance.

2.1 Excitations of the 2DEG

Electron-electron interaction effects have a significant effect on the inter-subband transition. The absorption of an infrared photon excites a collective mode of the electron gas, the intersubband plasmon. It is more useful to look at an excitation spectrum than at a spectrum of single particle states, because we can put both single particle and many body excitations on the same graph.

Figure 2.1 is a plot of the excitation energy as a function of magnitude of the in-plane wavevector. Both intrasubband and intersubband single-particle excitations are indicated, in the shaded regions. The plasmons are also shown. In addition to the standard 2D plasmon, there are plasmon-like excitations which involve intersubband transitions, which are the intersubband plasmons. There is one branch for each type of single-particle intersubband transition. In this work, only the lowest subband was
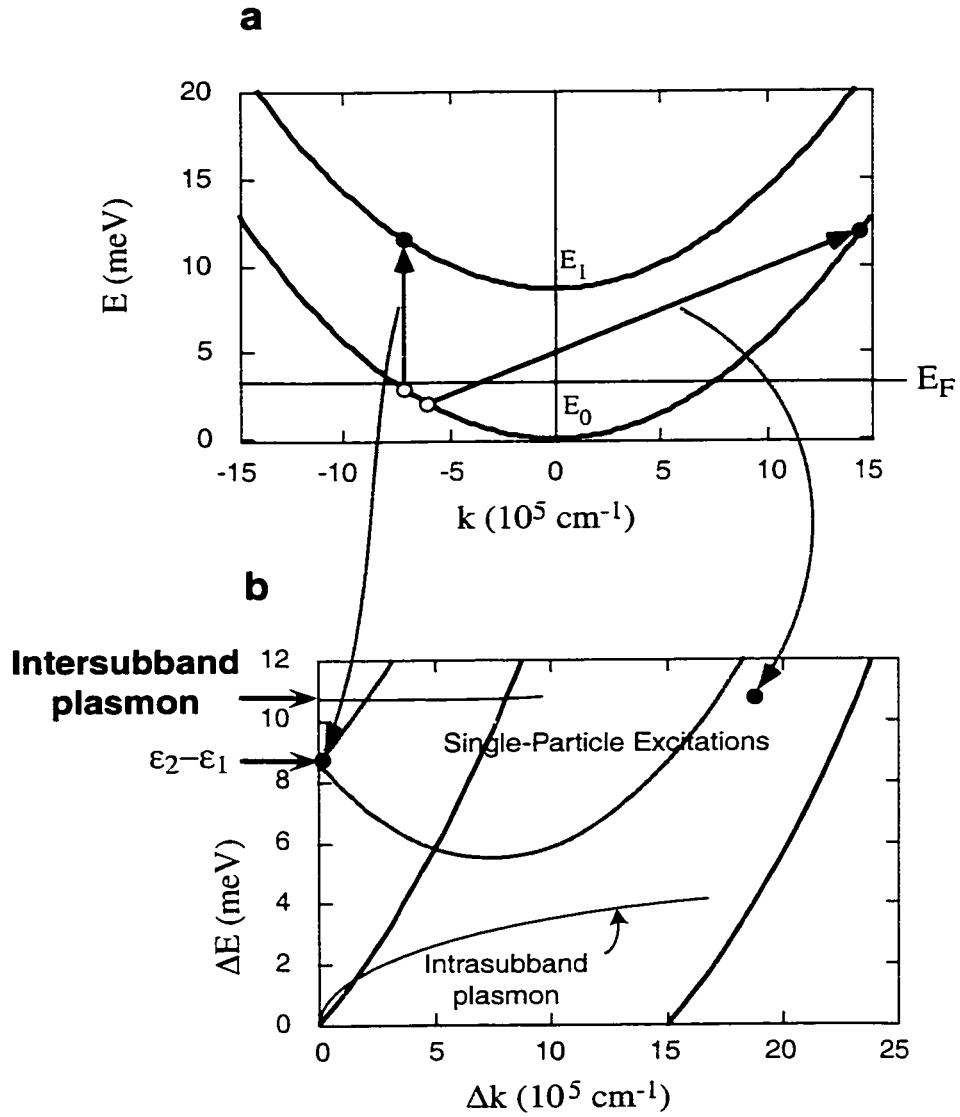
Figure 2.1: a) Single-particle states. b) Excitations of the 2DEG. Both single-particle and collective excitations (the plasmons) are shown.

occupied, so only $1 \rightarrow n$ intersubband plasmons could in principle be excited. We examined the $1 \rightarrow 2$ intersubband plasmon.

Infrared measurements excite plasmons at k=0 because of the small momentum of infrared photons. Dissipation is thought to be due to elastic scattering of the k=0 plasmon into single-particle modes at non-zero wavevector. Although infrared measurements do not directly probe such momentum-dependent phenomena, they do have advantages for basic physics (and they are the most relevant measurement for device applications anyway). It is experimentally more convenient to make detailed measurements of the properties of the k=0 plasmon in the infrared. because we can easily put gates on the sample so that we can vary the charge density and charge distribution in the sample, and we can readily do waveguide measurements to increase the absorption strength.

2.2 Previous studies of the linewidth

Most of the existing experimental work has been done on narrow wells less than 10 nm wide, which have transition energies in the mid-IR ($\sim$ 100 meV). Here, rapid emission of $\sim$36 meV optical phonons contributes to the ISB linewidth [13, 4, 9, 21], along with various types of disorder scattering. Because of ionized impurity scattering, the mid-IR ISB linewidth has been found to be larger for quantum wells doped in the well than in remotely-doped quantum wells [8]. In remotely-doped quantum wells, the mid-IR ISB linewidth is relatively insensitive to alloy disorder (which does degrade the mobility), but increases with decreasing well-width [4]. The dependence on well-width is consistent with a linewidth dominated by interface roughness (IFR) scattering. Experiments on InAs quantum wells show linewidths much smaller than would be expected based on non-parabolicity in a single-particle picture [21], and a very weak dependence on temperature [21], indicating the importance of the collective nature of the intersubband transition.

For wide GaAs quantum wells, with transitions far below the optical phonon

energy, the physics is much simpler than in narrow quantum wells. At low temperatures (for example 10K) optical phonon emission is energetically forbidden and acoustic phonon emission is two orders of magnitude slower [14] than relevant time scales. Non-parabolicity is also negligible. The homogeneous linewidth of the ISB plasmon is thus a measure of the how quickly the plasmon dissipates. This dissipation is expected to be purely determined by scattering from disorder, and perhaps a recently-suggested intrinsic (i. e. not related to disorder) contribution arising from the viscosity of the electron gas [20, 19]. (Calculations using this theory are shown in Chapter 6.)

Chapter 3

Sample design and processing

The fabrication of a 2D electron gas was mentioned in the first chapter. The particulars of the samples studied are discussed here.

3.1   Sample structures

A quantum well can be made with resonances in the THz by making it very wide, or by making two narrow wells coupled by a barrier (a "double well"), and both kinds are described in this dissertation. My first experiments on intersubband transitions were measurements of the temperature dependence of intersubband absorption in an asymmetric double square well sample with no backgate. (An asymmetric well was used rather than a symmetric well because the same design had been studied previously in other experiments in our group). These results are described in Chapter 5. This work led to measurements of a backgated double square well sample, because it appeared that independent control of the electric field and charge density in the well were required. These results are also described in Chapter 5.

The asymmetric double well measurements indicated that something interesting happens to the linewidth when the electric field in the well is zero ("flat-band"). However, the interpretation was complicated by the difficulty in determining when

11

the well was really at flat-band. This is because, in addition to the applied field, there is always some built-in field of unknown strength, which is due to fixed charges in the heterostructure. Thus, one could not predict at what value of the applied field the well was at flat-band. The only way to get an idea when the well is at flat-band is to look at the field-dependence of the absorption. This works nicely in a symmetric well: with a symmetric well, flat-band is the field at which the peak absorption frequency is a minimum. This is not the case in an asymmetric well (cf. Figures 3.6 and 3.3), so one would have to use careful simulations of the absorption frequency to tell from the data when the well was at flat-band. Clearly, the data from a symmetric well is easier to interpret.

A symmetric double square well sample could have been studied, but the ability to make a double well that is truly symmetric depends on how well one can control the growth rate. A single wide square well, on the other hand, is easier to make symmetric. Thus, I decided it was less ambiguous to study a single, wide, symmetric square well. The measurements on this sample are described in Chapter 6. Both types of samples are discussed in this chapter.

3.1.1 Asymmetric double quantum well

Several different asymmetric double quantum well samples were studied. The basic design of all of them was two wells, 75 Å and 85 Å in width, coupled by a 25 Å barrier. They differed in whether or not they had a backgate.

The first sample had no backgate. The MBE lab's name for the wafer was 950607A. My working name for the wafer was DSQC.

I also measured a backgated asymmetric double well that was grown for Gabriel Briceño, who was working on an intersubband-based THz detector. Gabriel's working name for the wafer was GB1.

The main backgated asymmetric double well is now described. The sample was grown by molecular beam epitaxy on a semi-insulating substrate. The grower
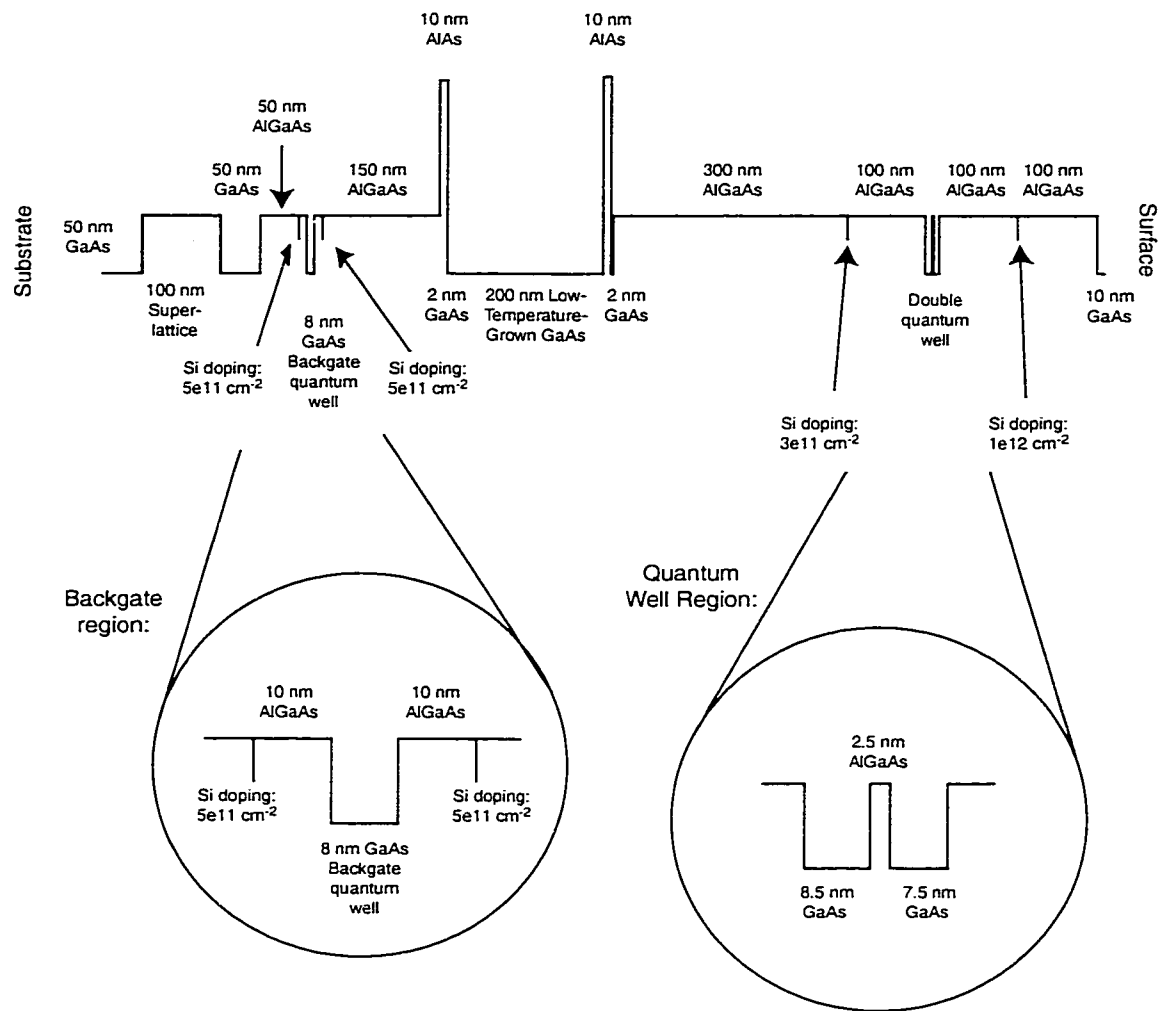
Figure 3.1: Conduction-band-edge diagram of the MBE-grown epilayer for the backgated double square quantum well sample (JW1).
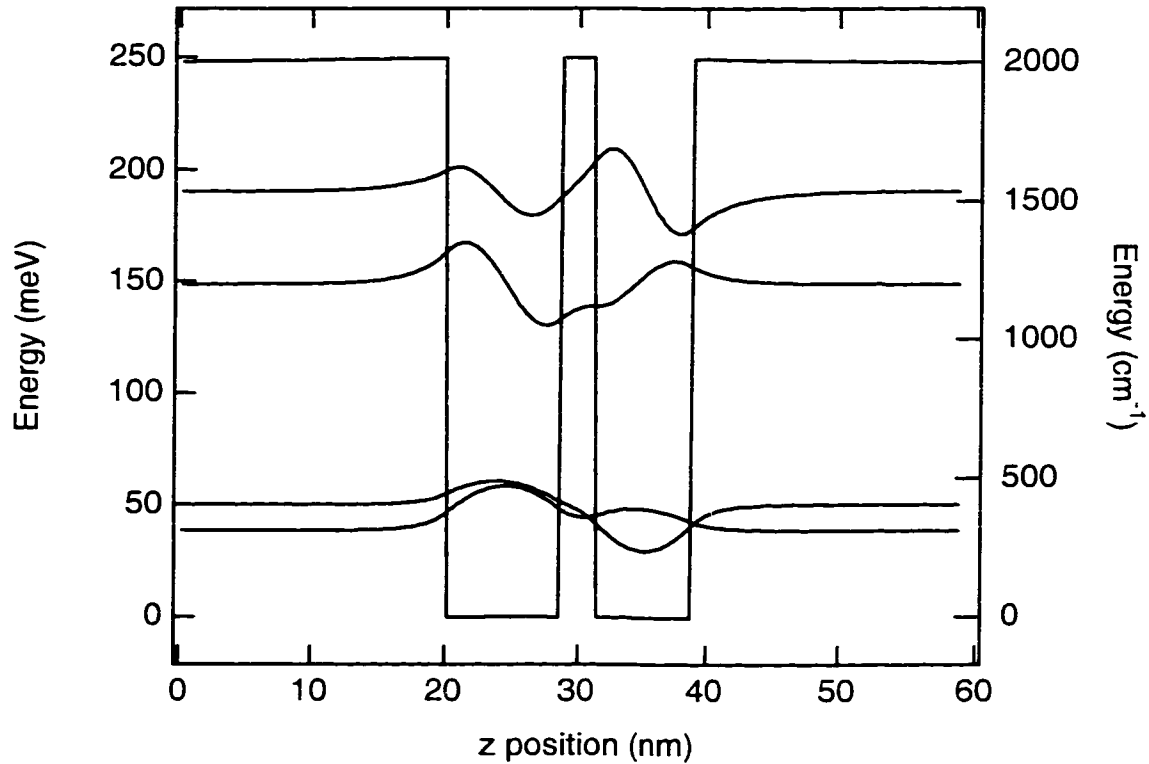
Figure 3.2: Self-consistent double square well and bound states for charge density $N_s = 10^{10}$ cm^{-2}. The states are vertically offset by their energy.

was Ken Campman, and the MBE lab's name for the wafer was 961023C. My working name for the wafer was JW1. A sketch of the conduction band is shown in Figure 3.1. The sample consists of 50 nm GaAs; 100 nm smoothing superlattice; 50 nm GaAs; 50 nm $Al_{0.3}Ga_{0.7}As$; Si delta-doped layer of charge concentration 5×10^{11}cm^{-2}; 10 nm $Al_{0.3}Ga_{0.7}As$; 8 nm GaAs quantum well backgate; 10 nm $Al_{0.3}Ga_{0.7}As$; Si delta-doped layer of charge concentration 5×10^{11}cm^{-2}; 150 nm $Al_{0.3}Ga_{0.7}As$; 10 nm AlAs; 2 nm GaAs; 200 nm low-temperature-grown GaAs; 10 nm AlAs; 2 nm GaAs (after which the wafer was annealed at 650 °C); 300 nm $Al_{0.3}Ga_{0.7}As$; Si delta-doped layer of charge concentration 5×10^{11}cm^{-2}; 100 nm $Al_{0.3}Ga_{0.7}As$ (digital alloy); 8.5 nm GaAs; 2.5 nm $Al_{0.3}Ga_{0.7}As$; 7.5 nm GaAs; 100 nm $Al_{0.3}Ga_{0.7}As$ (digital alloy); 100
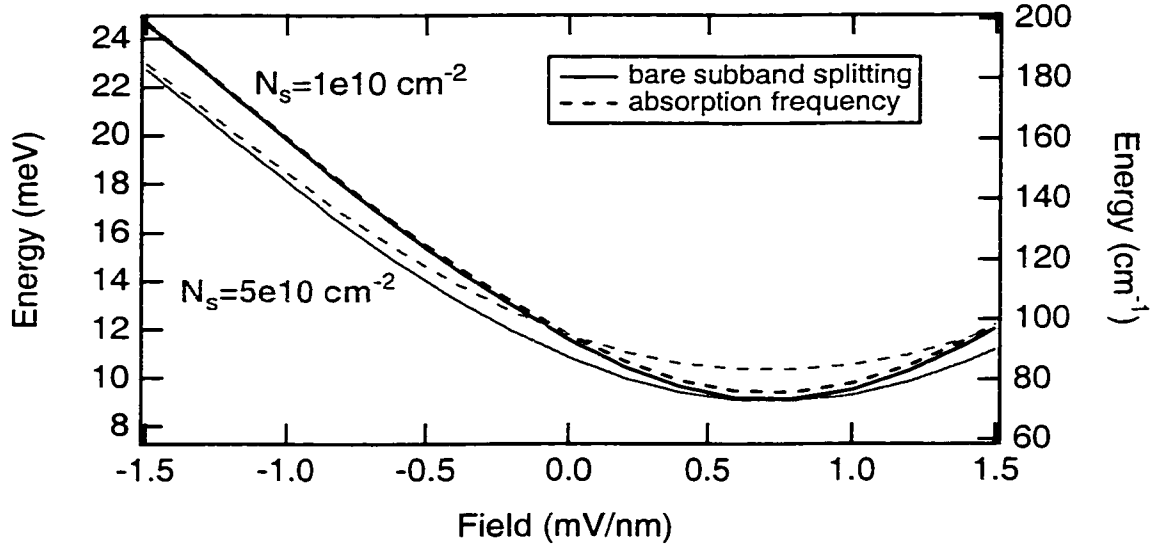
Figure 3.3: Calculated energy splitting of the lowest two subbands (solid curve) and intersubband absorption frequency (dashed curve) as a function of applied bias in the double square well, for charge density $N_s = 1 \times 10^{10}$ cm^{-2} (black) and $N_s = 5 \times 10^{10}$ cm^{-2} (gray).

nm $Al_{0.3}Ga_{0.7}As$; and a 10 nm GaAs capping layer. The backgate is a narrow, doped quantum well which is not optically active at the frequencies of interest, and was used to control the charge density in the double quantum well (hereafter, "the quantum well") via the field effect. The low-temperature-grown (LT) layer allows one to apply a voltage between the backgate and the quantum well at elevated temperatures. Without the LT layer, there would be significant conduction between the backgate and the quantum well at temperatures above about 10 K. Problems were experienced with the LT layer, which are discussed in Section 5.2.

There are several conduction subbands in the quantum well. Figure 3.2 shows the self-consistent well and bound states at flat-band (no electric field) and a charge density of $N_s = 10^{10}$ cm^{-2}, calculated with a program written by Bryan Galdrikian [11]. The energy separation of the lowest two subbands is field-tunable over a range of 10-20 meV. The energy separation of the lowest two subbands and

the intersubband absorption frequency is plotted vs. applied field in Figure 3.3. The absorption frequency is blue-shifted from the bare intersubband spacing by the depolarization shift, as discussed in Chapter 2. Note that both the subband splitting and the absorption frequency are asymmetric about zero field, and have a minimum at non-zero field. This means that if there is some built-in field in the well (and there usually is), it is difficult to tell when the sample is really at flat-band without careful modeling of the well.

In this work, only the lowest subband was occupied, and only transitions between the lowest two subbands were measured.

3.1.2 Wide quantum well

The sample was grown by molecular beam epitaxy on a semi-insulating substrate. The grower was Kevin Maranowski, and the MBE lab's name for the wafer was 980122A. My working name for the wafer was CC1. The substrate has a high resistivity so that it does not absorb the THz. A sketch of the conduction band is shown in Figure 3.4. The sample consists of 100 nm GaAs; 180 nm smoothing superlattice (30 periods of 3 nm GaAs, 3 nm $Al_{0.3}Ga_{0.7}As$); 100 nm $Al_{0.3}Ga_{0.7}As$; Si delta-doped layer of charge concentration $5 \times 10^{11} cm^{-2}$; 10 nm $Al_{0.3}Ga_{0.7}As$ barrier; 8.5 nm GaAs quantum-well backgate; a barrier and doping layer identical to the above; 490 nm $Al_{0.3}Ga_{0.7}As$; Si delta-doped layer of charge concentration $3 \times 10^{11} cm^{-2}$; 100 nm $Al_{0.3}Ga_{0.7}As$ barrier; 40 nm GaAs quantum well; 100 nm $Al_{0.3}Ga_{0.7}As$ barrier; Si delta doped layer of charge concentration $1 \times 10^{12} cm^{-2}$; 90 nm $Al_{0.3}Ga_{0.7}As$; and a 10 nm GaAs capping layer. The backgate is a narrow, doped quantum well which is not optically active at the frequencies of interest, and was used to control the charge density in the wide quantum well (hereafter, "the quantum well") via the field effect.

There are several conduction subbands in the wide quantum well. Figure 3.5 shows the calculated self-consistent well and bound states at flat-band (no electric field) and a charge density of $N_s = 10^{10}$ cm^{-2}, calculated with a program written
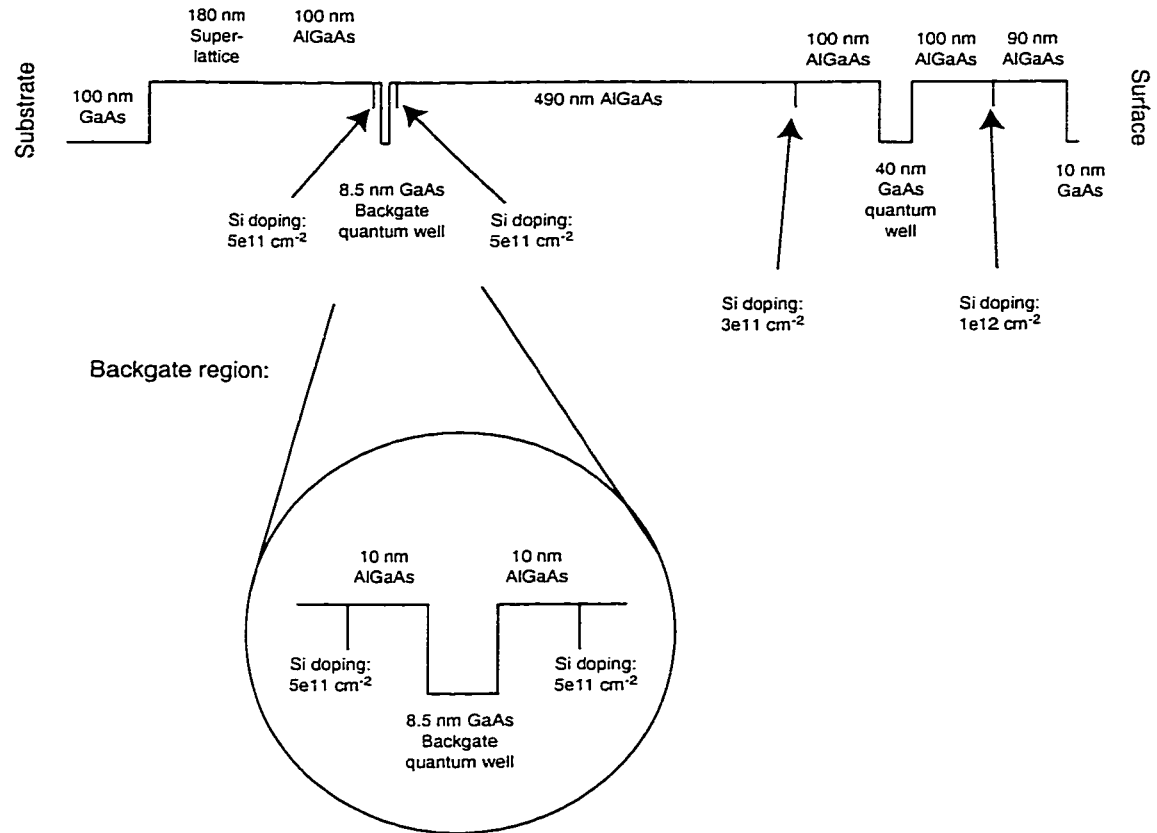
Figure 3.4: Conduction-band-edge diagram of the MBE-grown epilayer for the wide quantum well sample (CC1).
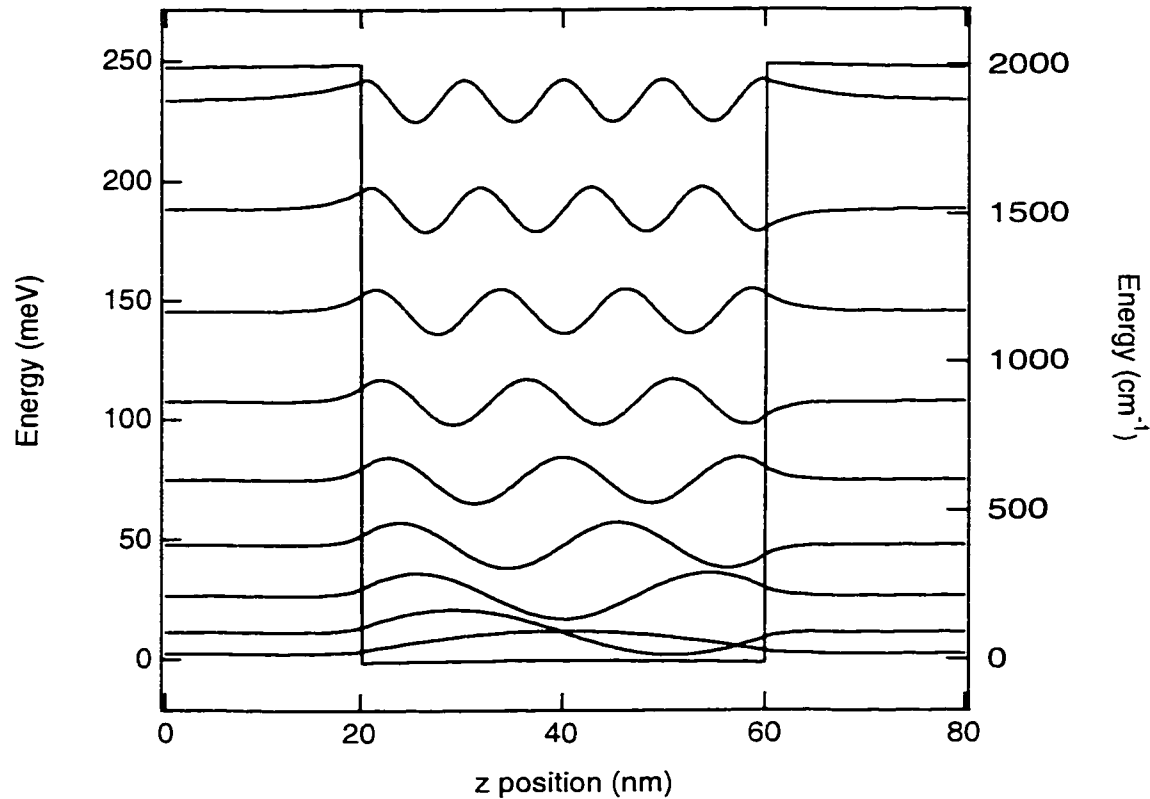
Figure 3.5: Self-consistent wide square well and bound states for charge density N_s = 10^{10} cm^{-2}. The states are vertically offset by their energy.

by Bryan Galdrikian [11]. The energy separation of the lowest two subbands is field-tunable over a range of 10-20 meV. The energy separation of the lowest two subbands and the intersubband absorption frequency are plotted vs. applied field in Figure 3.6. The absorption frequency is blue-shifted from the bare intersubband spacing by the depolarization shift, as discussed in Chapter 2. Note that both the subband splitting and the absorption frequency are symmetric about zero field, as we would expect for a symmetric well. Thus, even if there is a built-in field in the well, we can easily identify where the total field (applied plus built-in) is zero, i. e. the sample is at "flat-band," by finding the applied field that minimizes the absorption frequency.
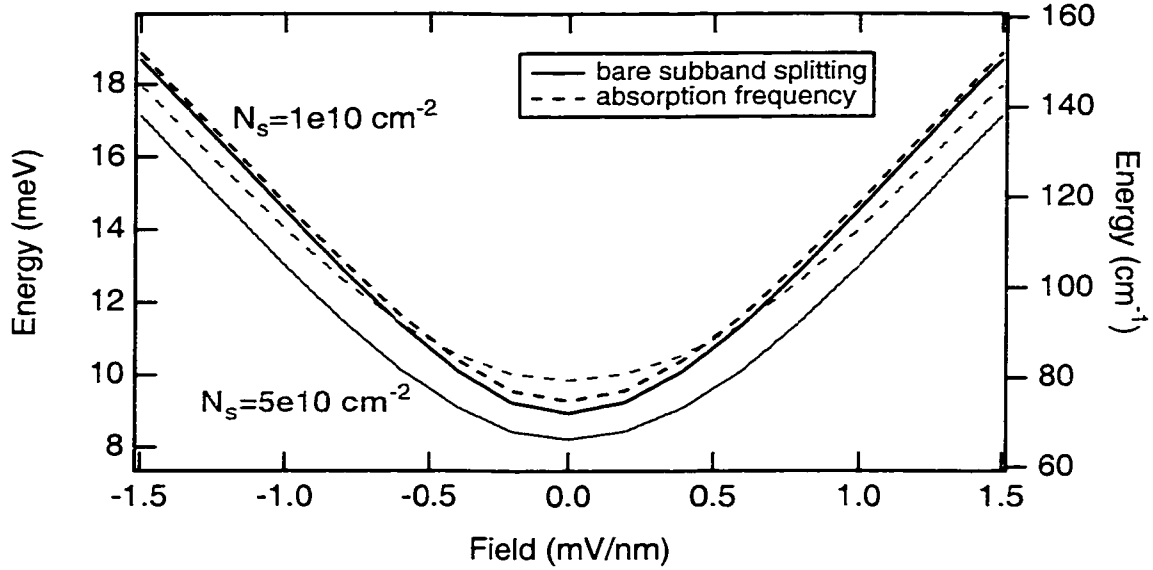
Figure 3.6: Calculated energy splitting of the lowest two subbands (solid curve) and inter-subband absorption frequency (dashed curve) as a function of applied bias in the wide square well, for charge density $N_s = 1 \times 10^{10}$ cm^{-2} (black) and $N_s = 5 \times 10^{10}$ cm^{-2} (gray).

In most of this work, only the lowest subband was occupied, and only transitions between the lowest two subbands were measured.

3.2 Processing the sample

After a wafer was grown, I would take it to the lab and cleave off a portion for the measurements. For the infrared measurements, I chose two opposing edges through which the light would be coupled and never touched these edges with anything hard enough to scratch or chip the sample, in order to keep edges smooth enough for clean coupling of the light. For the mobility measurements, I cleaved a second piece from a nearby spot on the wafer, with the hope that it is similar to the first piece. The sample is then brought to the cleanroom for making contacts to the charge layers.

The point of the cleanroom work is to make electrical contacts to the back-gate and the quantum well and to put a frontgate on the surface of the sample. (For non-backgated samples, omit parts of the process specific to backgates). In the case of the sample for mobility measurements, the first step was to etch a mesa in the surface of the sample, before making any of the contacts. In the case of samples for infrared measurements, I also put a layer of metal on the back side of the sample to form a waveguide. The processing recipes are given in Appendix A.

3.2.1   Ohmic contacts

The electrical contacts made to the well and the backgate have ohmic I-V characteristics. They needed to be electrically isolated from each other so that I could apply voltages between them. Ohmic contacts are formed by depositing a metal onto the surface of the sample, then annealing the sample at high temperature, to diffuse the metal into the sample.

The process for making contact to the backgate which is isolated from the quantum well is shown in Figure 3.7. It is discussed in more detail in Appendix A. I first made a photoresist mask and etched away the quantum well over a couple of small spots on the edge of the sample. The etch was stopped about 50 nm above the top doping layer of the backgate. I used a second photoresist mask to confine the backgate ohmic contact metal to an area within the etched region. [Note: I at first tried to etch areas in the sample and immediately deposit metal, using the same photoresist mask. It turns out that contacts made this way are always shorted to the quantum well, perhaps because the ohmic contact metal wets the side walls of the etch during the anneal, thus climbing up and contacting the quantum well.] The ohmic contacts for the backgate and quantum well are evaporated in the same step. The backgate ohmic contact metal is deposited within the etched away area. The quantum well ohmic contacts are evaporated directly onto the surface; no etch is required. After deposition and mask liftoff, I was left with squares of metal stuck to

a) Mask 1   b) Etch   c) Mask 2

d) Metallize   e) Liftoff   f) Anneal
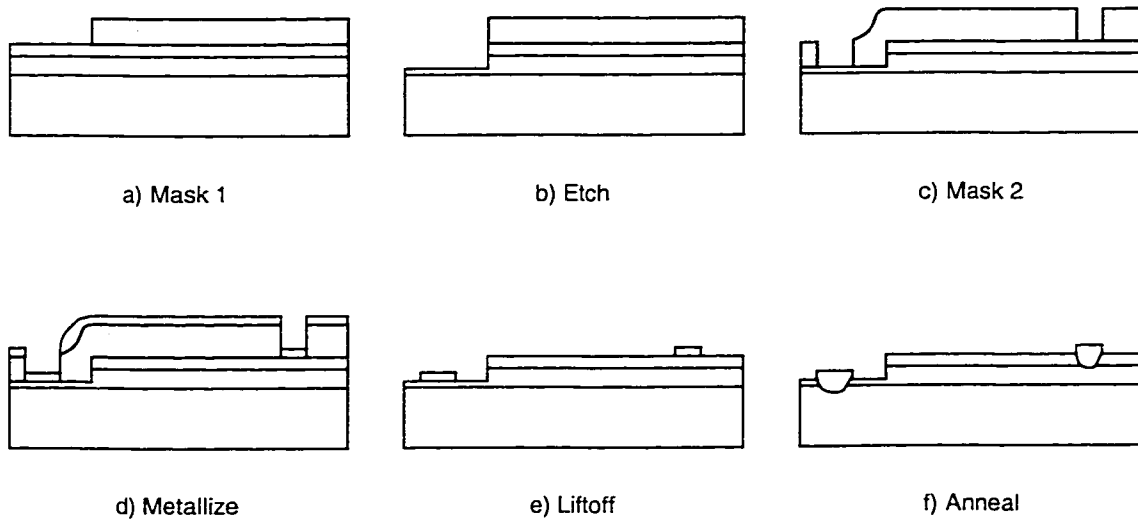
Figure 3.7: Process for making separate ohmic contacts to backgate and quantum well: a) Photoresist is spun on and an etch opening made for the backgate contact. b) The epilayer is etched down to just above the backgate. c) A second photoresist mask is made for the ohmic contact metallization. d) Ohmic contact metal is evaporated onto the sample. e) Photoresist is lifted off, leaving metal only for the ohmic contacts. f) The contacts are annealed to make contact to the buried charge layers.

the surface of the sample. The sample was annealed at high temperature to diffuse the metal into the sample. This process reliably makes contacts to the well with a resistance of order 1 kOhm which are ohmic for currents up to at least 10 μA, and which do not short the backgate to the quantum well at low temperatures.

3.2.2 Frontgate and backside metallization

The frontgate is a metal-semiconductor Schottky contact on the surface of the sample. It consisted of a 200 nm thick Al layer, evaporated onto the surface of the sample in a thermal evaporator at 5×10^{-7} torr, on a rectangular area covering the length of the sample. The Schottky contact has a diode-like I-V characteristic: I could apply negative voltages of large enough magnitude to deplete the quantum well, but I was limited to frontgate voltages less than about 1 V by the turn-on of
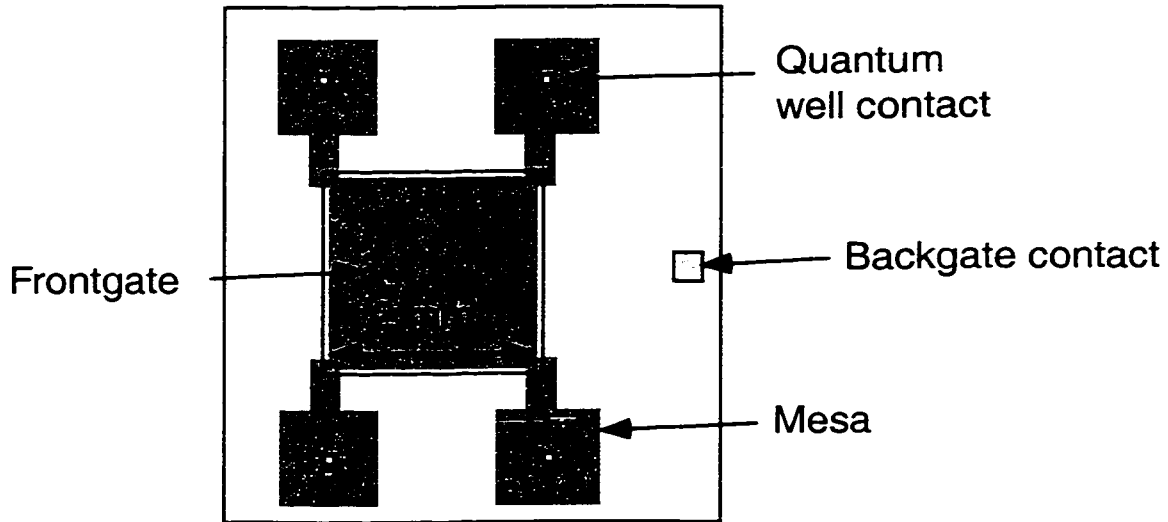
Figure 3.8: Sample used for mobility measurement.

current.

On the single wide square well, I also made some mobility measurements. The mobility sample was processed in the van der Pauw geometry [16], with a front-gate over an active region of dimensions 2mm × 2mm, as shown in Figure 3.8.

For the sample used in the infrared absorption experiments, another 200 nm thick layer of Al was evaporated onto the back side of the sample, so that the Al layers on both sides of the semiconductor sample form a parallel-plate waveguide (see Figure 3.9).
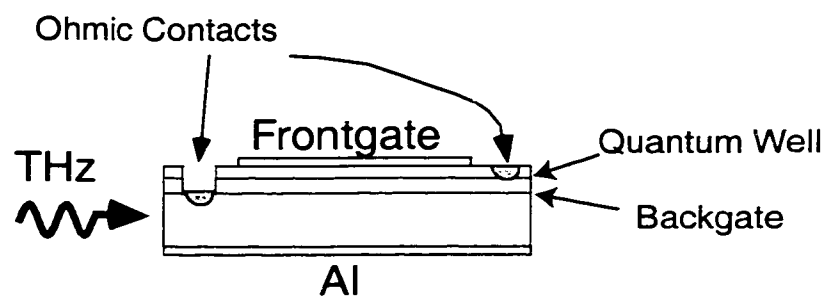
Figure 3.9: Sample used for infrared measurements.

Chapter 4

Measurement techniques

4.1 Controlling charge density and field in the back-gated samples

By separately controlling the voltages applied to the frontgate, quantum well, and backgate, the charge density in the well and the DC electric field at the well can be independently varied. The application of a negative frontgate bias tends to deplete the well, while adding an electric field across the well. The application of a negative *backgate* bias also tends to deplete the well, but adds an electric field of opposite sign. Thus by varying the two gate voltages together in the appropriate way, we can vary the charge density in the well while holding the field constant. Similarly, by varying the two gate voltages opposite to each other, we can vary the field in the well while holding the charge density constant. One does not have this capability in samples with only one gate: changing a single gate voltage always changes both the charge density and the applied field. It turns out that density and field effects in the linewidth are of the same magnitude, so it is critical to be able to separate out the two.

My measurements were among the first in our group on backgated samples,
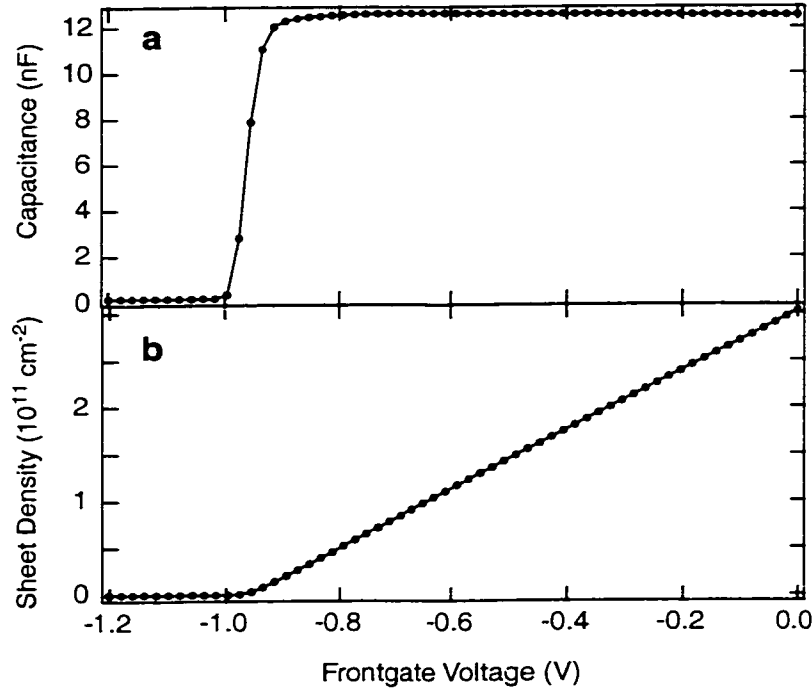
Figure 4.1: a) Typical measured C-V curve. b) Sheet density calculated from C-V data.

so here I describe in some detail how to determine the charge density and electric field as a function of the gate voltages, and how to vary the gate voltages together such that the either the density or electric field is held constant.

4.1.1 Charge density measurement

The charge density in the well was measured by integrating the gate-voltage-dependent capacitance (referred to as a "C-V" measurement). The frontgate and quantum well are two sheets of charge which form a parallel-plate capacitor. Using an AC technique, I measure this capacitance versus frontgate voltage, V_{fg}, while holding the backgate voltage fixed. The capacitance signal is equal to dQ/dV_{fg}, where Q is the charge in the quantum well. Below some sufficiently negative frontgate voltage

$V_{fg}^{-depl.}$, the well is depleted of charge, and the capacitance drops to zero. To find the total charge in the well at a certain frontgate voltage V_{fg}, I integrate the capacitance from $V_{fg}^{-depl.}$ to V_{fg}. This measurement is not sensitive to charges localized by disorder. By looking at the absorption strength as a function of measured sheet density, one can see that there is some charge left behind in the well even when the C-V indicates depletion, and we can estimate that the density of localized charges in the well is of the order $1 \times 10^{10} cm^{-2}$. To get the total density, this figure should be added to the density determined by the C-V measurement.

In talking about the charge in the well, I usually refer to either the charge density, which is the total charge divided by the measured frontgate area, or the sheet density, which is the number of electrons per unit area (charge density divided by e, the unit of electronic charge).

A typical C-V curve is shown in Figure 4.1a. The sheet density plotted in Figure 4.1b is given by

$$N_s(V_{fg}) = \frac{1}{eA} \int_{V_{fg}^{-depl.}}^{V_{fg}} C(V) \, dV \qquad (4.1.1)$$

where e is the charge of an electron, A is the frontgate area, and $V_{fg}^{-depl.}$ is a frontgate voltage for which the well is depleted, for example -1 V for the data in Figure 4.1. I assumed that any non-zero baseline in the capacitance data was due to a stray capacitance in parallel with the sample, so I subtracted the baseline.

To find the charge density as a function of both backgate and frontgate, this procedure is repeated for different values of the backgate voltage. A series of C-V curves at different backgate voltages is shown in Figure 4.2. One can see that increasing the backgate voltage puts more charge in the well, since the frontgate voltage at which the well depletes becomes more negative. (The strange behavior for $V_{bg} < -0.95$ V is discussed below).

In the wide square well sample, the capacitance was not constant even when the well was full. As shown in Figure 4.3, I could see some variation of the capacitance vs. frontgate voltage, especially at a certain frontgate voltage where the capacitance
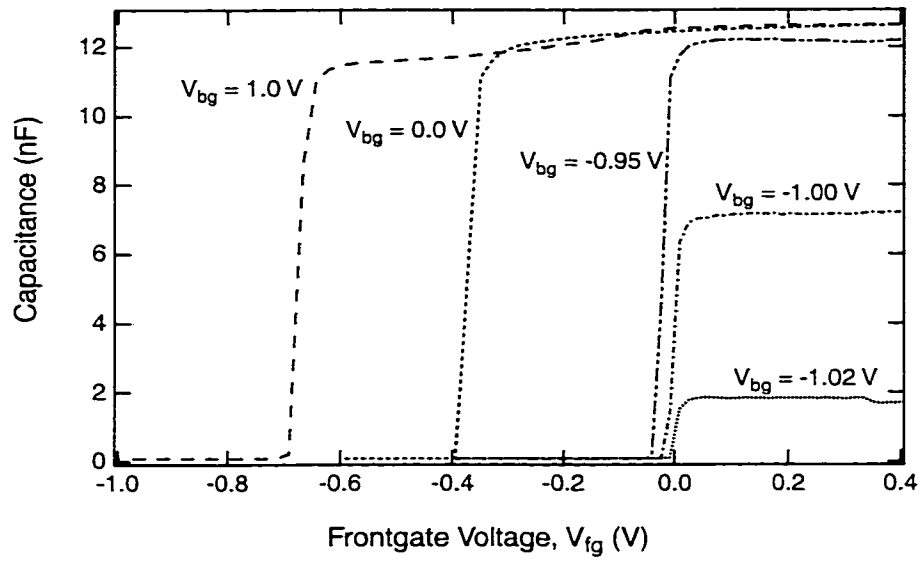
Figure 4.2: C-V at several backgate voltages for sample CC1 (wide well).
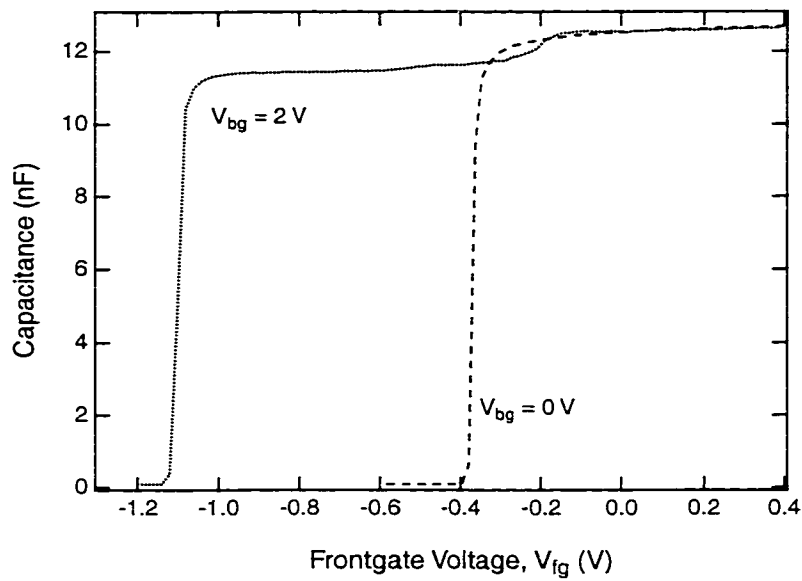
Figure 4.3: C-V at two different backgate voltages for sample CC1 (wide well). Note that the C-V is not flat-topped at V_{bg}=2 V.

steps up rather sharply. I didn't attempt to explain this behavior in detail, but I can think of a couple of suspects. First, the capacitance depends on the geometry of the charge layers, and the charge layer in the well moves around when the field is varied. This is true in any well, but the effect may be larger in the wide well, where the well width (40 nm) is a significant fraction of the frontgate-to-well spacing (200 nm). Second, the point at which the capacitance has the step seems to be where the excited subband begins to fill (which is indicated by the appearance of an additional peak in the absorption measurements). In any case, Equation 4.1.1 is still valid.

Measuring the C-V is slightly more challenging with a backgated sample than with a non-backgated sample. The main difficulty is that the quantum well is coupled to both the frontgate and the backgate. The circuit used for measuring the capacitance is shown schematically in Figure 4.4. I apply a tickle to the frontgate, and measure the current coming out the quantum well contact with a transimpedance amplifier, which holds the quantum well contact at virtual ground. The circuit equivalent of the sample itself is shown in Figure 4.5. However, there is another current path to ground, through the backgate, so just measuring the current through the quantum well contact misses that additional current. I could have measured the current out the backgate contact as well, but I decided it was easier to try to minimize the coupling of the current out through the backgate, by running the C-V at a rather low tickle frequency of 34 Hz. Using a low tickle frequency ensures that the impedance to the backgate is kept higher than the resistance out through the quantum well, except very near depletion, so I do a pretty good job of measuring the actual capacitance.

The effect of running with the tickle frequency too high is shown in Figure 4.6. Here I plot both the capacitance, which is 90° out of phase with the tickle, and the in-phase signal. At low gate voltage, the in-plane resistance of the quantum well is large because the sheet density is low (hence the increase in the in-phase signal). At higher frequencies, the impedance to the backgate is low enough that the current escapes through the backgate, and the capacitance signal drops.
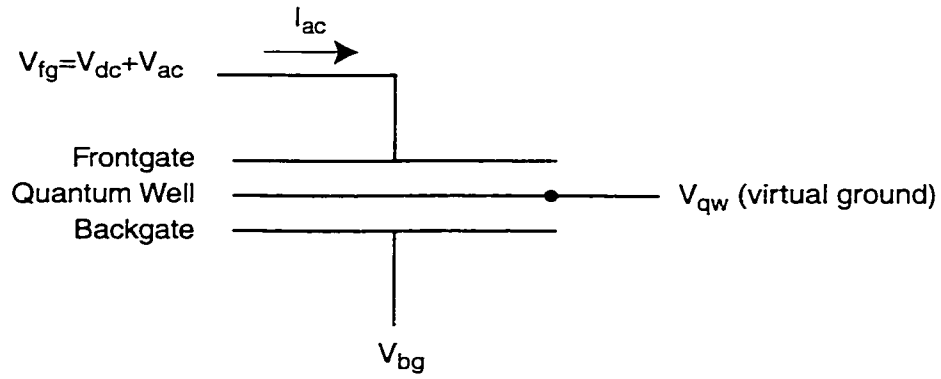
Figure 4.4: Sample wiring schematic for C-V measurement.
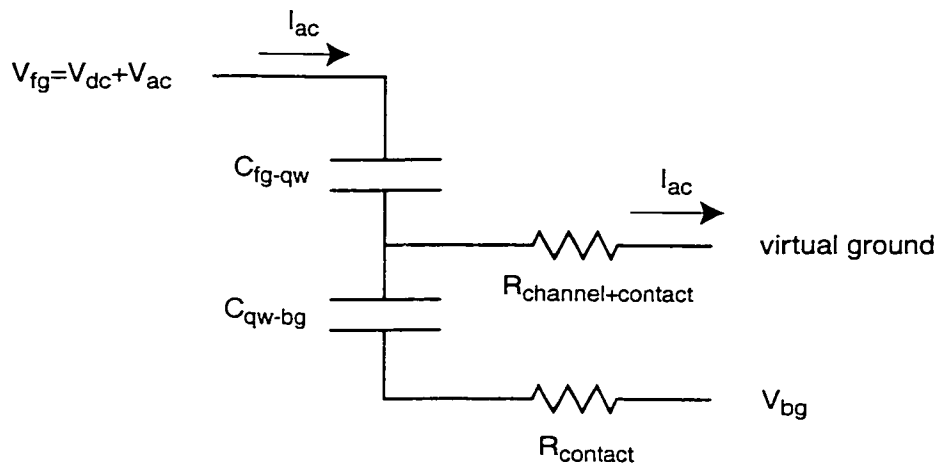
Figure 4.5: Circuit equivalent of the sample in C-V measurement.
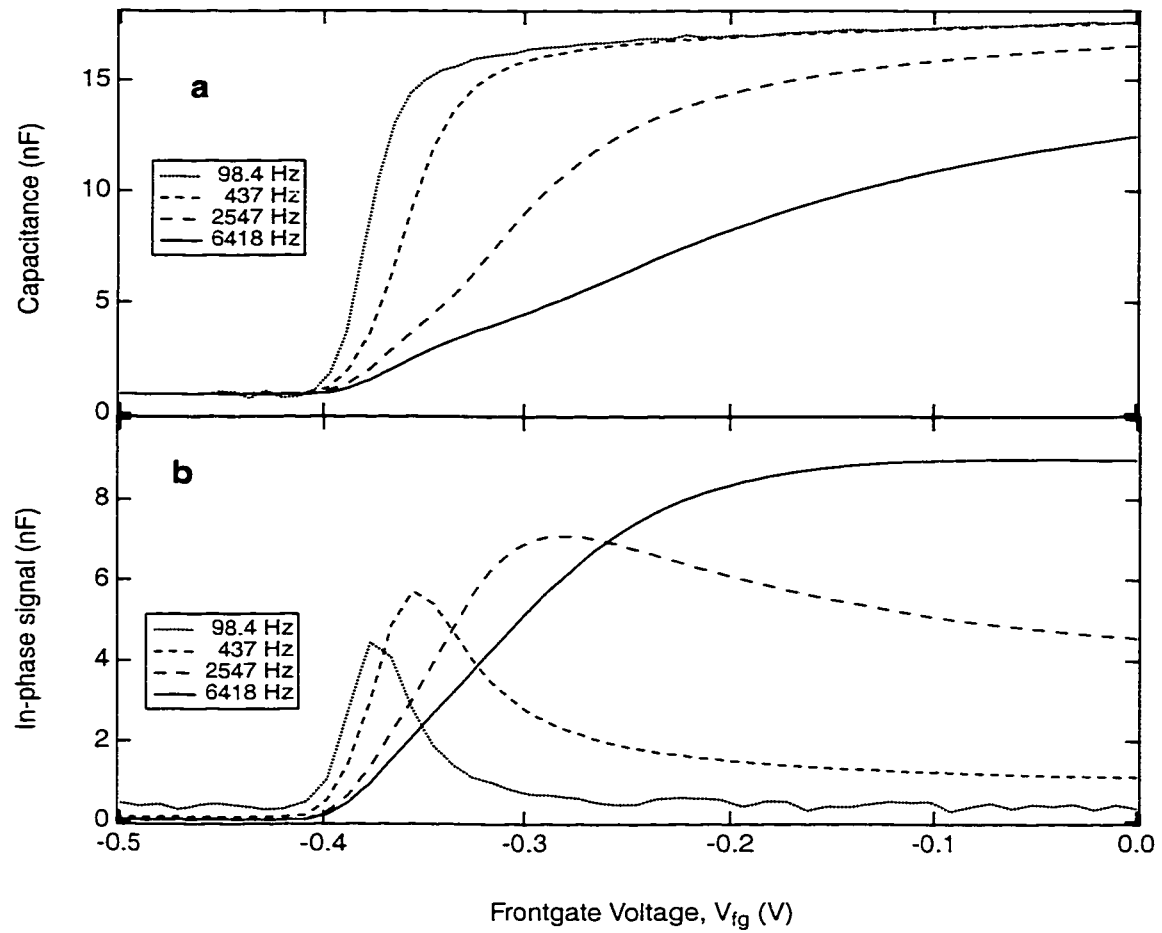
Figure 4.6: Frequency dependence of the C-V measurement. The backgate was fixed at -0.31 V. The sample was JW1. a) Capacitance vs. frontgate voltage. b) In-phase signal vs. frontgate voltage.
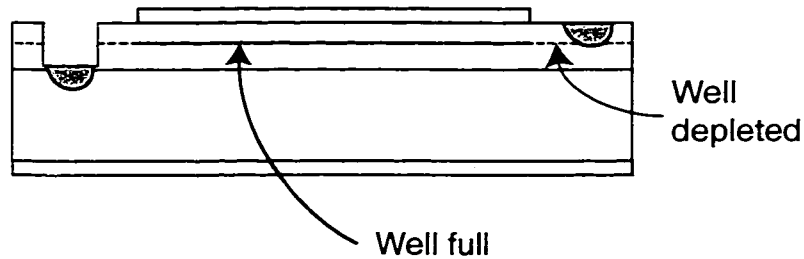
Figure 4.7: Cross-section of the sample showing the quantum well full under the backgate but empty elsewhere, thus cutting off the well from its contacts.

Another oddity about the backgated sample is that the backgate can deplete the regions of the quantum well that are not under the frontgate, even when the part of the well that is under the frontgate (the part I care about) is still full. See Figure 4.7. When this happens, I lose contact to the quantum well and can no longer control it, which obviously limits the range of useful backgate voltages. I can see this happen because the measured capacitance signal drops, as seen in Figure 4.2 for backgate voltages $V_{bg} < -0.95$ V. In this regime, the capacitance hasn't really dropped, but the quantum well contact resistance is effectively increasing. Much of the AC current will go out through the backgate instead of through the quantum well contact, so the capacitance measurement has an artificially low reading, which in turn skews my density calculation. The effect is even worse for higher tickle frequency, so again it's important to run the C-V at a low tickle frequency.

4.1.2 Electric field calculation

The DC electric field was calculated from the applied gate voltages and sample dimensions using the following formula:

$$\text{Field} = \frac{V_{fg}}{2d_{fg}} - \frac{V_{bg}}{2d_{bg}}$$

where $V_{fg(bg)}$ is the frontgate (backgate) voltage with respect to the quantum well voltage, and $d_{fg(bg)}$ is the distance of the frontgate (backgate) from the quantum

well. (This formula is derived from an expression for the field in a non-backgated sample, given in Keith Craig's Ph.D. dissertation [6]). A positive field pushes the electron distribution towards the surface, while a negative field pushes the electron distribution towards the substrate. The formula gives the field applied to the well by external charges on the gates, and does not include bending of the bands due to electron-electron interaction. In addition to the applied field there is typically a fixed, built-in electric field.

This formula for finding the field makes the simplifying assumption that the quantum well is infinitesimally thin. This breaks down somewhat, as seen by the fact that the capacitance of a full well is not quite constant. I haven't worried about this too much, but clearly there is some systematic error in my estimate of the applied field.

4.1.3 Independent control of density and field

In the experiments, I would set the backgate voltage, measure the C-V to determine the charge density vs. V_{fg}, and measure absorption spectra at several set values of the charge density. I would then repeat the procedure at a different backgate voltage, measuring spectra at the same charge densities, and so on. I could then piece together the spectra that were taken at the same charge density, and calculate the fields from the backgate and frontgate voltages I had used. In this way, I could put together sets of data for which the charge density was held fixed and the field was varied.

That's the procedure in a nutshell, but I'll explain it here in more detail. As explained above, the field F is given by

$$F = \frac{V_{fg}}{2d_{fg}} - \frac{V_{bg}}{2d_{bg}}$$

Thus, to vary the gate voltages but keep the field at a constant value F, the frontgate

voltage is varied according to

$$V_{fg} = 2d_{fg}F + \frac{d_{fg}}{d_{bg}}V_{bg}$$

Notice that one varies the two gate voltages in the same direction in order to keep the field constant. However, moving the voltages in the positive direction increases the sheet density, while moving them in the negative direction decreases the sheet density. Thus, the sheet density is varied, while the electric field remains constant.

Neglecting voltage dependence of the capacitances, the sheet density N_s (number of electrons per unit area) is given by

$$N_s = N_{s,0} + c_{fg}V_{fg} + c_{bg}V_{bg}$$

where $c_{fg(bg)}$ is the capacitance per unit area between the quantum well and the front-gate (backgate). (The sheet density was actually calculated using Equation 4.1.1, but this form is used here to elucidate the whole process). Thus, to vary the gate voltages but keep the sheet density at a constant value N_s, the frontgate voltage is varied according to

$$V_{fg} = \frac{1}{c_{fg}}(N_s - N_{s,0}) - \frac{d_{fg}}{d_{bg}}V_{bg}$$

where I've used the fact that $\frac{c_{bg}}{c_{fg}} = \frac{d_{fg}}{d_{bg}}$. Notice that one varies the two gate voltages in opposite directions in order to keep the density constant. Increasing one gate voltage puts more charge in the well, and decreasing the other gate voltage takes the charge back out of the well. However, increasing one gate voltage and decreasing the other changes the electric field. Thus the sheet density remains constant, while the electric field is varied.

Figure 4.8 is a plot of lines of constant sheet density and constant field in the $V_{fg} - V_{bg}$ plane. The figure also indicates the limits of the gate voltages that I could apply. The frontgate voltage could not go too far positive, or the Schottky diode would be forward-biased and significant conduction would occur. Similarly, the backgate voltage could not go too high, or significant conduction between the
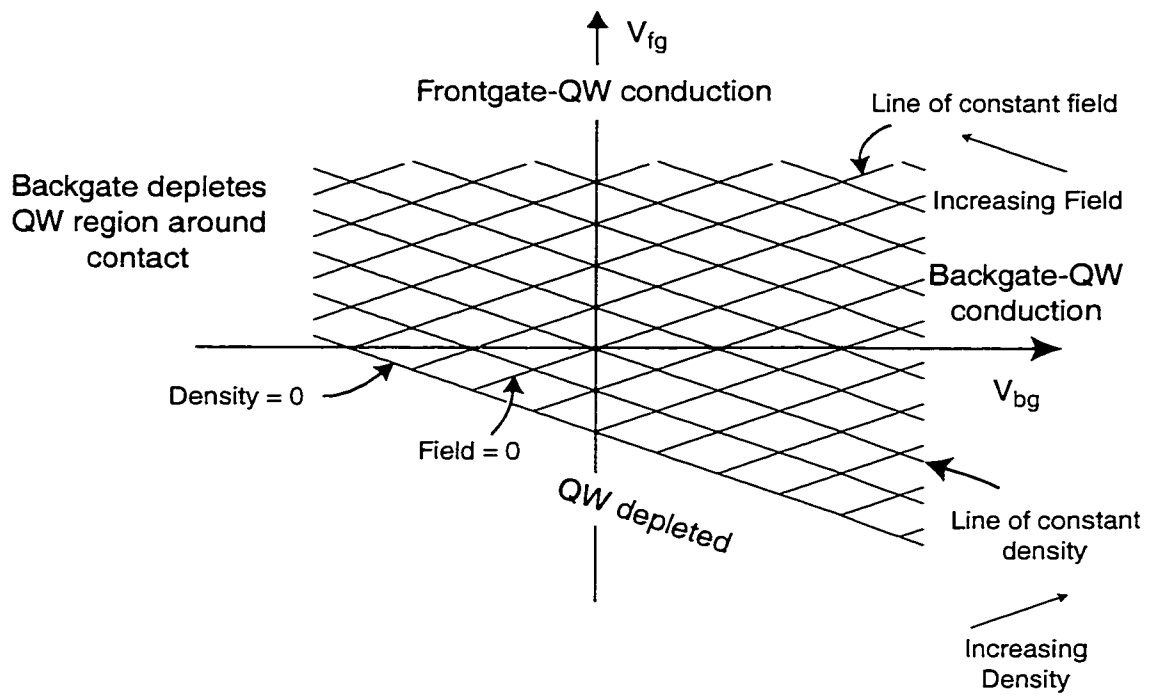
Figure 4.8: Plot of the $V_{fg} - V_{bg}$ plane, indicating lines of contant sheet density and constant field, and the range of usable gate voltages.
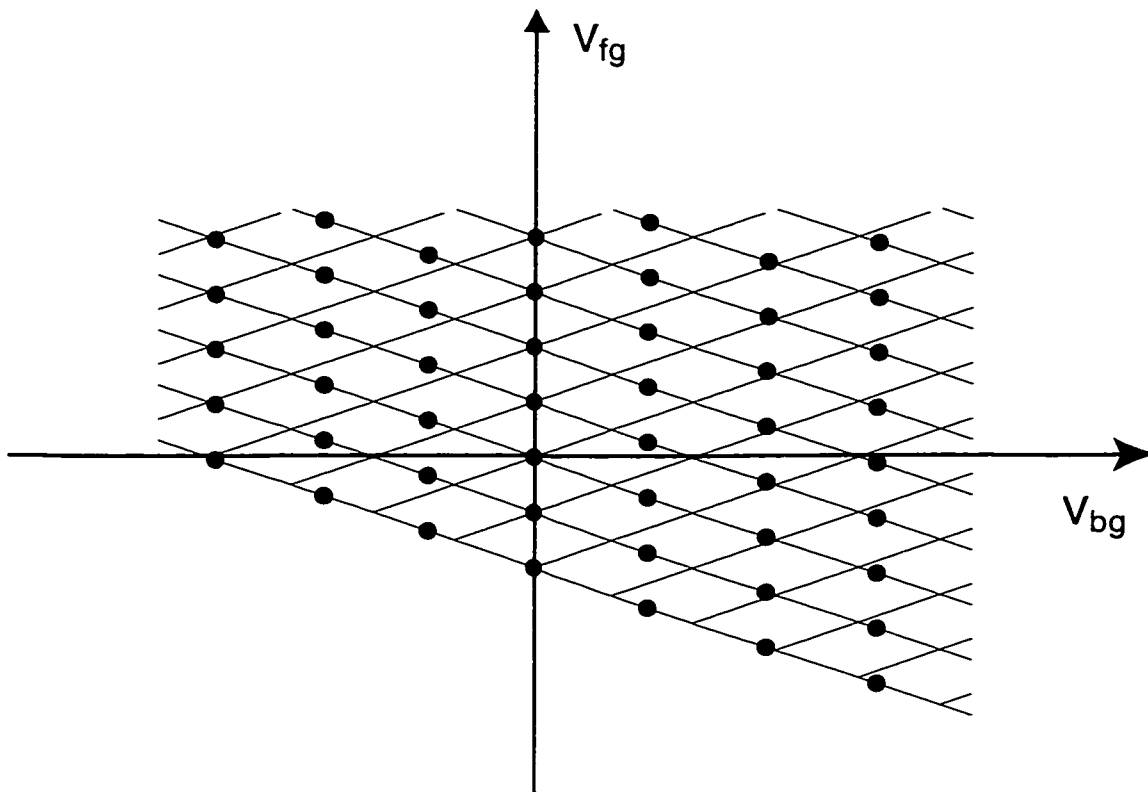
Figure 4.9: Plot of the $V_{fg} - V_{bg}$ plane. The dots indicate a set of voltages at which spectra are measured.

backgate and the quantum well would occur. The backgate voltage could not go too low, either, or I would cut off the quantum well from its contact, as described above.

Figure 4.9 indicates how I varied the gate voltage in the experiments. A backgate voltage was selected (one of the dots at the bottom of the graph) and measurements made at a set of frontgate voltages corresponding to certain charge densities (all the dots stacked up directly above). This procedure was repeated for different backgate voltages. I then picked out the spectra at constant charge density (dots lying along the diagonals).

4.2 Mobility measurement

I measured the mobility on a separate sample cleaved from an adjacent spot of the same wafer. The mobility sample was processed in the van der Pauw geometry [16], with a frontgate over an active region of dimensions 2mm × 2mm, as shown in Figure 3.8. The mobility was measured by applying a small (4 mV P-P) tickle voltage at 14 Hz to two of the contacts, and measuring the voltage on the opposite two contacts with a lock-in amplifier. The mobility was then calculated using Reference [16].

The procedure used to get data at a constant field, with varying field, is similar to that described in the previous section. The only difference is that I didn't measure the mobility at only a predetermined set of sheet densities. Instead, at each backgate voltage I would measure the mobility at a dense set of frontgate voltages, and to find the mobility at a certain density I would interpolate the data between the two data points on either side of the corresponding frontgate voltage. This was possible because the time required to measure a single mobility is much shorter than that required to measure an absorption spectrum.

4.3 Infrared absorption measurements

The spectra were measured with a Fourier Transform IR spectrometer [12]. I used two different geometries for coupling the light into the sample.

4.3.1 Edge coupling geometry

Most of the experiments were performed using the edge-coupling geometry, as shown in Figure 4.10. The THz was concentrated on the edge of the sample using a Winston cone [22]. The path length through the sample was 6 mm. A polarizer was inserted after the sample to select the component of the transmitted light with polarization in the growth direction. The transmitted light was then detected by a
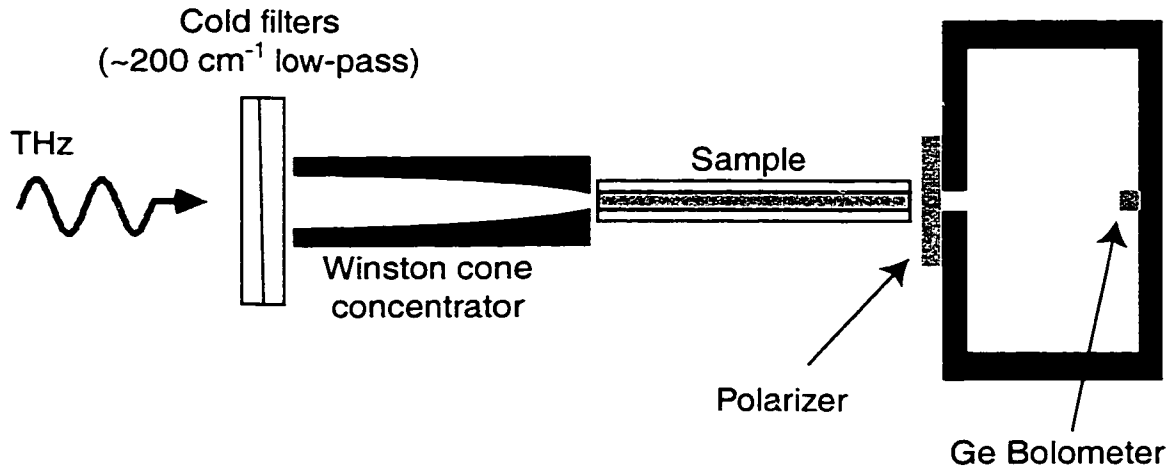
Figure 4.10: Infrared absorption measurement setup in the edge-coupling geometry.

bolometer.

The advantage of the waveguide geometry is that it provides a long optical path length through the sample, and large overlap of the light field with the quantum well region of the sample, so that the absorption of light by the sample is quite large (often up to 40 % at high charge density). This was important, because if the absorption strength had been small, I would have had to use long integration times for each spectrum in order to get an acceptable signal to noise ratio. Because my experiment involved measuring the absorption spectrum as a function of two different parameters, and was thus very time-consuming, this study would not have been feasible without good signal to noise.

A potential disadvantage of the waveguide geometry is that there may be a wavelength-dependent phenomena in the waveguide itself, which may affect the measured absorption spectra of the quantum well. This possibility was investigated by measuring a sample without the waveguide, as discussed in the next section.
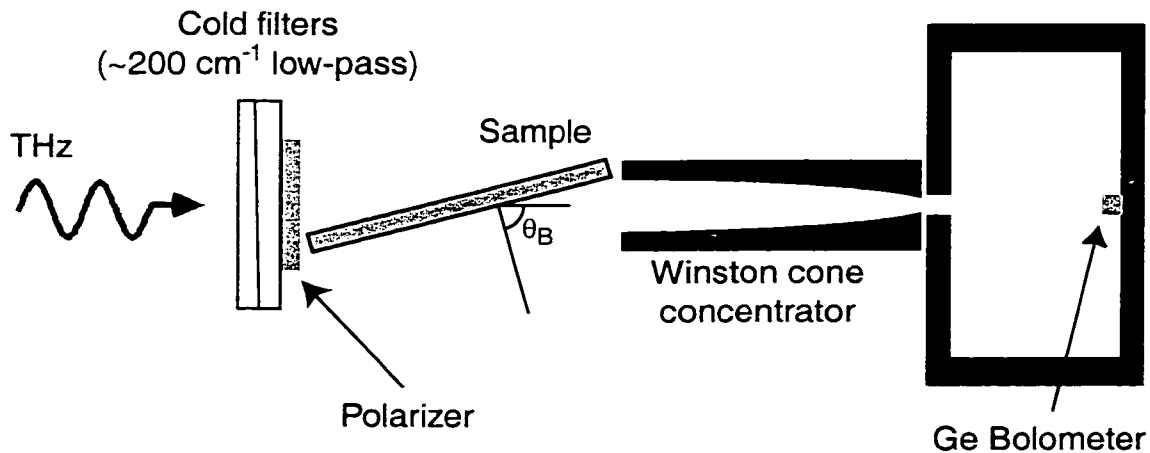
Figure 4.11: Infrared absorption measurement setup in the Brewster angle transmission geometry.

4.3.2 Brewster angle transmission geometry

I also did an infrared absorption experiment using a different geometry, in which polarized THz is incident on the surface of the sample at Brewster's angle, and the transmitted light is concentrated onto the bolometer by the Winston cone (Figure 4.11). There is no frontgate, and no metal on the backside of the sample. The absorption in this geometry is quite small ($\sim$ 1%), so this is not a practical way of examining absorption as a function of two variable parameters. However, it has the advantage of eliminating any waveguide effects, so I did the experiment to see whether waveguide effects significantly change the absorption of the sample.

4.3.3 Normalization of the spectra

Each raw spectrum, with electrons in the well, was normalized to the spectrum measured with the well depleted by the gates (see Figure 4.12). The attenuation
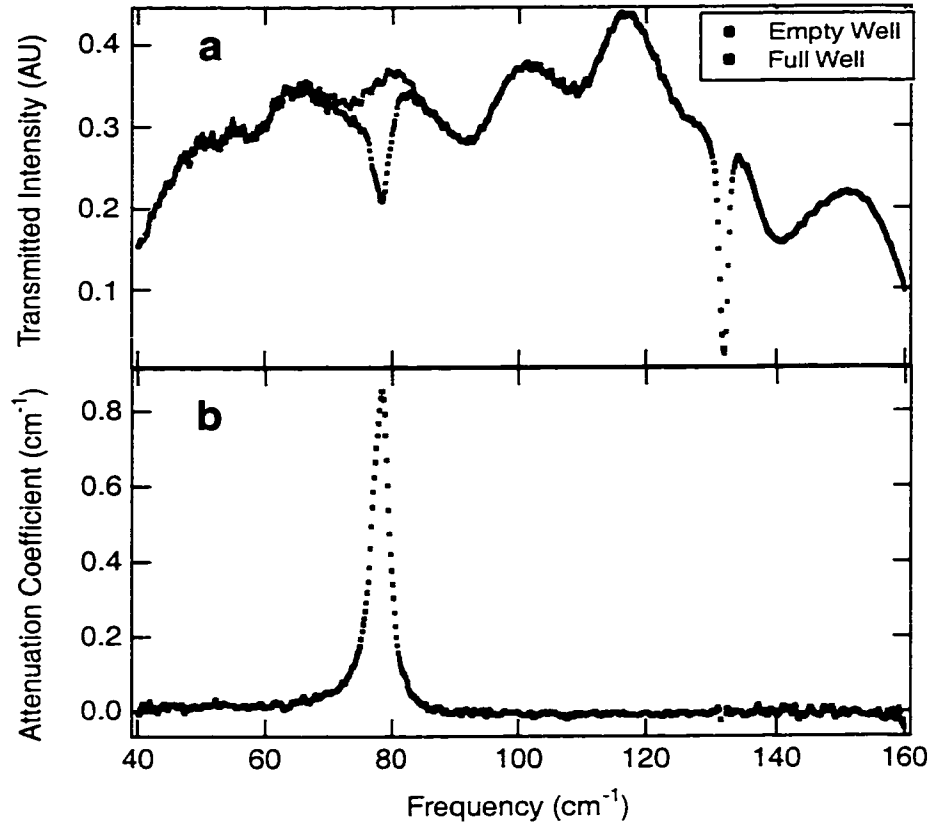
Figure 4.12: a) Raw transmission spectra for empty well and full well. b) Resulting normalized spectrum.

coefficient is given by

$$\alpha(\omega) = \frac{1}{\text{sample length}} ln \frac{I(\text{empty})}{I(\text{full})}$$

where ω is the frequency, $I(\text{empty})$ is the transmitted intensity vs. frequency with the well depleted of electrons, and $I(\text{full})$ is the transmitted intensity vs. frequency with the well full of electrons.

4.3.4   Curve fitting

I fit the absorption spectrum to the following Lorentzian lineshape function:

$$\alpha(\omega) = A + \frac{B\omega}{(\omega - C)^2 + D^2}$$

The parameter C is the peak position and D is the linewidth (half-width at half-max). The area under the absorption curve, which I'll refer to as the absorption strength, is given by $\pi BC/D$. The parameter A is a constant offset, which is ideally zero but can be nonzero if the FTIR source intensity or the detector sensitivity drifted somewhat between the time when the sample spectrum was taken and the reference spectrum was taken. Such a drift would not affect the other fit parameters.

42

Chapter 5

Results for the double square well

I made measurements on several asymmetric double square well samples. The most significant outcome of these experiments was that they convinced me to move on to experiments with the wide square well sample, which are described in Chapter 6. In this chapter, I'll briefly describe the results of these initial experiments.

5.1   Sample DSQC: no backgate

My first intersubband absorption experiments were performed on the sample DSQC, an asymmetric double square well sample with no backgate. I measured the absorption as a function of frontgate voltage and temperature. With only a frontgate to control the charge density in the sample, I could not vary the electric field independently of the charge density (see Figure 5.1).

In Figure 5.2 I plot the parameters of the absorption spectra as a function of gate voltage, at several temperatures. The same linewidth data are plotted vs. temperature for several gate voltages in Figure 5.3.

I was at first interested primarily in the temperature dependence of the

DC Electric Field (mV/nm)
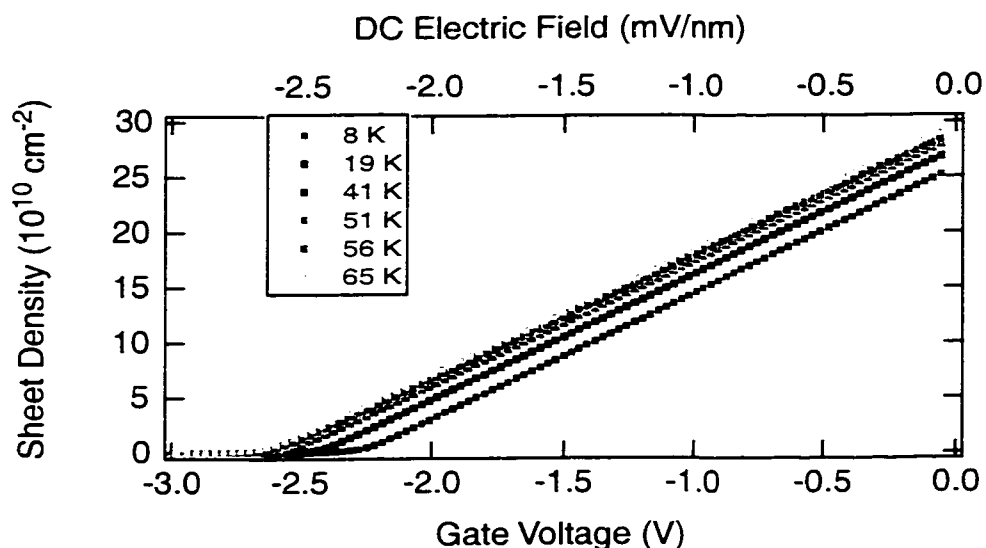
Figure 5.1: DSQC charge density at different temperatures

linewidth, at constant charge density. However, there are some complications here. First, Figure 5.1 shows that the charge density depends on temperature, so I would have to use a different gate voltage at each temperature in order to keep a constant charge density. This changes the electric field in the well, and I didn't know how that might affect the linewidth. Second, the peak position as a function of gate voltage has a different minimum position at low temperature than at high temperature. This may be due to the change in charge density, or may be due to some change in the static built-in field.

At constant temperature, one could examine the charge density dependence of the absorption, but of course the effects of varying charge density could not be distinguished from the effects of varying electric field.

In order to clear up these issues, a backgated sample was measured.
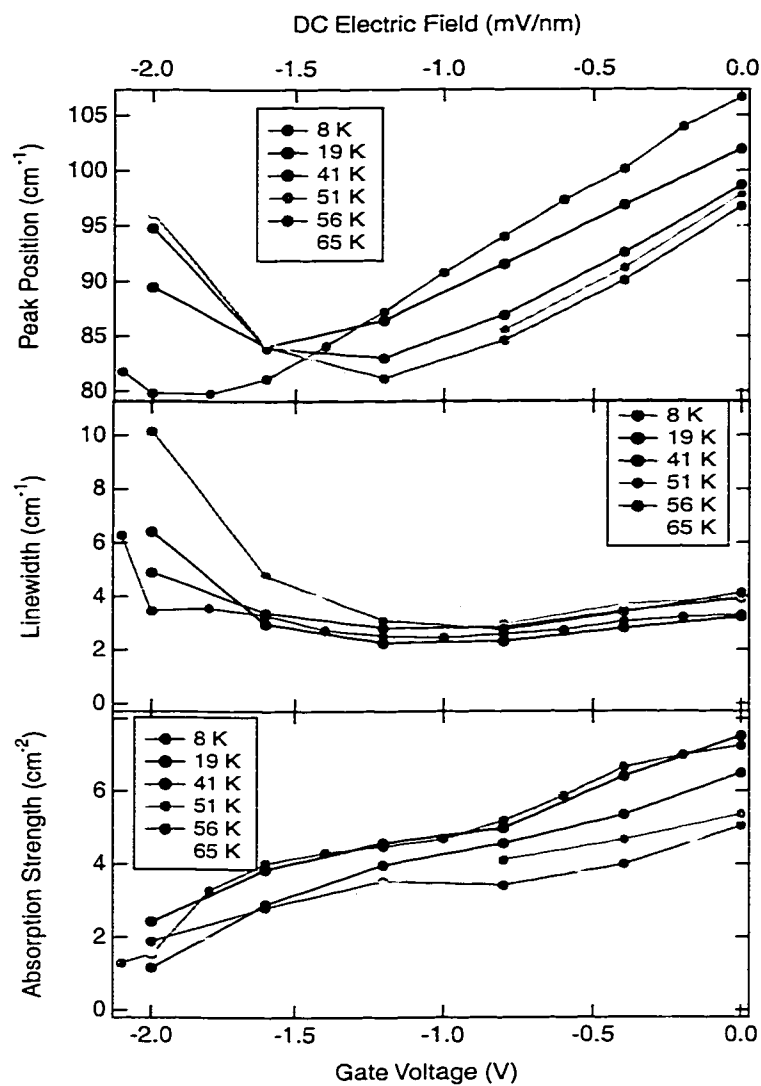
Figure 5.2: DSQC fit parameters vs. gate voltage, at several temperatures.
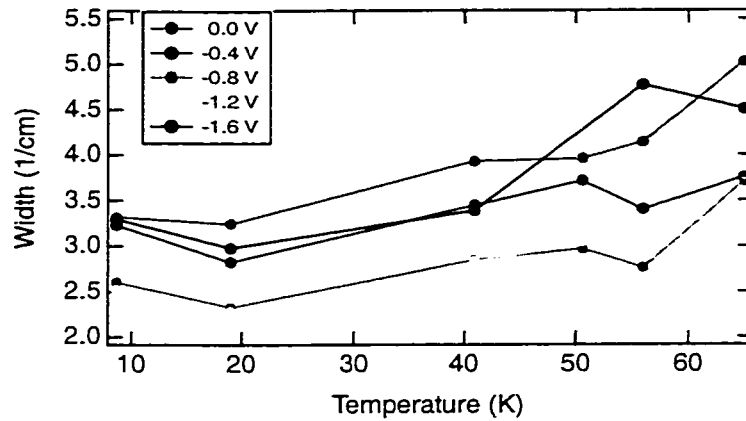
Figure 5.3: DSQC absorption linewidth vs. temperature for several gate voltages.

5.2   JW1: Backgated sample

I next measured the sample JW1, with a well similar to that of the sample DSQC but with a backgate. The backgate allowed me to vary the charge density and field independently. The backgate in this sample didn't work out as well as I had hoped it would: for some reason, setting the backgate voltage higher than a certain range of negative voltages led to loss of charge from the well, which could only be reversed by warming the sample. (The charge may have become trapped in defects in the low-temperature-grown layer between the backgate and quantum well). Thus, I had only a limited range of fields available.

The parameters of the absorption spectra at low temperature are shown in Figure 5.4. Although the range of fields used was limited, it appears that the linewidth may be minimized when the peak position is minimized. I thought it would be nice to look at a backgated sample in which I could tune the peak position all the way through a minimum, and see what happens to the linewidth. This led to the work on the wide well, described in Chapter 6.
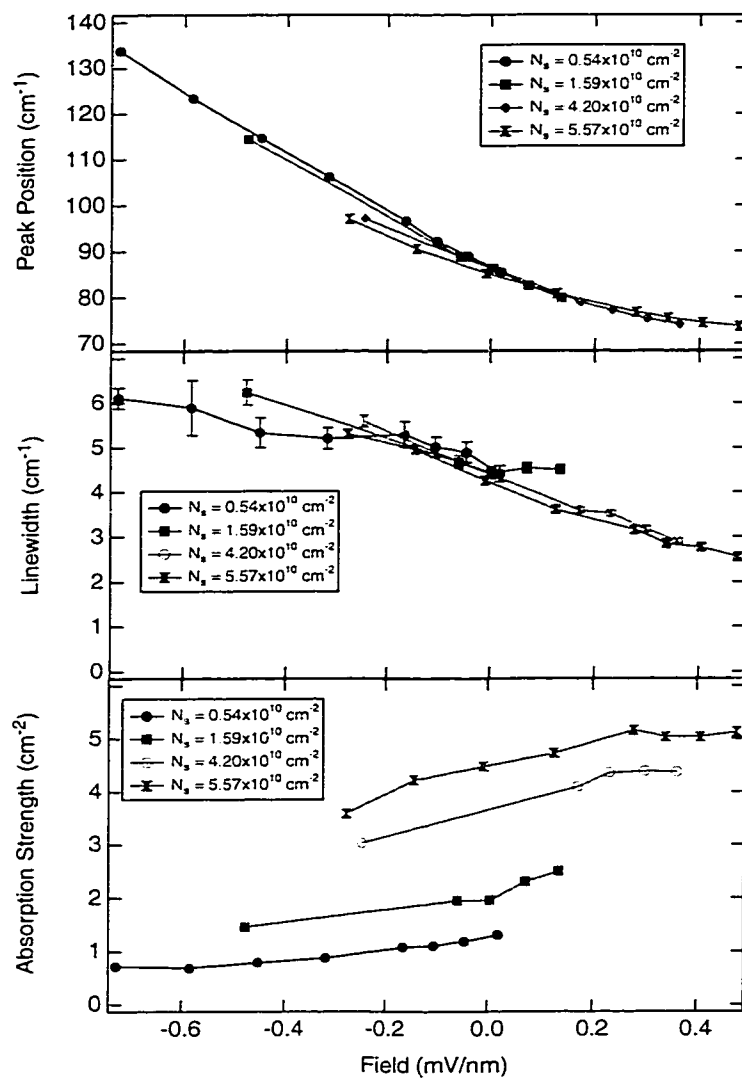
Figure 5.4: JW1 fit parameters vs. electric field, at several charge densities.
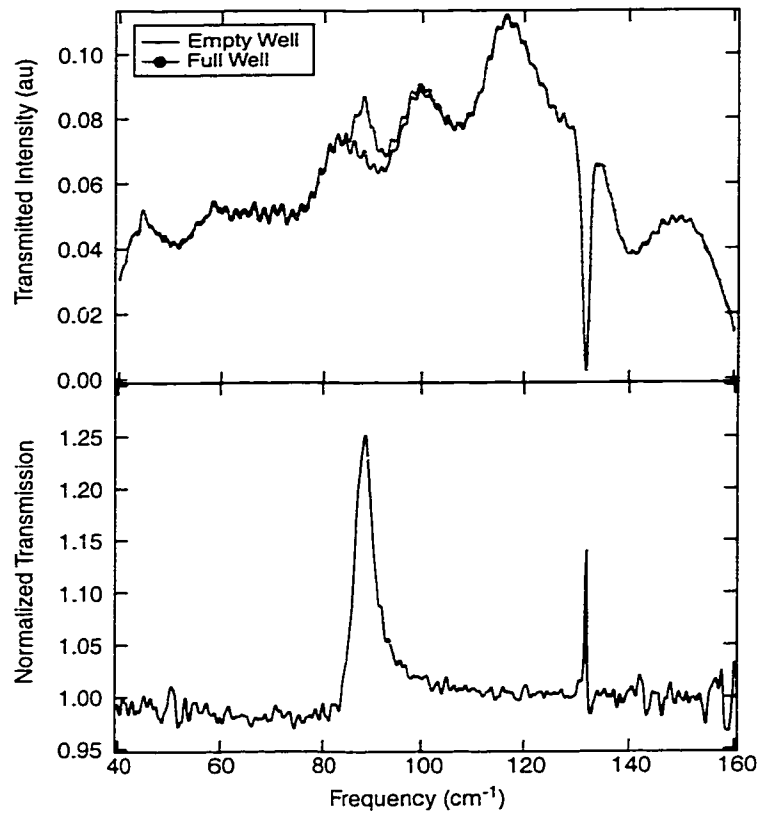
Figure 5.5: Strange behavior in GB1. a) raw transmission spectra for the empty and full well.

5.3 GB1: another backgated sample

I measured a backgated double well sample (GB1) for Gabriel Briceño, who was making a THz detector and wanted his wafer characterized. The behavior was totally unexpected: the absorption peak pointed the wrong way. See Figure 5.5. That is, the sample absorbed less at the resonant frequency. The peak tuned correctly with the gate voltage, which convinced me that I was seeing something related to an intersubband transition, but I didn't figure out why the sample behaved that way.

Chapter 6

Results for the wide square well

After measurements on several double square well samples, both with and without a backgate. a wide square well (sample CC1. described in Chapter 3) was measured. The most thorough experiments described in this dissertation were performed on this wide square well.

6.1 Absorption data

6.1.1 Full well

I performed the absorption experiments on a single cool-down. To get all the spectra (typically over 100 of them). the experiment usually took about 30 hours. I measured the spectra for charge density between depletion and 1.3×10^{11} cm^{-2}. The temperature was 2.3 K. Typical spectra, measured for several values of the applied field. at a constant charge density of 5×10^{10} cm^{-2}, are shown in Figure 6.1. The minimum in peak position identifies zero electric field in the well. The linewidth shows an unexpectedly sharp minimum at zero field. and saturates with a larger value at non-zero field.
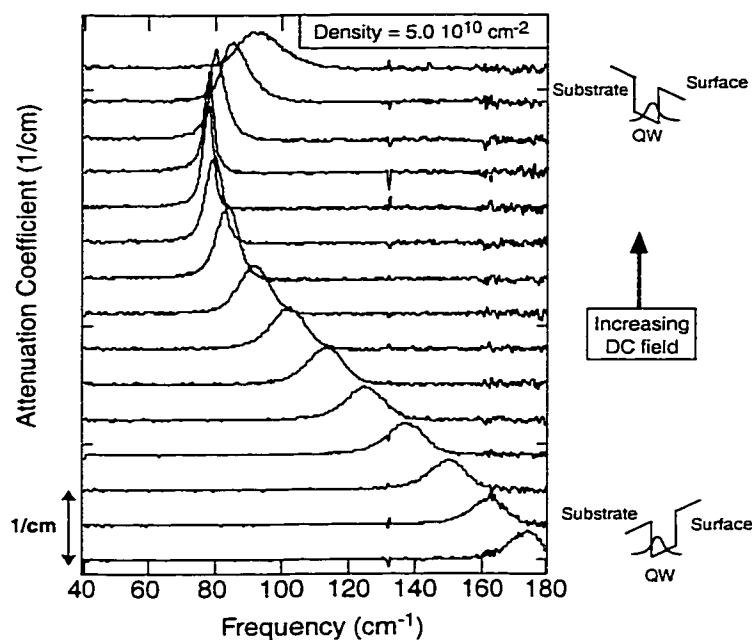
Figure 6.1: Spectra measured at charge density of 5×10^{10} cm^{-2} and several values of the electric field.

Peak Position

The peak positions are plotted against applied DC field, for several charge densities, in Figure 6.2a. The peak position is tunable by over a factor of two, from 75 cm^{-1} to over 160 cm^{-1}. Since this is a symmetric quantum well, the peak position should be symmetric about its minimum value at zero DC field. The peak position shows the expected quadratic dependence on DC field. The minimum of the peak position occurs at an applied field of -0.3 mV/nm, which implies that the sample has an additional fixed, built-in field of +0.3 mV/nm.

Linewidth

The existence of a sharp minimum at flat-band in the field dependence of the linewidth, seen in Figures 6.1 and 6.2, cannot be explained by assuming that the
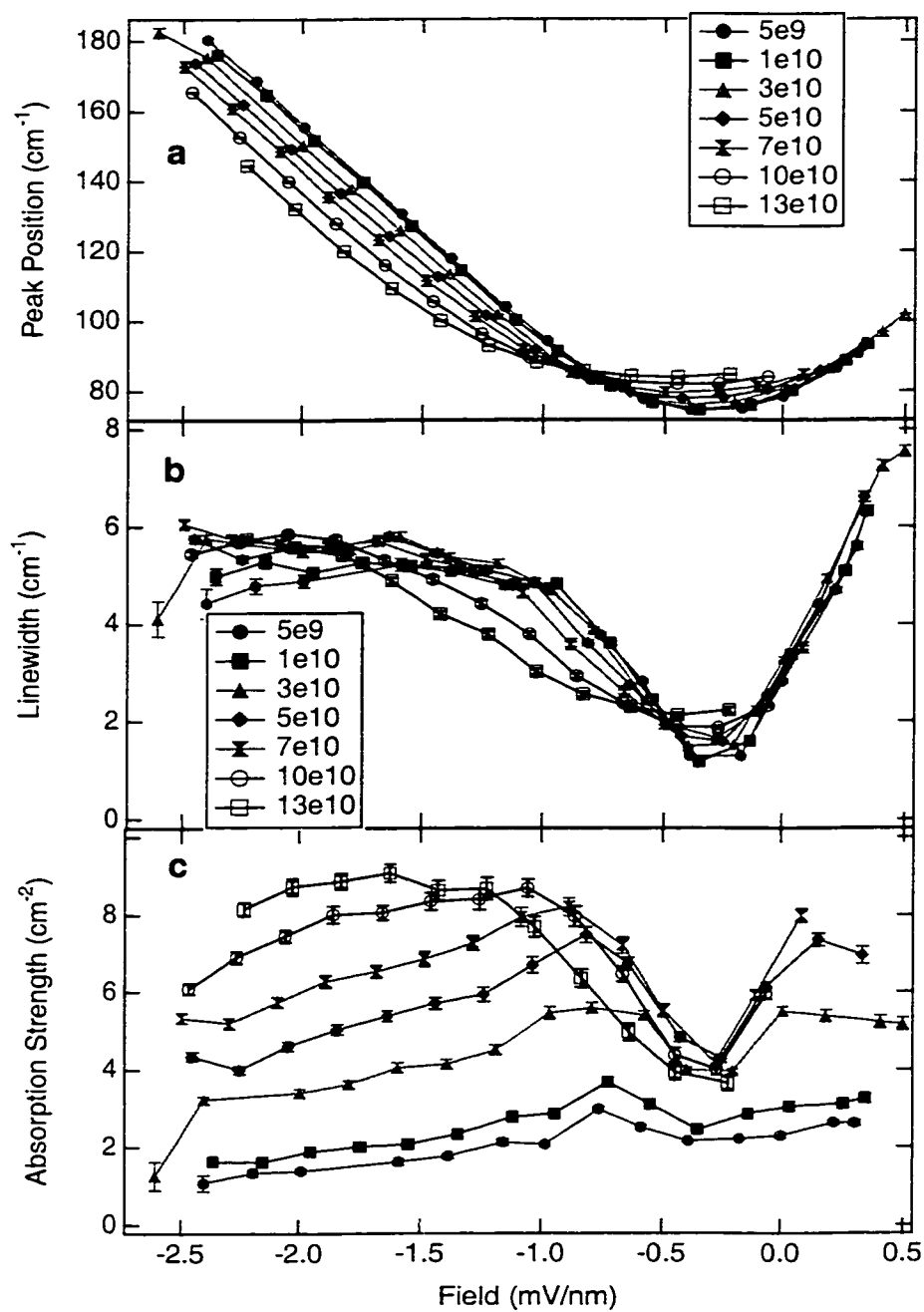
Figure 6.2: Parameters from fits to the spectra at several sheet densities. The sheet densit:~s are given in units of cm⁻² a) Peak position. b) linewidth. c) integrated absorption strength.
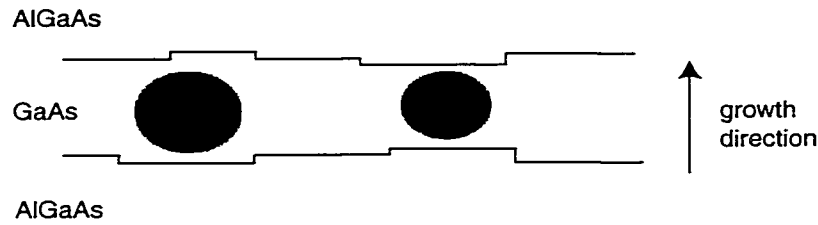
Figure 6.3: Inhomogeneity in the sample due to well-width fluctuations.

line is inhomogeneously broadened. With the remote donor layers 100 nm away from the well, the most likely source of inhomogeneous broadening is an inhomogeneous well-width (see Figure 6.3). Electrons in different parts of the sample see a different well width, and thus absorb at different frequencies. The measured absorption line then would be a superposition of absorption lines from all over the sample, and would thus be broadened by an amount equal to the range of superposed peak absorption frequencies.

I make a distinction between the well width fluctuations considered here and the interface roughness considered later in this chapter. Although both are due to a non-uniform well width, the well width fluctuations that may give rise to an inhomogeneously broadened line should have a long length scale, such that electrons in different parts of the sample do not correlate to each other. By contrast, the interface roughness, considered below as a source of scattering, is of a much shorter length scale.

One can estimate the inhomogeneous linewidth by calculating the absorption frequency for a slightly wider well and for a slightly narrower well and taking the difference. A reasonable well-width variation in these samples is about 0.5 nm. Figure 6.4 shows the result of the calculation for a well 40 nm wide and a well 39.5 nm wide. We see that the estimated inhomogeneous linewidth has a maximum at flat-band, and approaches zero off of flat-band. It makes sense that the inhomogeneity would be weakest away from flat-band, when electrons everywhere in the plane
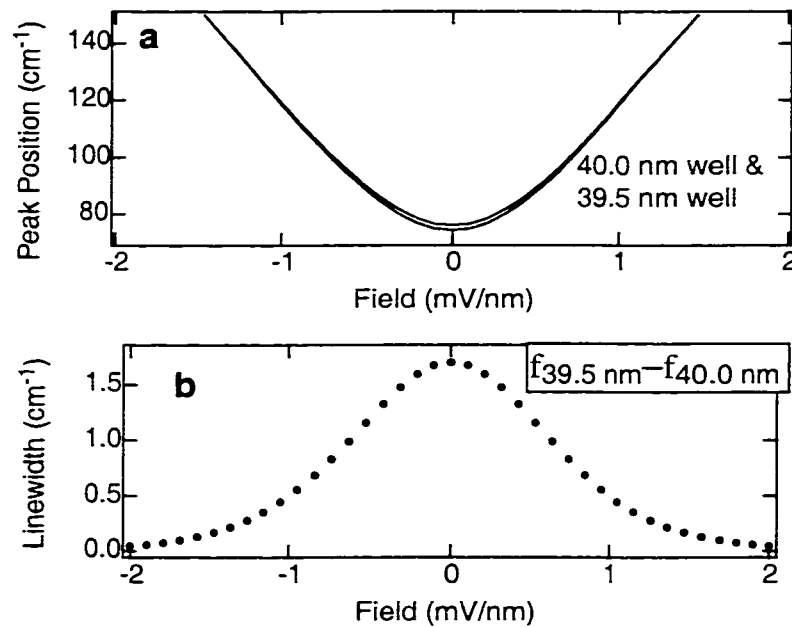
Figure 6.4: Argument for homogeneous broadening. a) Calculated absorption frequencies for a 39.5 nm well and a 40 nm well. b) Estimated linewidth due to well-width fluctuations. found by subtracting the curves in part a). The calculated linewidth shows a maximum at flat-band, opposite to what is measured.

are pushed against one side of the well and see a potential which is triangular. a shape that is independent of the position of the other side of the well.

The measured linewidth shows exactly the opposite field dependence: it has a minimum at flat-band. I concluded that. at least for non-zero applied field. the line is homogeneously broadened. At flat-band, the line may turn out to have an inhomogeneous component. but this would not affect the basic features of the field dependence. This is an important point, because a homogeneous linewidth tells us something intrinsic about the nature of the excitation, and is not simply determined by sample-dependent inhomogeneities.

Since the line is homogeneously broadened, it is inversely proportional to the dissipation time τ_d of the excitation, which is determined by scattering. The
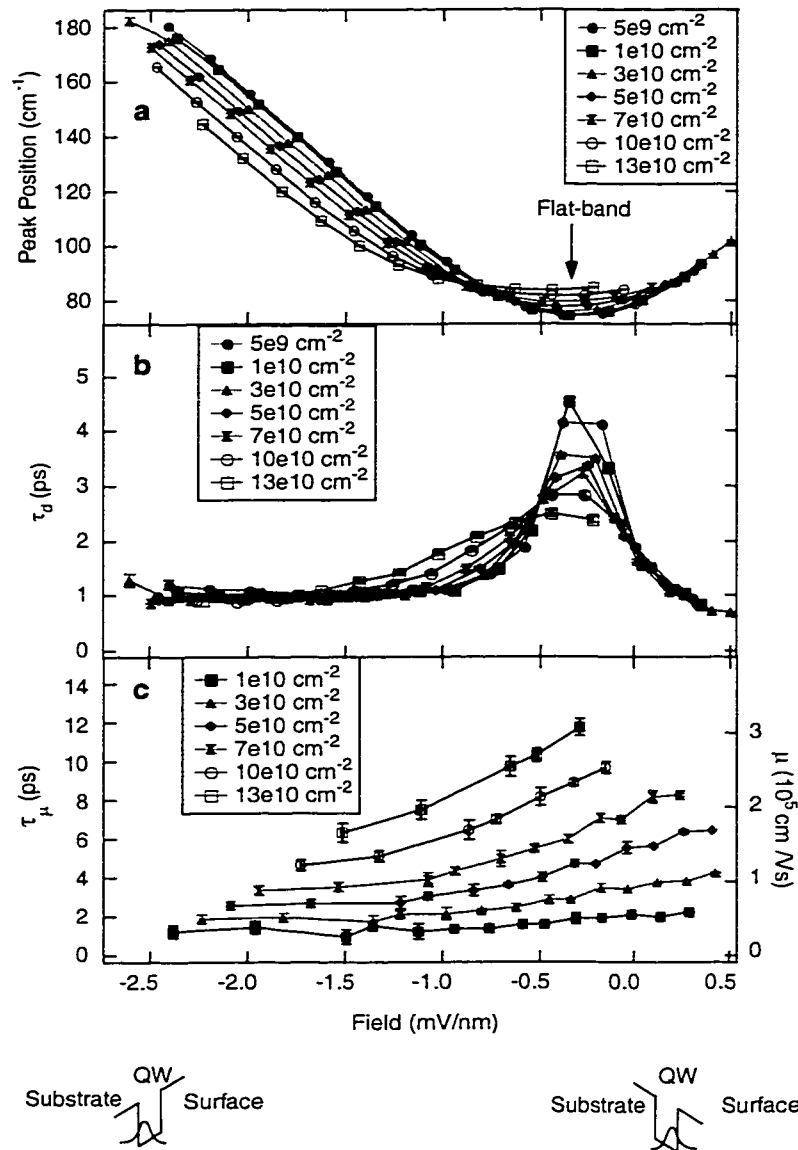
Figure 6.5: Peak position, dissipation time, and transport lifetime.

linewidth (half-width at half-max) is related to the dissipation time by $\tau_d = (2\pi c \times$ linewidth$)^{-1}$.

The ISB dissipation time is plotted against applied DC field in Figure 6.5b. The data shows several interesting features. First, the dissipation time has a strong field dependence, having a sharp maximum at zero bias, which coincides with the minimum in peak position. Second, the field dependence is greater at low charge densities than at high charge densities. Third, the dissipation time data are asymmetric about zero field, saturating at 1 ps for negative tilts (more negative frontgate) but appearing lower than that for positive tilts (more positive frontgate).

Absorption strength

The absorption strength was expected to be proportional to the charge density in the well. We can see from Figure 6.2c that near flat-band, the measured absorption strength deviates strongly from the expected behavior, and is actually non-monotonic in charge density. That is, putting more charge in the well actually decreases the absorption strength. This bizarre behavior was observed earlier by Keith Craig [6] in a non-backgated wide well and has been puzzling us ever since. I haven't figured out why it happens, but here I'll describe the behavior in some detail.

In Figure 6.6 I plot a series of spectra for different charge densities away from flat-band, where the absorption strength behavior is correct. In Figure 6.7, I replot curves for the lowest ($N_s = 0.5 \times 10^{10}\text{cm}^{-2}$) and highest ($N_s = 13 \times 10^{10}\text{cm}^{-2}$) charge density, along with the curve fits to Lorentzians. The absorption line at low charge density looks pretty much Lorentzian. At high charge density, the absorption line deviates somewhat from the Lorentzian shape, but not strongly.

In Figure 6.8 I plot a series of spectra for different charge densities near flat-band, where the absorption strength deviates from the expected behavior. It is clear that as the density is increased by over a factor of ten, the area under the absorption curve increases by only about a factor of two. It also appears that the absorption
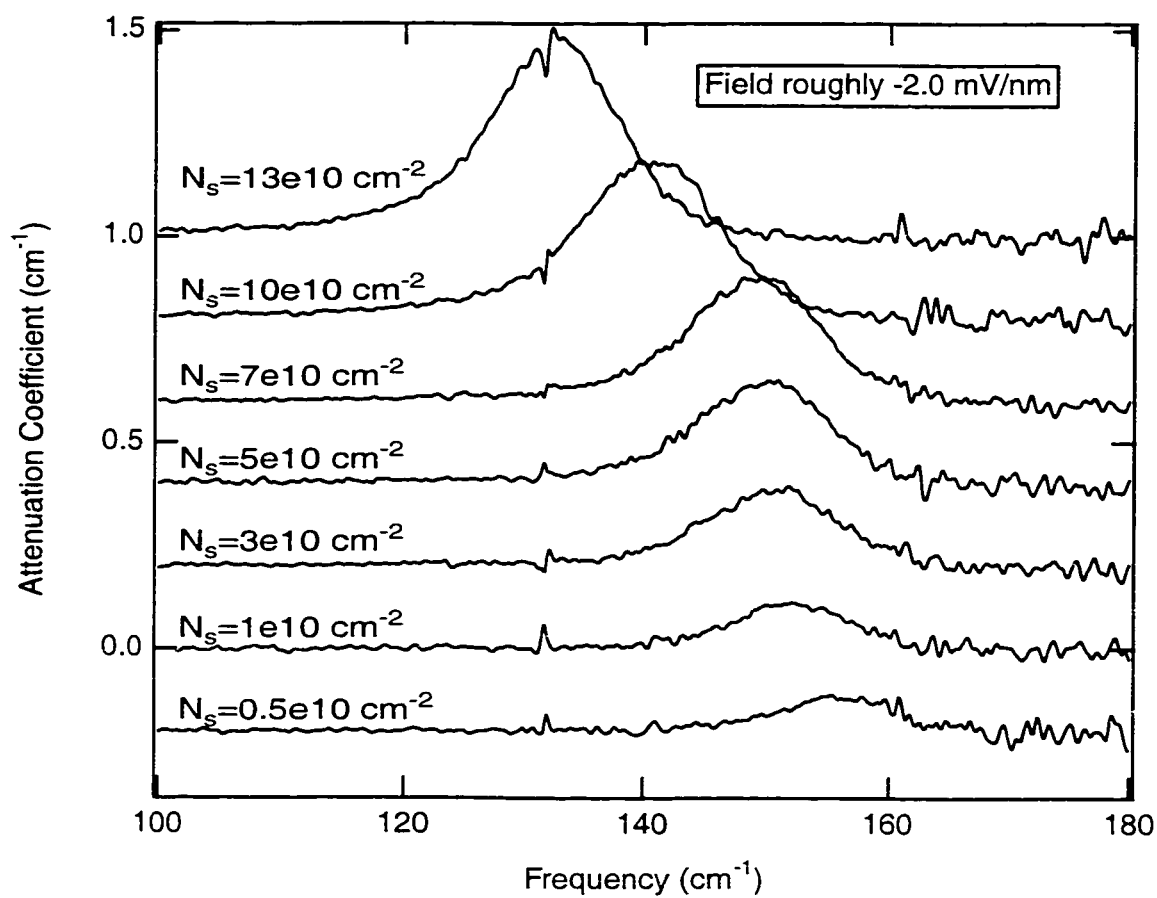
Figure 6.6: Spectra measured at various charge densities. away from flat-band. The curves are offset for clarity.
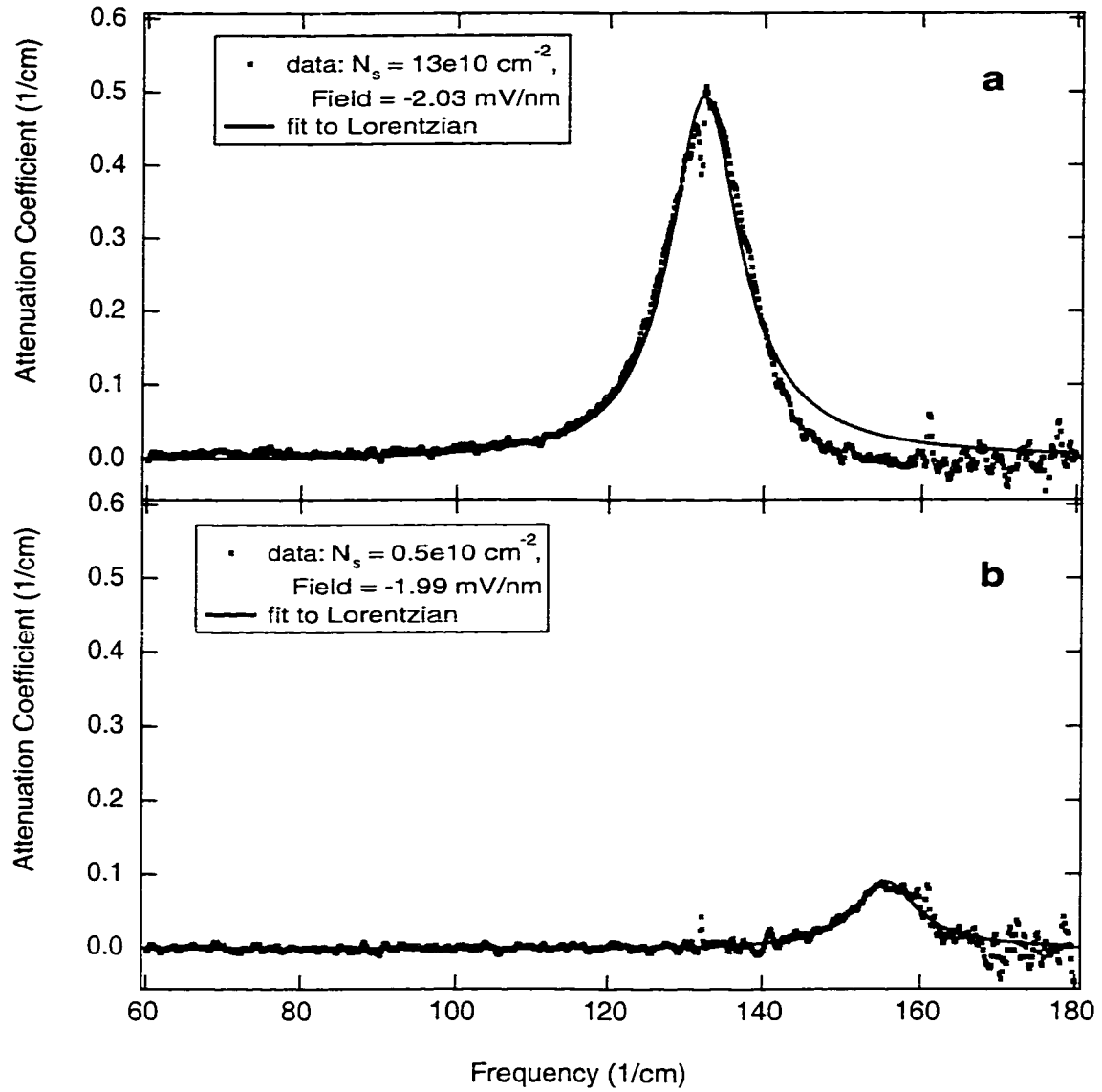
Figure 6.7: Spectra measured away from flat-band. a) $N_s = 13 \times 10^{10} \mathrm{cm}^{-2}$ b) $N_s = 0.5 \times 10^{10} \mathrm{cm}^{-2}$.
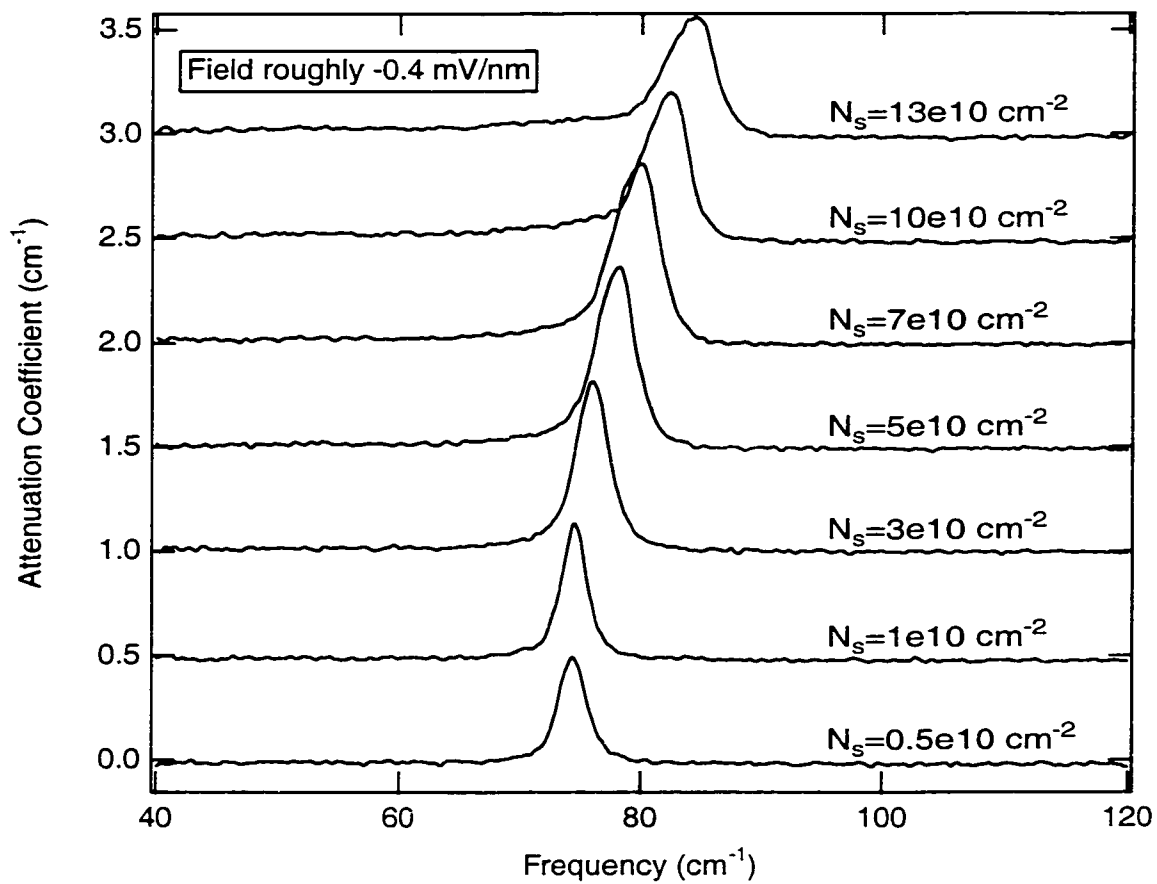
Figure 6.8: Spectra measured at various charge densities, near flat-band. The curves are offset for clarity.
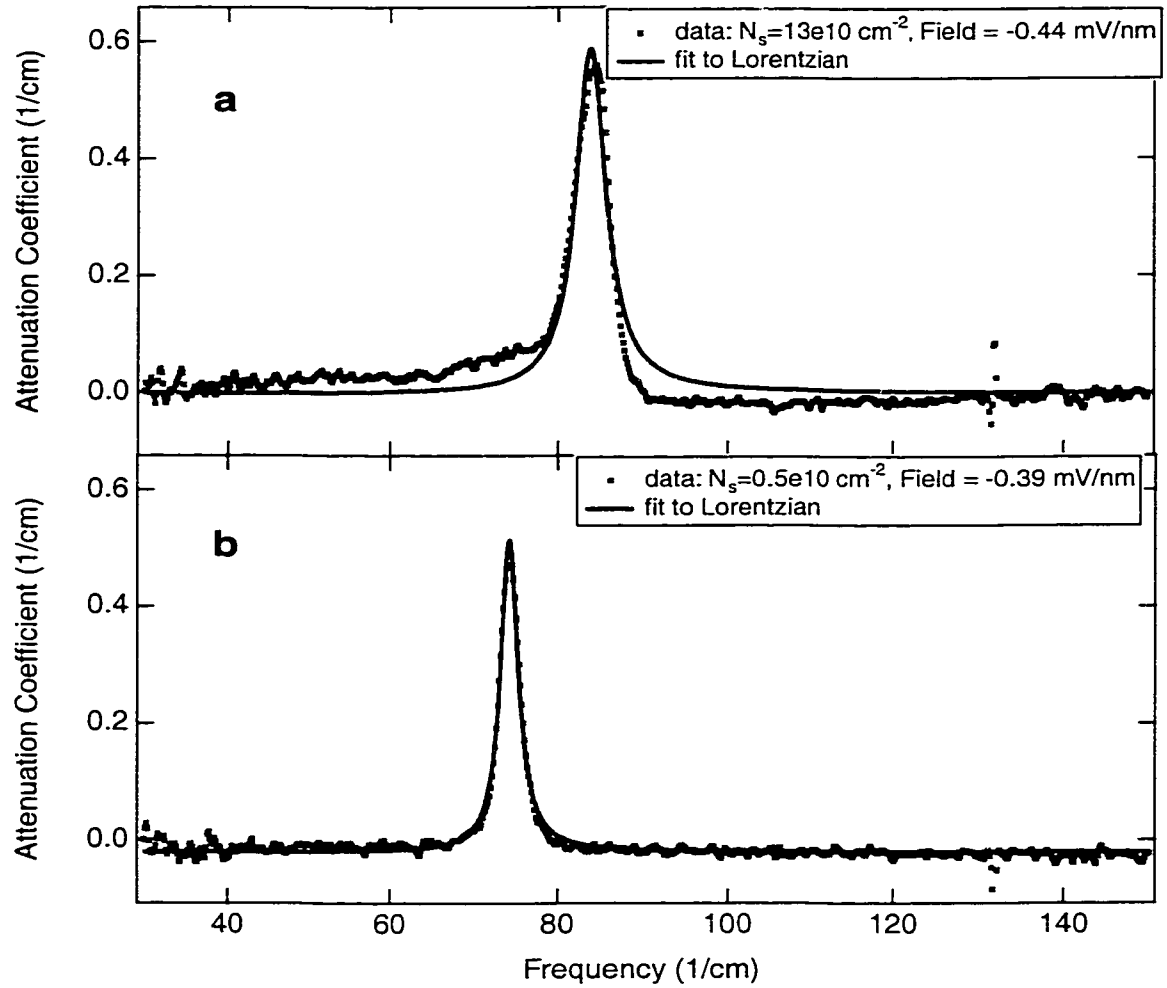
Figure 6.9: Spectra measured near flat-band. a) $N_s = 13 \times 10^{10} \mathrm{cm}^{-2}$ b) $N_s = 0.5 \times 10^{10} \mathrm{cm}^{-2}$.

line is quite symmetric at low density, and as the charge density is increased, the absorption line becomes asymmetric. In Figure 6.9, I replot curves for the lowest ($N_s = 0.5 \times 10^{10}\mathrm{cm}^{-2}$) and highest ($N_s = 13 \times 10^{10}\mathrm{cm}^{-2}$) charge density, along with the curve fits to Lorentzians. The absorption line at low charge density is well fit by the Lorentzian. At high charge density, the absorption line deviates strongly from the Lorentzian shape.

Back when Keith Craig observed the non-monotonic behavior of the density-dependent absorption strength, he speculated that it may be due to some effect of the waveguide. I was concerned that if the waveguide affected the absorption strength so strongly, it might also skew my linewidth data.

In order see whether the waveguide seriously affected the basic trends in the absorption data, I removed the metal cladding from the sample and did an absorption experiment in the Brewster-angle transmission geometry (the geometry is shown in Figure 4.3.2 in Chapter 4). Since the frontgate was now removed, I only had a backgate with which to control the electron gas. This meant of course that I could not vary the field and charge density independently. However I could still see if the behavior of the absorption strength vs. density was the same, and if the linewidth still had the same characteristic behavior near flat-band.

The spectra are shown in Figure 6.10. The largest absorption peak corresponded to an absorption of about 1%. The fit parameters are shown in Figure 6.11. Although we have a smaller range of fields to look at, we can see that we pass through flat-band and that the linewidth still has a minimum there. We also see that the absorption strength is non-monotonic in the charge density, as in the measurements in the edge-coupling geometry. The smallest linewidth looks smaller than anything I had previously observed, however. I concluded that while the waveguide may affect the value of the linewidth, the general trends, and the conclusions I draw from them, remain the same.
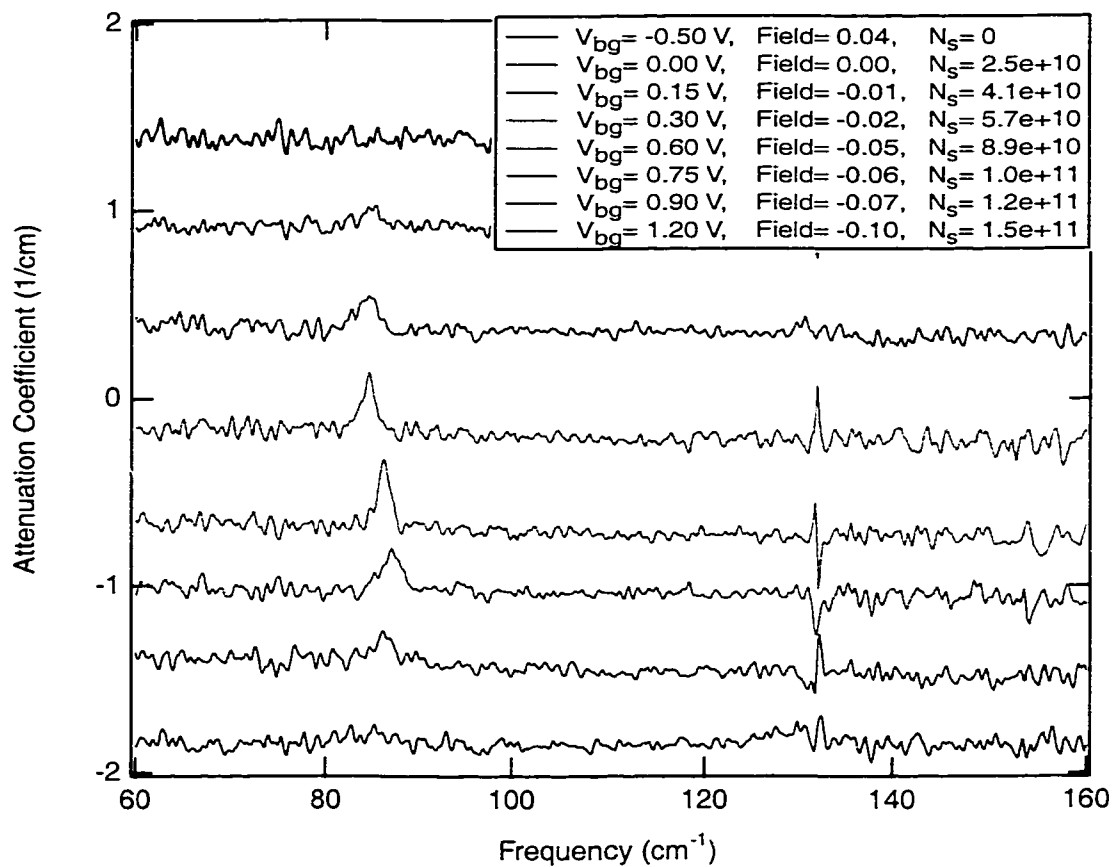
Figure 6.10: Spectra measured in the Brewster angle transmission experiment. The field is in units of mV/nm. The charge density N_s is in units of $10^{10} \mathrm{cm}^{-2}$. The curves are offset for clarity.
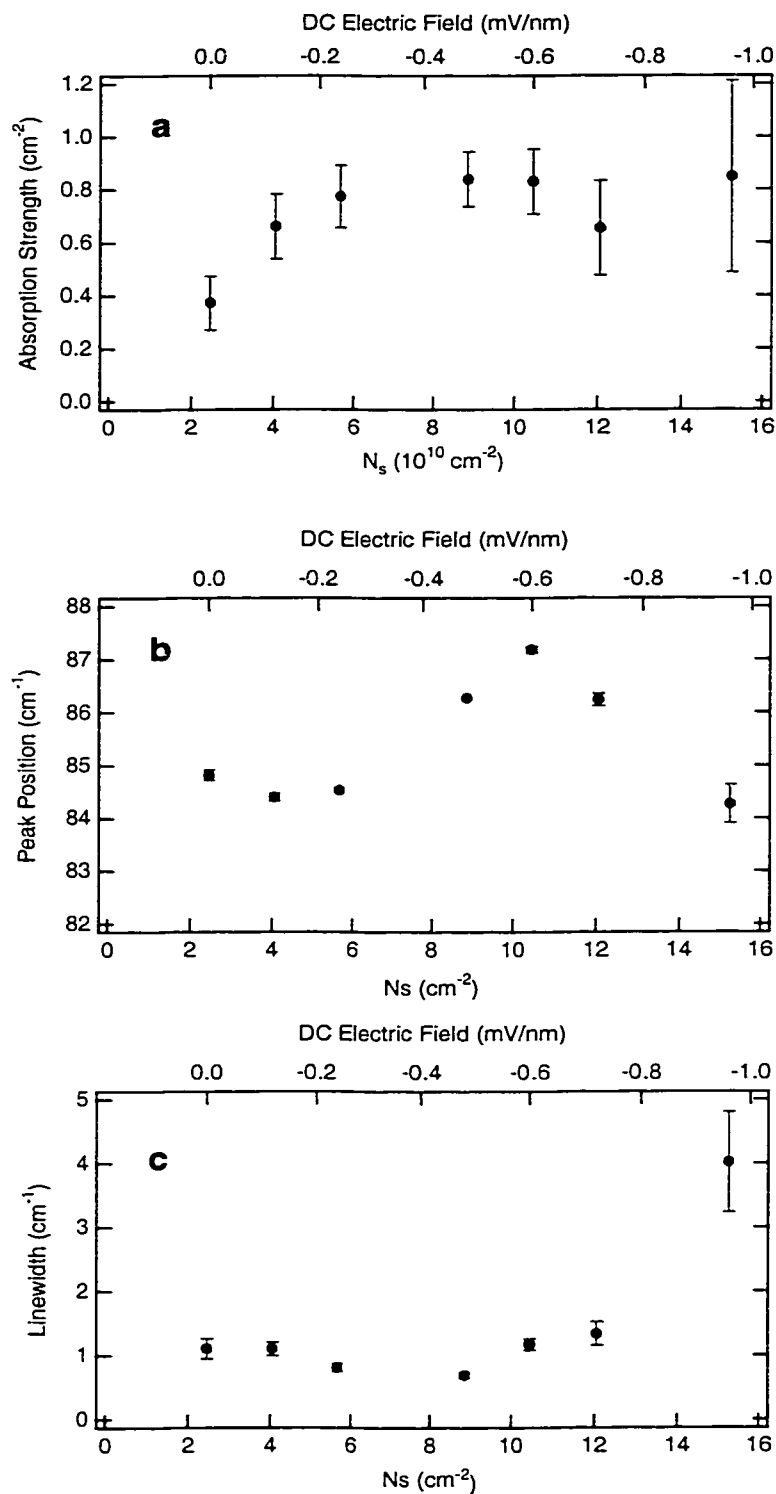
Figure 6.11: Fit parameters for the Brewster angle transmission experiment: a) absorption strength b) linewidth c) peak position
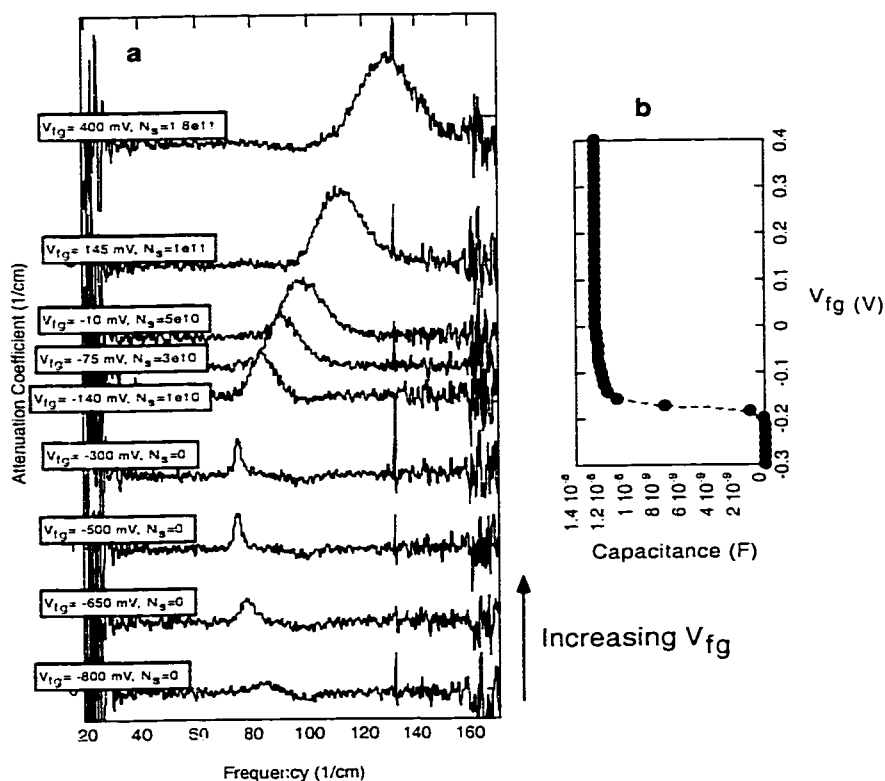
Figure 6.12: a) Absorption spectra for different values of frontgate voltage. at constant backgate voltage. The curves are offset for clarity. The baseline height of each curve corresponds to the frontgate voltage, and matches the scale in the C-V curve on the right. b) C-V measured at the same backgate voltage. Note that even at frontgate voltages less than −0.2 V. where the C-V depletes. there is an absorption.

6.1.2 Absorption in the "depleted" well

One of the interesting things I observed was that a sample which appears to be depleted from the C-V data can still absorb THz (see Figure 6.12). This is probably because there are electrons still in the well in localized states. Electrons in localized states would not contribute to the C-V signal, but could still undergo intersubband transitions.

I did some careful measurements of the absorption by the depleted well.
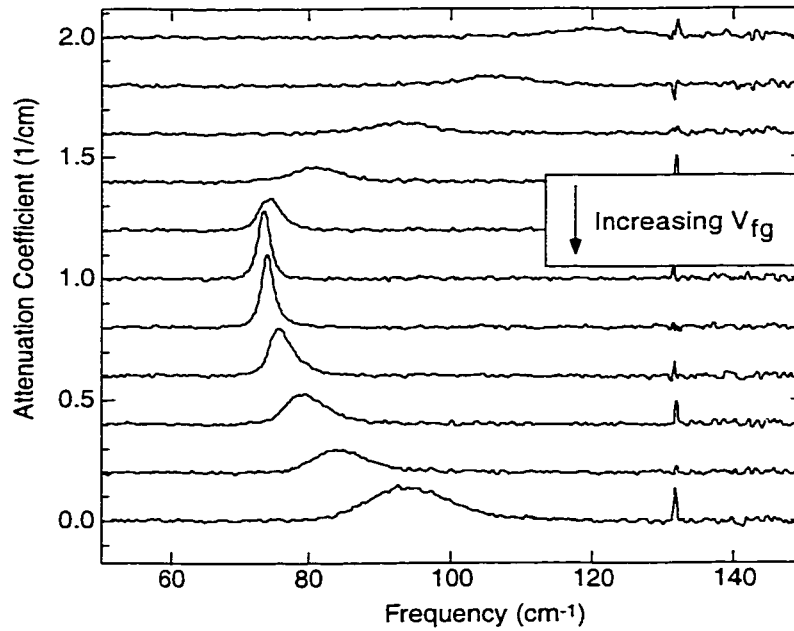
Figure 6.13: Absorption spectra in the depleted well for different values of frontgate voltage, at constant backgate voltage. The curves are offset for clarity.

Typical spectra are shown in Figure 6.13. In these measurements, I fixed the backgate voltage and measured spectra at different values of the frontgate voltage in the regime where the C-V measurements indicated that the well was depleted. In this regime, the quantum well ohmic contact is not connected to the charges localized in the well. Therefore, the charge density should be independent of the gate voltages, and the electric field should depend only on the difference between the gate voltages. Explicitly, the field is $\frac{V_{fg}-V_{bg}}{d_{fg}+d_{bg}}$, where $(d_{fg}+d_{bg})$ is the total distance between the frontgate and the backgate. This formula differs from that used in the full well.

Parameters of the absorption line are extracted from the curve fits, and are shown in Figure 6.14. I did the measurements of spectra vs. frontgate voltage as shown in Figure 6.13, and repeated for three different backgate voltages. We see that the data for the different backgate voltages overlap very closely, which confirms
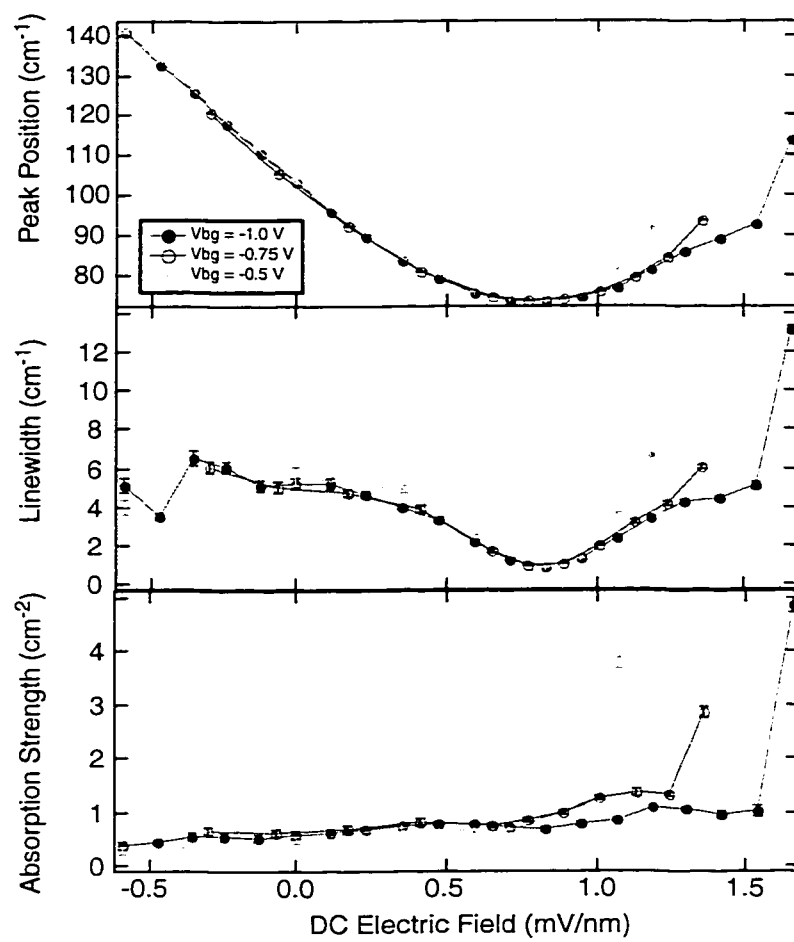
Figure 6.14: Peak position, linewidth, and absorption strength in the depleted well. from fits to the spectra.

my equation for the electric field in the depleted well. At certain positive fields, the absorption strength shoots upward. This occurs when the well is just barely depleted, so there may be somewhat more charge in the well than for the rest of the data.

6.2 Mobility data

The in-plane mobility is plotted in Figure 6.5c. The mobility was actually slightly anisotropic, but only at the lowest charge densities; I have plotted the geometric mean of the two in-plane components of the mobility tensor. The mobility does not show a maximum at flat-band, and is indeed uncorrelated to the intersubband dissipation time. The mobility also shows an asymmetry about flat-band, being higher for positive field than for negative field.

6.3 Scattering mechanisms

I interpret both the ISB dissipation and mobility data in terms of scattering from disorder in the well. The main sources of disorder in the $GaAs/Al_{0.3}Ga_{0.7}As$ quantum well are ionized impurities in the delta-doping layers, interface roughness (due to non-uniform well width on a short length scale), alloy disorder in the $Al_{0.3}Ga_{0.7}As$ barriers, and bulk impurities in the well. Remote impurities are far enough from our well to have little influence. Due to the short-range nature of the interface roughness (IFR) and alloy disorder potentials, one expects scattering from such potentials to be strong only when the wavefunctions strongly overlap with the interface and penetrate the barriers, as is the case away from flat-band. Thus, the IFR and alloy disorder scattering rates are greatly decreased at flat-band. The bulk impurity distribution is largely due to the segregation of impurities from the delta-doped layer during growth [15]. It is monotonically decreasing in the growth direction and can extend into the well. When a negative field is applied to the well,
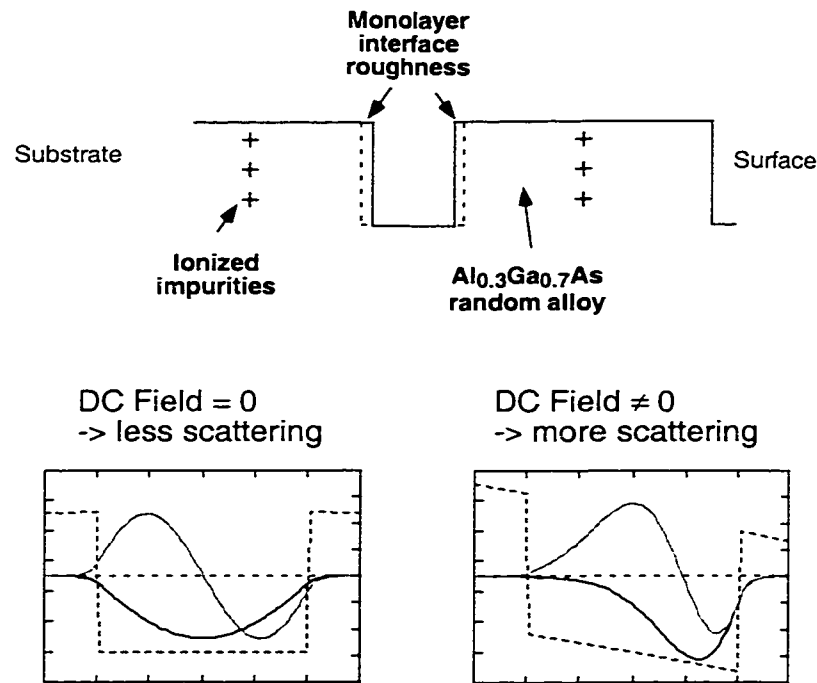
Figure 6.15: Sources of disorder scattering in the wide quantum well.

electrons are pushed towards the substrate and experience a higher local impurity density. Thus, bulk impurity scattering is greater at negative fields than at positive fields.

The field dependence of the data indicates which scattering mechanisms determine the ISB plasmon dissipation and the mobility. The expected field dependence of IFR and alloy disorder scattering is consistent with the peak in the measured ISB plasmon dissipation time, seen in Figure 6.5b. Reference [4] indicates that alloy disorder can be ignored, so we conclude that the ISB plasmon dissipation is dominated by IFR scattering. The expected field dependence of the bulk impurity scattering rate qualitatively explains the asymmetry in the field dependence of the mobility, seen in Figure 6.5c. I concluded that the mobility is limited by bulk
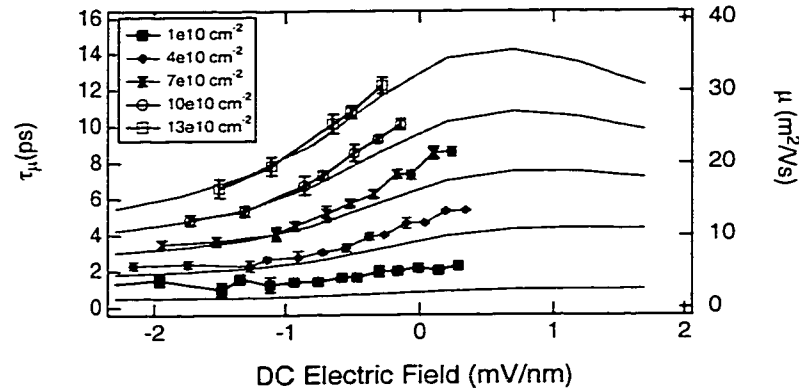
Figure 6.16: Measured and calculated mobilities, including all three scattering mechanisms. The bulk ionized impurity density was assumed to be $\rho(z) = 1.33 \times 10^{15}$ cm$^{-3} \times e^{-z/20nm}$. The ionized impurity densities were assumed to be 8×10^{10} cm^{-2} for the donor layer below the well, and 4.8×10^{11} cm^{-2} for the donor layer above the well. The interface roughness is assumed to be Gaussian correlated with average height $\Delta = 0.31$ nm and correlation length $\xi = 3.4$ nm.

impurity scattering.

6.4   Calculation of the mobility

In order to get a better idea of how the various scattering mechanisms work and how they manifest themselves, I calculated the mobility. The transport scattering rate was calculated in the Born approximation, including quasi-2D linear Thomas-Fermi screening. The calculation is compared to the data in Figure 6.16. The mobility is inversely proportional to the transport scattering rate. The details of the calculation are given in Appendix B. The IFR scattering was calculated assuming Gaussian-correlated roughness characterized by an average height $\Delta = 0.31$ nm and correlation length $\xi = 3.4$ nm (see Appendix B for a definition of the correlation function). These were the parameters that best fit the linewidth data in Carsten Ullrich's calculations, which are described in Section 6.5. Scattering from remote ionized impurities in the delta-doped layers was calculated assuming a sheet
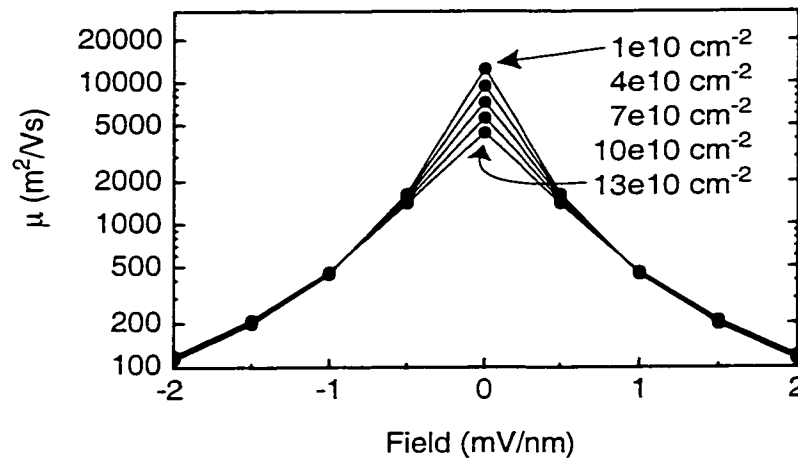
Figure 6.17: Calculated mobility limited by interface roughness scattering. The interface roughness is assumed to be Gaussian correlated with average height $\Delta = 0.31$ nm and correlation length $\xi = 3.4$ nm.

density of ionized donors of 4.8×10^{11} cm^{-2} in the upper layer. The lower layer was treated as a bulk distribution which had segregated towards the surface during growth. Scattering from these bulk impurities was calculated assuming a distribution given by $\rho(z) = 1.33 \times 10^{15} \times e^{-z/30\text{nm}}$ cm^{-3}, where the zero of z lies in the middle of the well. The origin of this type of distribution was already discussed. The parameters were chosen to give the best fit to the mobility data, and is consistent with measured distributions reported by other authors [15]. The mobility calculation is dominated by scattering from the bulk impurities, although we do see that at positive tilt, where the electron distribution is tilted towards the surface and thus the bulk impurity distribution it sees is somewhat lowered, the interface roughness begins to limit the mobility.

I've plotted separately the various contributions to the mobility in Figures 6.17, 6.18, and 6.19, so that one can better understand how they work and how they manifest themselves.
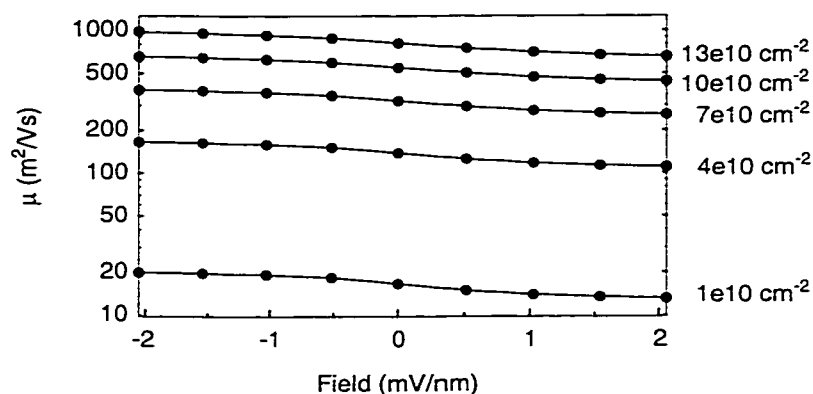
Figure 6.18: Calculated mobility limited by remote ionized impurity scattering. The ionized impurity densities were estimated to be 8×10^{10} cm^{-2} for the donor layer below the well, and 4.8×10^{11} cm^{-2} for the donor layer above the well.

6.4.1   Contribution from interface roughness

In Figure 6.17, the calculated mobility shows a sharp maximum at flat-band. From Equation B.1.1 in Appendix B, one sees that the scattering rate from a single rough interface is proportional to the square of the value of the wavefunction at the interface. Thus, the scattering rate is minimized at flat-band because that is where the wavefunctions have the smallest overlap with the interface.

Even at non-zero field, the mobility calculated for this set of parameters is much higher than what I measured. In order to get this calculation to agree with the data at non-zero field, I would have to assume an average height of the interface roughness of about 10 Å, which is much larger than one would expect for these samples. Because of this and the fact that the field dependence is all wrong, I concluded that interface roughness scattering does not make a significant contribution to the transport scattering rate.
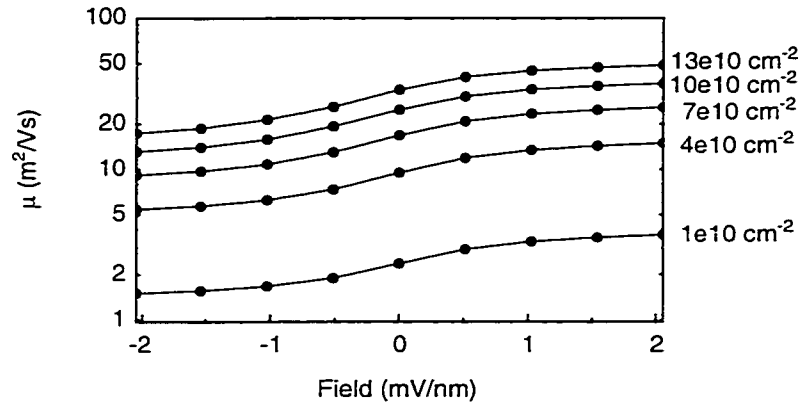
Figure 6.19: Calculated mobility limited by bulk ionized impurity scattering. The bulk ionized impurity density was assumed to be $\rho(z) = 10^{15}$ cm$^{-3} \times e^{-z/20nm}$.

6.4.2 Contribution from remote ionized impurities

The remote doping layers are far enough from the quantum well that they don't contribute much to the transport scattering rate. We see in Figure 6.18 that the contribution is negligible except at the lowest electron sheet density. In this calculation, I assumed there were sheets of ionized donors both above and below the well, but the lower donor layer should be left out of the total calculation because it comprises the bulk impurity distribution, which is treated separately. The mobility is lower for positive field than for negative field because the upper donor layer has a higher ionization density than the lower layer. Thus tilting the well towards the surface brings the electrons nearer to a high density of ionized impurities, and the mobility thus decreases.

6.4.3 Contribution from bulk ionized impurities

Bulk impurities in the well make the largest contribution to the transport scattering rate. As discussed above, when a negative field is applied to the well, electrons are pushed towards the substrate and experience a higher local impurity

density, which decreases the mobility. This effect qualitatively explains asymmetry in the field dependence of the mobility, seen in Figure 6.5c. The mobility in Figure 6.19 was calculated assuming a bulk ionized impurity density of $\rho(z) = 10^{15}$ cm^{-3} × $e^{-z/20nm}$. I got the best agreement with the data by multiplying that density by a factor of 1.33.

6.5 Comparison to a new theory

We had the pleasure of collaborating with Carsten Ullrich and Giovanni Vignale, who were working on a theory [20, 19] which could explain my linewidth data. Their theory calculates the linewidth of the intersubband plasmon in the framework of time-dependent density functional theory. Line broadening in the theory comes from two sources: disorder, mostly due to interface roughness, and by "intrinsic" effects of the electron-electron interaction. ("Intrinsic" in this case means that such line broadening occurs even in the absence of disorder). The work is significant because it is apparently the first successful microscopic theory of the intersubband linewidth.

Figure 6.20 shows the results of the theory, with and without disorder. Interface roughness was assumed to be Gaussian correlated with an average height $\Delta = 0.31$ nm and a correlation length $\xi = 3.25$ nm. Scattering from remote ionized impurities in the delta-doped layers was calculated assuming a sheet density of ionized donors of 4.8×10^{11} cm^{-2} in the upper layer. The lower layer was treated as a bulk distribution which had segregated towards the surface during growth. Scattering from these bulk impurities was calculated assuming a distribution given by $\rho(z) = 0.75 \times 10^{15} \times e^{-z/30nm}$ cm^{-3}, where the zero of z lies in the middle of the well. The theory (including disorder) agrees well with the data near flat-band, and in general reproduces the basic trends in the data. The theoretical curves shown in Figure 6.20c do not saturate off of flat-band, probably because they were calculated for an approximate form of the theory (which was used instead of the full form
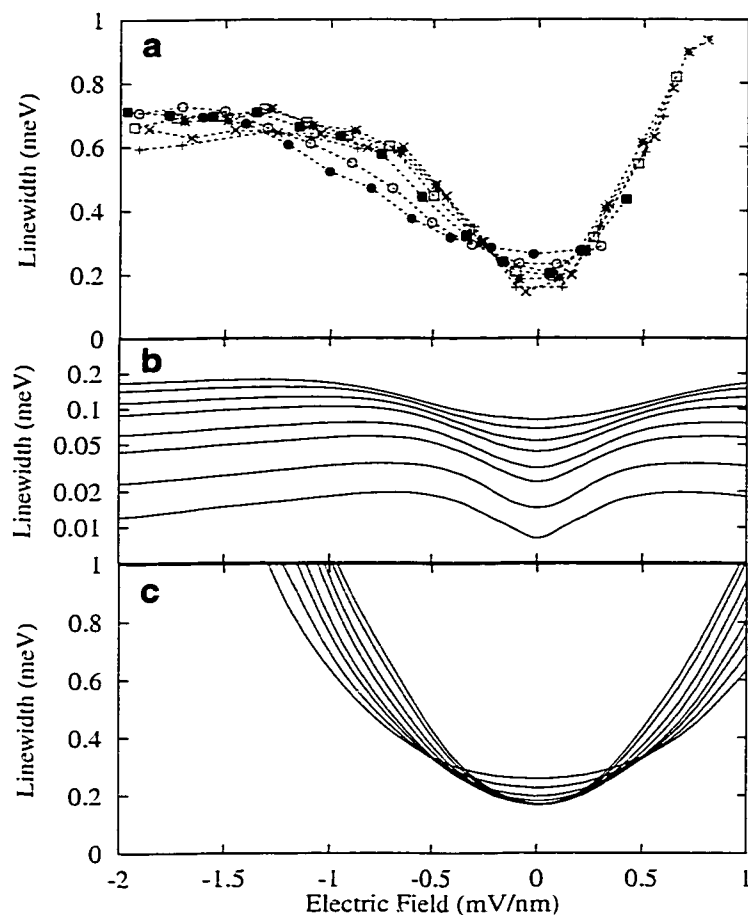
Figure 6.20: Results of the linewidth theory with both interface roughness and impurities included. compared to experiment. a) Experiment. b) Intrinsic linewidth (as above. but this time on a logarithmic scale). c) Including interface roughness. remote impurities, and bulk impurities. (Courtesy Carsten Ullrich).

in order to save computation time). Note that one must assume a bulk impurity density somewhat smaller than what was used for the mobility calculation. We still consider this to be in reasonable agreement with the parameters used in the mobility calculation.

There are several interesting results of the theory. One is that it supports the conclusion that the interface roughness dominates the line broadening, even while my mobility data and simulations show that the mobility is dominated by bulk impurity scattering. Another important point is that there is a finite linewidth even in a well with no rough interfaces or any other kind of disorder. This gives the ultimate limit to the linewidth that could in principle be achieved.

Chapter 7

Conclusions

This dissertation has presented detailed measurements of the mobility and intersubband linewidth of electrons in a quantum well, in which the charge density and dc electric field were varied independently. Calculations of the mobility were also discussed.

An immediate consequence of this work is that the knowledge described in this dissertation can be used by our group in the development of a new kind of THz detector, the tunable antenna-coupled intersubband terahertz (TACIT) detector. Much was learned about how to process and control the backgated samples. The issue of the density dependence of the absorption strength is also obviously important for device applications. More was discovered about the strange behavior of the absorption strength, e.g. that it is not a waveguide effect, although the issue was not resolved. The residual absorption by the "depleted" well was closely examined, which may be useful for TACIT work.

The introduction of the backgated samples was crucial to this work. The mobility and linewidth depended strongly on both the field and the density, and the use of a backgate and a frontgate were necessary in order to separate out the two effects. Once this was done, it was found that some basic trends, as well as actual numbers, in the field dependence reveal a lot about what goes on in the well.

In the sample that was studied most closely, the field dependence of the linewidth shows that the line is homogeneously broadened and dominated by interface roughness scattering. The field dependence of the mobility shows that is dominated by scattering from bulk impurities in the well.

These results are really sample dependent, to some extent. For example, one could make a sample with high enough bulk impurity concentration that the linewidth and mobility are indeed dominated by the bulk impurity scattering, and then their behavior could well correlate. However, some generalizations can be made that are of greater significance. First, the mobility, often used to characterize the quality of a sample, is not *necessarily* correlated with the linewidth. The linewidth and mobility may both be affected by the same scattering mechanisms, but each responds to a particular mechanism to a different degree. Hence, for infrared devices the mobility is not a reliable characterization. Second, the good agreement between linewidth data and theory for this particular sample gives one confidence in the theory, which is significant from a basic physics point of view.

One consequence of the theory, of significance for device design, is that it sets a lower limit to the linewidth, which can't be beaten even in a perfectly clean well. Furthermore, a better understanding of how disorder increases the linewidth above this intrinsic limit should help designers optimize device performance.

Bibliography

[1] L. Allen and J. H. Eberly. *Optical Resonance and Two-Level Atoms.* Dover, 1987.

[2] P. Bakshi, K. Kempa, A. Scorupsky, C. G. Du, G. Feng, R. Zobl, G. Strasser, C. Rauch, Ch. Pacher, K. Unterrainer, and E. Gornik. Plasmon-based terahertz emission from quantum well structures. *Applied Physics Letters,* 75:1685–1687, 1999.

[3] Gerald Bastard. *Wave Mechanics Applied to Semiconductor Heterostructures.* Les Editions de Physique, 1988.

[4] K. L. Campman, H. Schmidt, A. Imamoglu, and A. C. Gossard. Interface roughness and alloy-disorder scattering contributions to intersubband transition linewidths. *Applied Physics Letters,* 69:2554–2556, 1996.

[5] C. L. Cates, G. Briceno, M. S. Sherwin, K. D. Maranowski, and A. C. Gossard. A concept for a tunable antenna-coupled intersubband terahertz (tacit) detector. *Physica E,* 2:463–467, 1997.

[6] Keith Allen Craig. *Experimental Investigation of Nonlinear Intersubband Absorption and Many-Body Effects in Gallium Arsenide Quantum Wells in the Far-Infrared.* PhD thesis, University of California, Santa Barbara, 1997.

[7] John H. Davies. *The Physics of Low-Dimensional Semiconductors:An Introduction.* Cambridge University Press, 1998.

[8] E. B. Dupont, D. Delacourt, D. Papillon, J. P. Schnell, and M. Papuchon. Influence of ionized impurities on the linewidth of intersubband transitions in gaas/algaas quantum wells. *Applied Physics Letters,* 60:2121–2122, 1992.

[9] Jerome Faist, Carlo Sirtori, Federico Capasso, Loren Pfeiffer, and Ken W. West. Phonon limited intersubband lifetimes and linewidths in a two-dimensional electron gas. *Applied Physics Letters,* 64:872–874, 1994.

[10] Guy Fishman and Daniel Calecki. Surface-induced resistivity of ultrathin metallic films: A limit law. *Physical Review Letters,* 62:1302–1305, 1989.

[11] Bryan Galdrikian. *Nonlinear and Nonperturbative Dynamics in Quantum Wells.* PhD thesis, University of California, Santa Barbara, 1994.

[12] Peter R. Griffiths and James A. de Haseth. *Fourier Transform Infrared Spectrometry.* John Wiley and Sons, 1986.

[13] Manfred Helm. The basic physics of intersubband transitions. In H. C. Liu and Federico Capasso, editors, *Intersubband Transitions in Quantum Wells: Physics and Device Applications I,* volume 62, chapter 1, pages 1–99. 2000.

[14] J. N. Heyman, K. Unterrainer, K. Craig, B. Galdrikian, M. S. Sherwin, K. Campman, P. F. Hopkins, and A. C. Gossard. Temperature and intensity dependence of intersubband relaxation rates from photovoltage and absorption. *Physical Review Letters,* 74:2682–2685, 1995.

[15] L. Pfeiffer, E. F. Schubert, K. W. West, and C. W. Magee. Si dopant migration and the algaas/gaas inverted interface. *Applied Physics Letters,* 58:2258–2260, 1991.

[16] A. A. Ramadan, R. D. Gould, and A. Ashour. On the van der pauw method of resistivity measurements. *Thin Solid Films*, 239:272–275, 1994.

[17] Michel Rochat, Jérôme Faist, Mattias Beck, and Ursula Oesterle. Electrically pumped terahertz quantum well sources. *Physica E*, 7:44–47, 2000.

[18] A. M. Tomlinson, C. C. Chang, R. J. Stone, R. J. Nicholas, A. M Fox, M. A. Pate, and C. T. Foxon. Intersubband transitions in gaas coupled-quantum-wells for use as a tunable detector at thz frequencies. *Applied Physics Letters*, 76:1579–1581, 2000.

[19] C. A. Ullrich and G. Vignale. Collective intersubband transitions in quantum wells: A comparative density-functional study. *Physical Review B*, 58:15756–15765, 1998.

[20] G. Vignale, C. A. Ullrich, and S. Conti. Time-dependent density functional theory beyond the adiabatic local density approximation. *Physical Review Letters*, 79:4878–4881, 1997.

[21] R. J. Warburton, K. Weilhammer, J. P. Kotthaus, M. Thomas, and H. Kroemer. Influence of collective effects on the linewidth of intersubband resonance. *Physical Review Letters*, 80:2185–2188, 2000.

[22] W. T. Welford and R. Winston. *High Collection Nonimaging Optics*. Academic Press, 1989.

[23] Benjamin S. Williams, Bin Xu, and Qing Hu. Narrow-linewidth terahertz intersubband emission from three-level systems. *Applied Physics Letters*, 75:2927–2929, 1999.

Appendix A

Processing details

I got my cleanroom process from Charly Unterrainer when I started processing, and I've done a little to modify it. It was originally borrowed from someone in one of the engineering groups long ago.

Solvent clean

Cold ACE: 5 min.

Hot METH: 5 min.

Hot ISO: 5 min.

Running DI water: 3 min.

Blow dry with N_2.

Dehydration bake. 120 °C. 30 min.

Photoresist application

10 min. cool down after dehydration

Apply AZ4110 with syringe and filter

Spin at 5.5 krpm for 30 sec.

Hot plate bake at 95 °C, 1 min.

Exposure

10 min. cool down after bake

Expose to 7.5 mW for 15 sec.

Development

If this mask is for metal deposition, soak in toluene for 10 min., then blow dry with N_2.

45 sec. develop in 1:4::AZ 400:H2O

Rinse running DI water for 3 min.

Blow dry with N_2.

Etch

Mix etchant, 5.8 : 1 : 83 :: NH_4OH : H_2O_2 : H_2O. (I used 10.5 ml:1.8 ml:150 ml::NH_4OH : H_2O_2 : H_2O).

Dektak wafer to measure photoresist thickness.

Dip in 1 : 10 :: NH_4OH : H_2O for 20 sec.

Rinse in running DI for 3 min.

Etch in etchant.

Rinse in running DI for 3 min.

Blow dry with N_2.

Dektak to measure etch depth.

Repeat the last four steps until desired depth is reached.

Second photoresist application

Remove the photoresist with acetone and follow the above solvent cleaning procedure.

Apply photoresist for ohmic contact deposition, as above.

Ohmic contact deposition

Pump down the evaporator to at least 2×10^{-6} torr.

Deposit material: 108 Å Ge, 102 Å Au, 63 Å Ge, 236 Å Au. 100 Å Ni. 3000 Å Au

Liftoff

Soak in acetone for several hours (preferrably overnight).

Remove any extra metal by squirting the sample with acetone.

Rinse in ISO, DI.

Blow dry with N_2.

Rapid Thermal Anneal

The sample was annealed for 45 seconds at 430 °C, to diffuse the metal into the sample.

DI rinse.

Blow dry with N_2.

Frontgate metallization

Follow the above procedures for solvent cleaning, photoresist application. and development.

Pump down thermal evaporator to 5×10^{-7} torr.

Follow the above procedure for liftoff.

Backside metallization

Follow the above procedures for solvent cleaning, photoresist application, and development.

Pump down thermal evaporator to $\sim 1 \times 10^{-6}$ torr.

Follow the above procedure for liftoff.

Appendix B

Details of the mobility calculation

The standard way to calculate the mobility of a heterostructure is to use the relaxation time approximation, and calculate a scattering rate using the Born approximation. Screening of the scattering potential by the 2DEG is usually treated using quasi-2D linear Thomas-Fermi screening. I followed these conventions in calculating the mobility. Most of the theoretical framework is described in textbooks, so I will mostly refer to those results. I will derive those parts of the calculation that are peculiar to my system and that I have not found in the literature.

The mobility μ is defined by the relation

$$v = \mu E$$

where v is the average velocity of an electron in an electric field with magnitude E, in the diffusive transport regime. Experimentally, we determine the mobility by measuring the conductivity σ of the sample and using the relation

$$\sigma = n\mu$$

where n is the sheet density of carriers.

We calculate the mobility in the relaxation time approximation. The mobility is proportional to a transport scattering lifetime

$$\mu = \frac{e}{m} \langle \tau_{tr} \rangle$$

where $\langle \tau_{tr} \rangle$ is the transport lifetime averaged over the Fermi-Dirac distribution. At low temperatures, only those electrons at the Fermi surface contribute to the transport properties of the electron gas, so we evaluate the transport lifetime at the Fermi energy:

$$\langle \tau_{tr} \rangle = \tau_{tr}(E_F)$$

The problem is to calculate this lifetime.

The lifetime is given by the inverse of the transport scattering rate, calculated within the Born approximation. The transport scattering rate is given in equation 8.32 of Reference [7] for scattering from remote ionized impurities. For general isotropic scattering potential, that equation becomes (in the absence of screening):

$$\frac{1}{\tau_{tr}} = \frac{m^* A}{2\pi \hbar^3 k_F^3} \int_0^{2k_F} |V_{fi}|^2 \frac{q^2 dq}{\sqrt{1 - \left(\frac{q}{2k_F}\right)^2}}$$

where q is the momentum transfer, A is the sample area and V_{fi} is the scattering matrix element. To include screening, one divides the scattering matrix element by $\varepsilon(q)$, the dielectric function of the 2DEG.

When several mechanisms contribute to the total scattering rate, we add the individual rates incoherently to obtain the total scattering rate:

$$\frac{1}{\tau_{tr}} = \sum_i \left(\frac{1}{\tau_{tr}}\right)_i$$

B.1   Scattering matrix elements

I considered three sources of scattering: remote ionized impurities, bulk ionized impurities, and interface roughness.

The remote ionized impurities are in the delta-doping layers outside the well. The density can be calculated by considering the electrostatic situation during cool-down of the sample, taking into account the band offsets and so forth.

It is known that during growth, impurities from the delta-doped layer segregate in the growth direction, leading to a bulk impurity distribution which is monotonically decreasing in the growth direction and which can extend into the well [15]. When a negative field is applied to the well, electrons are pushed towards the substrate and experience a higher local impurity density, which decreases the mobility. This effect qualitatively explains asymmetry in the field dependence of the mobility, seen in Figure 6.5c.

Interface roughness is another way of saying that the well width is not uniform across the sample.

Born approximation

In the Born approximation, the initial and final states of the scattered particle are plane waves. In two dimensions, this means we take the states to be

$$
\phi_i(\mathbf{r}, z) = \frac{1}{\sqrt{A}} e^{i\mathbf{k}\cdot\mathbf{r}} \chi_i(z)
$$
$$
\phi_f(\mathbf{r}, z) = \frac{1}{\sqrt{A}} e^{i(\mathbf{k}+\mathbf{q})\cdot\mathbf{r}} \chi_f(z)
$$

where $\chi_{i(j)}(z)$ is the envelope function of the initial (final) state, and A is the sample area. The matrix element is:

$$
\begin{aligned}
V_{fi} &= \int d^2r \; dz \; \phi_f^*(\mathbf{r}, z) V(\mathbf{r}, z) \phi_i(\mathbf{r}, z) \\
&= \frac{1}{A} \int d^2r \; dz \; e^{-i(\mathbf{k}+\mathbf{q})\cdot\mathbf{r}} \; \chi_f^*(z) \; V(\mathbf{r}, z) \; e^{i\mathbf{k}\cdot\mathbf{r}} \; \chi_i(z) \\
&= \frac{1}{A} \int d^2r \; dz \; e^{-i\mathbf{q}\cdot\mathbf{r}} \chi_f^*(z) V(\mathbf{r}, z) \chi_i(z)
\end{aligned}
$$

Remote ionized impurities

Suppose we have a single impurity located at $(\mathbf{r}, z) = (\mathbf{0}, d)$. The perturbation Hamiltonian is

$$V(\mathbf{r}, z) = \frac{-e^2}{4\pi\epsilon_0\epsilon_b} \frac{1}{\sqrt{r^2 + (z - d)^2}}$$

The Born approximation matrix element is

$$
\begin{aligned}
V_{fi} &= \frac{-e^2}{4\pi\epsilon_0\epsilon_b} \frac{1}{A} \int d^2r \; dz \; e^{-i\mathbf{q}\cdot\mathbf{r}} \frac{1}{\sqrt{r^2 + (z - d)^2}} |\chi(z)|^2 \\
&= \frac{-e^2}{4\pi\epsilon_0\epsilon_b} \frac{1}{A} \int dz \; |\chi(z)|^2 \int d^2r \; \frac{e^{-i\mathbf{q}\cdot\mathbf{r}}}{\sqrt{r^2 + (z - d)^2}} \\
&= \frac{-e^2}{2\epsilon_0\epsilon_b} \frac{1}{A} \int dz \; |\chi(z)|^2 \frac{e^{-q|z-d|}}{q}
\end{aligned}
$$

where q is assumed positive. Let's define $K(q) = \int dz \; |\chi(z)|^2 e^{-qz}$, which is valid for positive or negative q.

For $d < 0$ and $d < z$ (i.e. donors far to the left of the well), we have $(z - d) > 0$ and thus $|z - d| = z + |d|$. Then we get

$$
\begin{aligned}
V_{fi} &= \frac{-e^2}{2\epsilon_0\epsilon_b} \frac{1}{A} \frac{e^{-q|d|}}{q} \int dz \; |\chi(z)|^2 e^{-qz} \\
&= \frac{-e^2}{2\epsilon_0\epsilon_b} \frac{1}{A} \frac{e^{-q|d|}}{q} K(q)
\end{aligned}
$$

For the case of $d > z$ and $d > 0$ (i.e. donors far to the right of the well), we have $(z - d) < 0$ and thus $|z - d| = -z + |d|$, and therefore

$$
\begin{aligned}
V_{fi} &= \frac{-e^2}{2\epsilon_0\epsilon_b} \frac{1}{A} \frac{e^{-q|d|}}{q} \int dz \; |\chi(z)|^2 e^{qz} \\
&= \frac{-e^2}{2\epsilon_0\epsilon_b} \frac{1}{A} \frac{e^{-q|d|}}{q} K(-q)
\end{aligned}
$$

To get the total scattering rate due to a layer of ionized impurities, we should multiply the scattering rate by the number of scattering centers, $n_{imp}A$, where n_{imp} is the 2D density of scatterers. If we have donor layers on either side of the well,

located at $d_1 < 0$ (far to the left) and $d_2 > 0$ (far to the right) we add the scattering rates due to each layer. We then get

$$\frac{1}{\tau_{tr}} = \frac{m}{2\pi\hbar^3} \left(\frac{e^2}{2\epsilon_0\epsilon_b}\right)^2 \left(n_{imp,1} \frac{1}{k_F^3} \int_0^{2k_F} \frac{e^{-2q|d_1|}}{q^2} (K(q))^2 \frac{q^2 dq}{\sqrt{1-\left(\frac{q}{2k_F}\right)^2}} \right.$$

$$\left. + n_{imp,2} \frac{1}{k_F^3} \int_0^{2k_F} \frac{e^{-2q|d_2|}}{q^2} (K(-q))^2 \frac{q^2 dq}{\sqrt{1-\left(\frac{q}{2k_F}\right)^2}} \right)$$

Bulk impurities

For remote impurities it was convenient to define $K(q) = \int dz \, |\chi(z)|^2 e^{-qz}$, but now that's not convenient because we can have d lie in the middle of the well.

In general we have

$$V_{fi} = \frac{-e^2}{2\epsilon_0\epsilon_b} \frac{1}{A} \frac{1}{q} \int dz \, |\chi(z)|^2 e^{-q|z-d|}$$

$$= \frac{-e^2}{2\epsilon_0\epsilon_b} \frac{1}{A} \frac{1}{q} L(q; d)$$

where we have defined

$$L(q; d) = \int dz \, |\chi(z)|^2 e^{-q|z-d|}$$

As in the case of the remote impurities, the scattering rate due to a layer of area density n_{imp} located at $z = d$ is

$$\frac{1}{\tau_{tr}} = \frac{m}{2\pi\hbar^3} \left(\frac{1}{k_F^3} \int_0^{2k_F} \left(\frac{-e^2}{2\epsilon_0\epsilon_b} \frac{1}{q} L(q; d) \right)^2 \frac{n_{imp}q^2 dq}{\sqrt{1-\left(\frac{q}{2k_F}\right)^2}} \right)$$

We should integrate the scattering rate over all impurity layers (which comprise the bulk impurity density). We can take $n_{imp}(d) = dd \, \rho_{imp}^{(3D)}(d)$, where dd is the infinitesimal element of length, and $\rho_{imp}^{(3D)}(d)$ is the d-dependent bulk impurity density.

So the quantity in parentheses (which is proportional to the scattering rate) should
be integrated over d, so that the scattering rate becomes

$$\frac{1}{\tau_{tr}} = \frac{m}{2\pi\hbar^3 \, k_F^3} \left(\frac{-e^2}{2\epsilon_0\epsilon_b}\right)^2 \int_{-\infty}^{\infty} dd \int_0^{2k_F} \frac{1}{q^2} \, (L(q;d))^2 \, \frac{\rho_{imp}^{(3D)}(d) \, q^2 dq}{\sqrt{1 - \left(\frac{q}{2k_F}\right)^2}}$$

Reversing the order of integration, we have

$$\frac{1}{\tau_{tr}} = \frac{m}{2\pi\hbar^3 \, k_F^3} \left(\frac{-e^2}{2\epsilon_0\epsilon_b}\right)^2 \int_0^{2k_F} \frac{1}{q^2} \frac{q^2 dq}{\sqrt{1 - \left(\frac{q}{2k_F}\right)^2}} \int_{-\infty}^{\infty} dd \, \rho_{imp}^{(3D)}(d) \, (L(q;d))^2$$

Let's give a name to the integral over d:

$$L(q) = \int_{-\infty}^{\infty} dd \, \rho_{imp}^{(3D)}(d) \, (L(q;d))^2$$

So now the scattering rate for bulk impurities can be written

$$\frac{1}{\tau_{tr}} = \frac{m}{2\pi\hbar^3 \, k_F^3} \left(\frac{-e^2}{2\epsilon_0\epsilon_b}\right)^2 \int_0^{2k_F} \frac{1}{q^2} L(q) \frac{q^2 dq}{\sqrt{1 - \left(\frac{q}{2k_F}\right)^2}}$$

Interface roughness

For interface roughness scattering, we need to know what the interface looks
like. Suppose the well width is d and assume the position of the interface has the
form

$$z_{int}(\mathbf{r}) = \pm d/2 + f(\mathbf{r})$$

where the roughness height function $f(\mathbf{r})$ has an average value of 0. It is characterized
by a height autocorrelation function,

$$\langle f(\mathbf{r}')f(\mathbf{r}' + \mathbf{r})\rangle = \frac{1}{A} \int d^2r' f(\mathbf{r}')f(\mathbf{r}' + \mathbf{r})$$

(where $\langle\rangle$ denotes an average over $\mathbf{r}'$.) The average roughness height Δ is defined by

$$\Delta^2 = \langle f(\mathbf{r}')f(\mathbf{r}')\rangle$$

and we can rewrite the autocorrelation function as

$$\langle f(\mathbf{r}')f(\mathbf{r}' + \mathbf{r})\rangle \equiv \Delta^2 G(\mathbf{r})$$

Reference [10] gives the following perturbation Hamiltonian for a single rough interface at $z = d/2$:

$$U(\mathbf{r}, z) = V \left(\Theta[z - d/2 - f(\mathbf{r})] - \Theta[z - d/2]\right) \approx -Vf(\mathbf{r})\delta(z - d/2)$$

The square of the scattering matrix element becomes

$$|U_{fi}|^2 = \frac{1}{A}[(-V)\chi^*(d/2)\chi(d/2)]^2 \int e^{-i\mathbf{q}\cdot\mathbf{r}}\langle f(\mathbf{r}')f(\mathbf{r}' + \mathbf{r})\rangle\, d^2r$$

Defining $A_1 = V\chi^*(d/2)\chi(d/2)$, we get

$$|U_{fi}|^2 = A_1^2 \frac{1}{A} \int e^{-i\mathbf{q}\cdot\mathbf{r}}\langle f(\mathbf{r}')f(\mathbf{r}' + \mathbf{r})\rangle\, d^2r$$

Reference [10] defines

$$\langle f(\mathbf{r}')f(\mathbf{r}' + \mathbf{r})\rangle = \Delta^2 G(r/\xi)$$

where ξ is a correlation length and $G(r/\xi)$ is dimensionless. If $F(q)$ is the 2D Fourier Transform of $G(r)$, then the FT of $G(r/\xi)$ is $\xi^2 F(\xi q)$. which is dimensionless (since the argument of G is dimensionless here.) We would typically have something like $G(r/\xi) = exp(-r^2/\xi^2)$, whose FT is given by $\xi^2 F(\xi q) = \pi\xi^2 exp(-\xi^2 q^2/4)$.

Now we get

$$|U_{fi}|^2 = A_1^2 \frac{1}{A}\Delta^2\xi^2 F(\xi q)$$

For two rough interfaces indexed 1 and 2 (which are not correlated with each other) we get

$$|U_{fi}|^2 = A_1^2 \frac{1}{A}\Delta_1^2\xi_1^2 F_1(\xi_1 q) + A_2^2 \frac{1}{A}\Delta_2^2\xi_2^2 F_2(\xi_2 q)$$

The scattering rate for interface roughness becomes

$$\frac{1}{\tau_{tr}} = \frac{m}{2\pi\hbar^3 k^3}\left(A_1^2\Delta_1^2\xi_1^2 \int_0^{2k} \frac{F_1(\xi_1 q)\; q^2 dq}{\sqrt{1 - (\frac{q}{2k})^2}} + A_2^2\Delta_2^2\xi_2^2 \int_0^{2k} \frac{F_2(\xi_2 q)\; q^2 dq}{\sqrt{1 - (\frac{q}{2k})^2}}\right) \quad \text{(B.1.1)}$$

B.2 Screening

I found the treatment of screening in the textbooks to be unclear for the quasi-2D case, so here I'll do the derivation in some detail.

External and induced charges

The total potential and total charge density are due to contributions from external sources (e.g. impurities) as well as induced charges, both from the bound charge of the background dielectric and from the rearrangement of mobile electrons of the electron gas. So we have

$$\phi(\mathbf{r}) = \phi_{ext}(\mathbf{r}) + \phi_b(\mathbf{r}) + \phi_e(\mathbf{r})$$

and a similar equation holds for Fourier space. The subscript "ext" denotes external charges, "b" denotes induced charge of the background dielectric, and "e" denotes induced charge of the electron gas.

Dielectric constant

Define the dielectric constant as follows. Apply an external potential to the 2DEG and assume that the total potential is linear in the external potential.

$$\phi_{ext}(\mathbf{r}) = \int d^3r' \ \epsilon(\mathbf{r} - \mathbf{r}')\phi(\mathbf{r}')$$

In Fourier space this becomes

$$\tilde{\phi}_{ext}(\mathbf{q}) = \tilde{\epsilon}(\mathbf{q}) \ \tilde{\phi}(\mathbf{q})$$

The task is to find the dielectric function, $\tilde{\epsilon}(\mathbf{q})$. The unscreened potential is simply $\tilde{\phi}_{ext}(\mathbf{q})$, and the screened potential which goes into the scattering calculations is $\tilde{\phi}(\mathbf{q})$, which is obtained by dividing the unscreened potential by the dielectric function.

The exact form of the external potential is unimportant, as we are here only trying to find the dielectric function. We just apply an external potential, calculate

the response of the 2DEG to that potential. and divide out the external potential to get the dielectric function. I'll use the Coulomb potential of an ionized impurity located outside of the well.

Dielectric susceptibility

Define a dielectric susceptibility χ as follows.

$$\tilde{\epsilon}(\mathbf{q}) = 1 + \tilde{\chi}(\mathbf{q}) = 1 + \tilde{\chi}_b(\mathbf{q}) + \tilde{\chi}_e(\mathbf{q})$$

So χ summarizes the response of the system to an applied field. and splits it into contributions from the background dielectric (χ_b) and from the electron gas (χ_e).

Here's how we relate the potentials to the susceptibilities:

$$\begin{aligned} \tilde{\epsilon}(\mathbf{q})\tilde{\phi}(\mathbf{q}) &= \tilde{\phi}_{ext}(\mathbf{q}) \\ &= \tilde{\phi}(\mathbf{q}) - \tilde{\phi}_e(\mathbf{q}) - \tilde{\phi}_b(\mathbf{q}) \end{aligned}$$

But

$$\tilde{\epsilon}(\mathbf{q})\tilde{\phi}(\mathbf{q}) = (1 + \tilde{\chi}(\mathbf{q}))\tilde{\phi}(\mathbf{q})$$

so we have

$$\tilde{\chi}(\mathbf{q})\tilde{\phi}(\mathbf{q}) = -\tilde{\phi}_e(\mathbf{q}) - \tilde{\phi}_b(\mathbf{q})$$

And since

$$\tilde{\chi}(\mathbf{q}) = \tilde{\chi}_b(\mathbf{q}) + \tilde{\chi}_e(\mathbf{q})$$

it makes sense to define

$$\begin{aligned} \tilde{\phi}_b(\mathbf{q}) &= -\tilde{\chi}_b(\mathbf{q})\tilde{\phi}(\mathbf{q}) \\ \tilde{\phi}_e(\mathbf{q}) &= -\tilde{\chi}_e(\mathbf{q})\tilde{\phi}(\mathbf{q}) \end{aligned}$$

Quasi-2D Thomas-Fermi screening

Assume (Ando, p. 447, equation 2.8) that the induced charge in the 2DEG is given by

$$\rho_e(\mathbf{r}, z) = -e^2 \; \bar{\phi}(\mathbf{r}) \; \frac{dn_0}{d\mu} \; g(z)$$

where n_0 is the Fermi distribution of states per unit area, $g(z) = |\chi(z)|^2$ is the probability density in the 2DEG, and $\bar{\phi}(\mathbf{r}) = \int_{-\infty}^{\infty} \phi(\mathbf{r}, z) \; g(z) \; dz$.

2D Poisson's equation

The Laplacian operator is:

$$\nabla^2 \phi(\mathbf{r}, z) = \frac{\partial^2}{\partial z^2} \phi(\mathbf{r}, z) + \nabla_r^2 \phi(\mathbf{r}, z)$$

In Fourier space, this becomes

$$\frac{\partial^2}{\partial z^2} \bar{\phi}(\mathbf{q}, z) - q^2 \bar{\phi}(\mathbf{q}, z)$$

where I've done a 2D Fourier transform of the in-plane variables.

The sources are as follows (assume the impurity is located at $(\mathbf{0}, d)$:

$$
\begin{aligned}
\rho_{ext}(\mathbf{r}, z) &= e\delta^2(\mathbf{r})\delta(z - d) \\
\rho_b(\mathbf{r}, z) &= -\epsilon_0 \nabla^2 \phi_b(\mathbf{r}, z) \\
\rho_e(\mathbf{r}, z) &= -e^2 \; \bar{\phi}(\mathbf{r}) \; \frac{dn_0}{d\mu} \; g(z)
\end{aligned}
$$

In Fourier space these become

$$
\begin{aligned}
\bar{\rho}_{ext}(\mathbf{q}, z) &= e\delta(z - d) \\
\bar{\rho}_b(\mathbf{q}, z) &= -\epsilon_0 \left(-q^2 \bar{\phi}_b(\mathbf{q}, z) + \frac{\partial^2}{\partial z^2} \bar{\phi}_b(\mathbf{q}, z) \right) \\
&= -\epsilon_0 \left(q^2 \bar{\chi}_b(\mathbf{q}) \bar{\phi}(\mathbf{q}, z) - \frac{\partial^2}{\partial z^2} \bar{\chi}_b(\mathbf{q}) \bar{\phi}(\mathbf{q}, z) \right) \\
\bar{\rho}_e(\mathbf{q}, z) &= -e^2 \; \bar{\phi}(\mathbf{q}) \; \frac{dn_0}{d\mu} \; g(z)
\end{aligned}
$$

So Poisson's equation in Fourier space becomes

$$\frac{\partial^2}{\partial z^2}\tilde{\phi}(\mathbf{q}, z) - q^2\tilde{\phi}(\mathbf{q}, z) = -\frac{e}{\epsilon_0}\delta(z - d) + \frac{1}{\epsilon_0}e^2\ \tilde{\phi}(\mathbf{q})\ \frac{dn_0}{d\mu}\ g(z)$$

$$+ \left(q^2\tilde{V}_b(\mathbf{q})\tilde{\phi}(\mathbf{q}, z) - \frac{\partial^2}{\partial z^2}\tilde{V}_b(\mathbf{q})\tilde{\phi}(\mathbf{q}, z)\right)$$

Rearranging terms, we have

$$\epsilon_b\left(\frac{\partial^2}{\partial z^2} - q^2\right)\tilde{\phi}(\mathbf{q}, z) = -\frac{e}{\epsilon_0}\delta(z - d) + \frac{1}{\epsilon_0}e^2\ \tilde{\phi}(\mathbf{q})\ \frac{dn_0}{d\mu}\ g(z)$$

Defining the Thomas-Fermi wavevector

$$q_{TF} = \frac{e^2}{2\ \epsilon_0\ \epsilon_b}\frac{dn_0}{d\mu}$$

we get

$$\left(\frac{\partial^2}{\partial z^2} - q^2\right)\tilde{\phi}(\mathbf{q}, z) = -\frac{e}{\epsilon_0\epsilon_b}\delta(z - d) + 2\ q_{TF}\ \tilde{\phi}(\mathbf{q})\ g(z) \qquad \text{(B.2.1)}$$

The task is to solve this differential equation for the z dependence of $\tilde{\phi}(\mathbf{q}, z)$.

Solution for a flat infinite square well

I treated the approximate case of a flat infinite square well rather than a biased finite square well, which makes analytic solutions possible.

The impurity atom is located at $d < 0$. The well potential is infinite for $z < 0$ and $z > a$ so $g(z) = 0$ in these regions. The general solutions in these regions are just superpositions of exponentials. For $0 < z < a$, $g(z)$ is finite and is given by $g(z) = \frac{2}{a}\sin^2\left(\frac{\pi z}{a}\right)$, so there is a particular solution in addition to the superpositions of exponentials.

The general solution then is

$$\tilde{\phi}(\mathbf{q}, z) = \begin{cases} Ae^{qz} & z < d \\ Be^{qz} + Ce^{-qz} & d < z < 0 \\ De^{qz} + Fe^{-qz} + \tilde{\phi}_P(\mathbf{q}, z) & 0 < z < a \\ Ge^{-qz} & a < z \end{cases}$$

where $\tilde{\phi}_P(\mathbf{q}, z)$ is the particular solution of Equation B.2.1.

Continuity of the potential at $z = d$, $z = 0$, and $z = a$ gives us

$$
\begin{aligned}
Ae^{qd} &= Be^{qd} + Ce^{-qd} \\
B + C &= D + F + \tilde{\phi}_P(\mathbf{q}, 0) \\
De^{qa} + Fe^{-qa} + \tilde{\phi}_P(\mathbf{q}, a) &= Ge^{-qa}
\end{aligned}
$$

Discontinuity of the first derivative due to the delta function at $z = d$ gives us

$$
q\left(Be^{qd} - Ce^{-qd}\right) - qAe^{qd} = -\frac{e}{\epsilon_0 \epsilon_b}
$$

Continuity of the first derivative at $z = 0$ and $z = a$ gives us

$$
\begin{aligned}
q(B - C) &= qD - qF + \tilde{\phi}'_P(\mathbf{q}, 0) \\
qDe^{qa} - qDe^{-qa} + \tilde{\phi}'_P(\mathbf{q}, a) &= -qGe^{-qa}
\end{aligned}
$$

This is easily solved in Mathematica. In the end we get for the dielectric function

$$
\tilde{\epsilon}(\mathbf{q}) = \epsilon_b \left(1 + G(q)\frac{q_{TF}}{q}\right)
$$

where $G(q)$ is a form factor given by

$$
G(q) = \frac{32\left(-1 + e^{-(aq)}\right)\pi^4 + 32\, a\, \pi^4 q + 20\, a^3\, \pi^2\, q^3 + 3\, a^5\, q^5}{\left(4\, a\, \pi^2 q + a^3\, q^3\right)^2}
$$

Appendix C

Modeling of Rabi Oscillations of Impurity States

Bryan Cole did a nice experiment to observe Rabi oscillations of impurity states in a GaAs epilayer. The sample was driven by short THz pulses $(0 - 50$ ps) sliced out of a long pulse ($\sim 1\mu s$) from the UCSB free electron laser (FEL). I did some modeling of the dynamics so that we could extract the Rabi frequency etc. from the experimental data.

In the experiment, THz pulses sliced from the FEL drove the $1s - 2p^+$ transition of the hydrogenic donors. The state of the system after absorption of a driving pulse was probed by biasing the sample and measuring the photocurrent. The integrated photocurrent is proportional to the number of carriers excited into the conduction band. At the end of the THz pulse, an impurity can be in the ground ($1s$) state, in the excited ($2p^+$) state, or ionized. Excited electrons are known to ionize within the first ns after the end of the THz pulse. The integrated photocurrent is thus proportional to the total fraction of electrons excited out of the $1s$ ground state at the end of the THz pulse.

Thus, I calculated the dynamics of an open two-level system to find the

ground state population well after an intense driving pulse. I used the density matrix formalism and included relaxation of the excited state to the ground state, dephasing of the excited state, and ionization of the excited state.

C.1   Basis

Here's the basis for the two level system:

$$|1\rangle, |2\rangle$$

These are eigenstates of the unperturbed Hamiltonian H_0.

$$
\begin{aligned}
H_0|1\rangle &= \hbar\omega_1|1\rangle \\
H_0|2\rangle &= \hbar\omega_2|2\rangle
\end{aligned}
$$

C.2   Time dependent problem

Hamiltonian:

$$H = H_0 + H'(t)$$

Density operator:

$$\rho = |\psi(t)\rangle\langle\psi(t)|$$

Time evolution:

$$\dot{\rho} = \frac{1}{i\hbar}[H, \rho] + \text{damping terms to be added later}$$

In the absence of damping, the time dependence of the density operator matrix elements is given by

$$
\begin{aligned}
\dot{\rho}_{ij} &= \langle i|\dot{\rho}|j\rangle \\
&= \frac{1}{i\hbar}\langle i|[H,\rho]|j\rangle \\
&= \frac{1}{i\hbar}[\langle i|H|1\rangle\langle 1|\rho|j\rangle + \langle i|H|2\rangle\langle 2|\rho|j\rangle - \langle i|\rho|1\rangle\langle 1|H|j\rangle - \langle i|\rho|2\rangle\langle 2|H|j\rangle]
\end{aligned}
$$

$$= \frac{1}{i\hbar} \left[H_{i1}\rho_{1j} + H_{i2}\rho_{2j} - \rho_{i1}H_{1j} - \rho_{i2}H_{2j} \right]$$

The matrix elements of the Hamiltonian are given by

$$H_{ij} = (H_0 + H')_{ij} = \hbar\omega_i\delta_{ij} + H'_{ij}$$

So here are the equations of motion of the density operator matrix elements in the absence of damping terms:

$$\dot{\rho}_{11} = \frac{i}{\hbar}H'_{21}\rho_{12} - \frac{i}{\hbar}H'_{12}\rho_{21},$$

$$\dot{\rho}_{22} = -\frac{i}{\hbar}H'_{21}\rho_{12} + \frac{i}{\hbar}H'_{12}\rho_{21},$$

$$= -\dot{\rho}_{11},$$

$$\dot{\rho}_{12} = i\,\omega_0\rho_{12} + \frac{i}{\hbar}(H'_{22} - H'_{11})\rho_{12} + \frac{i}{\hbar}H'_{12}(\rho_{11} - \rho_{22}),$$

$$\dot{\rho}_{21} = (\dot{\rho}_{12})^*,$$

where $\omega_0 = \omega_2 - \omega_1$. These are the exact equations of motion for the density matrix elements of a two-level system, in the absence of damping.

C.3 Monochromatic Driving in the Electric Dipole Approximation

In the electric dipole approximation, with the electric field $E = E_0 \cos(\omega t + \phi)$, at frequency ω, polarized in the z-direction, we have:

$$H'(t) = eE_0 z \cos(\omega t + \phi)$$

$$H'_{ij} = eE_0 z_{ij} \cos(\omega t + \phi)$$

Define

$$V_{ij} = \frac{eE_0 z_{ij}}{\hbar}$$

so that

$$\frac{H'_{ij}}{\hbar} = V_{ij}\cos(\omega t + \phi)$$

Also use the fact that $H'_{ii} = 0$. Then we have

$$
\begin{aligned}
\dot{\rho}_{11} &= iV_{21}\cos(\omega t + \phi)\rho_{12} - iV_{12}\cos(\omega t + \phi)\rho_{21}\\
\dot{\rho}_{22} &= -iV_{21}\cos(\omega t + \phi)\rho_{12} + iV_{12}\cos(\omega t + \phi)\rho_{21}\\
\dot{\rho}_{12} &= i\omega_0\rho_{12} + iV_{12}\cos(\omega t + \phi)(\rho_{11} - \rho_{22})\\
\dot{\rho}_{21} &= -i\omega_0\rho_{21} - iV_{21}\cos(\omega t + \phi)(\rho_{11} - \rho_{22})
\end{aligned}
$$

Note that, when $H' = 0$, $\dot{\rho}_{11} = \dot{\rho}_{22} = 0$, and $\dot{\rho}_{12} = i\omega_0\rho_{12}$. Therefore, ρ_{11} and ρ_{22} are constant, and $\rho_{12} = \rho_{12}(0)e^{i\omega_0 t}$. When we start driving the system at frequency ω, and we include dissipation, the part of ρ_{12} oscillating like $e^{i\omega_0 t}$ will damp out, leaving only a part oscillating like $e^{i\omega t}$.

Make a substitution here:

$$\sigma_{12} = \rho_{12}e^{-i\omega t}$$

So σ_{12} will undergo damped oscillations before approaching a steady-state value.

Then we have

$$
\begin{aligned}
\dot{\sigma}_{12} &= \dot{\rho}_{12}e^{-i\omega t} - i\omega\rho_{12}e^{-i\omega t}\\
&= \dot{\rho}_{12}e^{-i\omega t} - i\omega\sigma_{12}\\
&= -i\omega\sigma_{12} + i\omega_0\sigma_{12} + iV_{12}\cos(\omega t + \phi)e^{-i\omega t}(\rho_{11} - \rho_{22})\\
&= -i(\omega - \omega_0)\sigma_{12} + iV_{12}\cos(\omega t + \phi)e^{-i\omega t}(\rho_{11} - \rho_{22})
\end{aligned}
$$

Then the equations of motion become

$$\dot{\rho}_{11} = iV_{21}\cos(\omega t + \phi)e^{i\omega t}\sigma_{12} - iV_{12}\cos(\omega t + o)e^{-i\omega t}\sigma_{21}$$

$$\dot{\rho}_{22} = -iV_{21}\cos(\omega t + \phi)e^{i\omega t}\sigma_{12} + iV_{12}\cos(\omega t + \phi)e^{-i\omega t}\sigma_{21}$$

$$\dot{\sigma}_{12} = -i(\omega - \omega_0)\sigma_{12} + iV_{12}\cos(\omega t + o)e^{-i\omega t}(\rho_{11} - \rho_{22})$$

$$\dot{\sigma}_{21} = i(\omega - \omega_0)\sigma_{21} - iV_{21}\cos(\omega t + \phi)e^{i\omega t}(\rho_{11} - \rho_{22})$$

C.4 Relaxation, Dephasing, and Ionization

Assume a form

$$\dot{\rho}_{22} = \dot{\rho}_{22 \text{ (no damping)}} - \gamma_1\rho_{22} - \gamma_3\rho_{22}$$

$$\dot{\rho}_{11} = \dot{\rho}_{11 \text{ (no damping)}} + \gamma_1\rho_{22}$$

$$\dot{\sigma}_{12} = \dot{\sigma}_{12 \text{ (no damping)}} - \gamma_2\sigma_{12}$$

$$\dot{\sigma}_{21} = \dot{\sigma}_{21 \text{ (no damping)}} - \gamma_2\sigma_{21}$$

The parameter γ_1 is the rate of non-radiative relaxation of the impurity atom from the excited state back down to the ground state. The parameter γ_2 broadens the absorption line, so I used it to take into account both intrinsic line broadening and broadening due to sample inhomogeneities. (This is not the usual way to handle inhomogeneous broadening, though. See Reference [1].) The parameter γ_3 is the rate of ionization from the excited state into the conduction band. The equations of motion of the matrix elements of the density operator become

$$\dot{\rho}_{11} = iV_{21}\cos(\omega t + \phi)e^{i\omega t}\sigma_{12} - iV_{12}\cos(\omega t + \phi)e^{-i\omega t}\sigma_{21} + \gamma_3\rho_{22}$$

$$\dot{\rho}_{22} = -iV_{21}\cos(\omega t + \phi)e^{i\omega t}\sigma_{12} + iV_{12}\cos(\omega t + \phi)e^{-i\omega t}\sigma_{21} - \gamma_1\rho_{22} - \gamma_3\rho_{22}$$

$$\dot{\sigma}_{12} = -i(\omega - \omega_0)\sigma_{12} + iV_{12}\cos(\omega t + \phi)e^{-i\omega t}(\rho_{11} - \rho_{22}) - \gamma_2\sigma_{12}$$

$$\dot{\sigma}_{21} = i(\omega - \omega_0)\sigma_{21} - iV_{21}\cos(\omega t + \phi)e^{i\omega t}(\rho_{11} - \rho_{22}) - \gamma_2\sigma_{21}$$

C.5   The Rotating Wave Approximation (RWA)

We can obtain analytic solutions by making the following approximations:

$$
\begin{aligned}
\cos(\omega t + \phi)e^{\pm i\omega t} &= \frac{1}{2}(e^{i(\omega t+\phi)} + e^{-i(\omega t+\phi)})e^{\pm i\omega t} \\
&= \frac{1}{2}(e^{\pm i(2\omega t+\phi)} + e^{\mp i\phi}) \\
&\approx \frac{1}{2}e^{\mp i\phi}
\end{aligned}
$$

This is the rotating wave approximation. Recall in Section C.3 it was pointed out that σ_{12} goes to a constant for large t. Then the part of $\cos(\omega t + \phi)e^{\pm i\omega t}$ which is constant is a more effective driving term for σ_{12} than is the part which oscillates like $e^{\pm i2\omega t}$. The RWA throws away this other term. Another way of looking at this is to recall that ρ_{12} oscillates like $e^{i\omega t}$ for large t. Thus, the part of $\cos(\omega t + \phi)$ which oscillates like $e^{i\omega t}$ is a more effective driving term for ρ_{12} than is the part which oscillates like $e^{-i\omega t}$.

Now we just define $V \equiv V_{12}e^{i\phi}$. (Note that $V_{21} = (V_{12})^*$). The quantity $|V|$ is called the Rabi frequency. Putting this into the above form, we get

$$
\left.
\begin{aligned}
\dot{\rho}_{11} &= \tfrac{1}{2}iV\sigma_{12} - \tfrac{1}{2}iV\sigma_{21} + \gamma_1\rho_{22} \\
\dot{\rho}_{22} &= -\tfrac{1}{2}iV\sigma_{12} + \tfrac{1}{2}iV\sigma_{21} - \gamma_1\rho_{22} - \gamma_3\rho_{22} \\
\dot{\sigma}_{12} &= -i(\omega - \omega_0)\sigma_{12} + \tfrac{1}{2}iV(\rho_{11} - \rho_{22}) - \gamma_2\sigma_{12} \\
\dot{\sigma}_{21} &= i(\omega - \omega_0)\sigma_{21} - \tfrac{1}{2}iV(\rho_{11} - \rho_{22}) - \gamma_2\sigma_{21}
\end{aligned}
\right\}
\qquad \text{(C.5.1)}
$$

When we solve for the time dependence of the density matrix elements, it will be convenient to have these equations in matrix form :

$$
\begin{pmatrix} \dot{\rho}_{11} \\ \dot{\rho}_{22} \\ \dot{\sigma}_{12} \\ \dot{\sigma}_{21} \end{pmatrix}
=
\begin{pmatrix}
0 & \gamma_1 & \tfrac{1}{2}iV & -\tfrac{1}{2}iV \\
0 & -\gamma_1 - \gamma_3 & -\tfrac{1}{2}iV & \tfrac{1}{2}iV \\
\tfrac{1}{2}iV & -\tfrac{1}{2}iV & -i(\omega - \omega_0) - \gamma_2 & 0 \\
-\tfrac{1}{2}iV & \tfrac{1}{2}iV & 0 & i(\omega - \omega_0) - \gamma_2
\end{pmatrix}
\begin{pmatrix} \rho_{11} \\ \rho_{22} \\ \sigma_{12} \\ \sigma_{21} \end{pmatrix}
$$

C.6 Solutions in the RWA

This is a system of first-order ordinary differential equations with constant coefficients. We could easily take V to be imaginary, so that iV is real, and hence the coefficients are also all real. So we have the vector equation

$$\dot{\mathbf{X}} = \mathbf{AX} \qquad\qquad (C.6.1)$$

where $\mathbf{A}$ is a constant matrix whose elements are real. The theory of differential equations tells us that if λ is a distinct eigenvalue of $\mathbf{A}$ which corresponds to the eigenvector $\mathbf{E}_\lambda$, then the function $\mathbf{X}_\lambda(t) = \mathbf{E}_\lambda e^{\lambda t}$ is a solution of Equation C.6.1. The solutions obtained in this way are linearly independent (provided that the eigenvalues are all distinct, which is the case for us here). The general solution is of the form

$$\mathbf{X}(t) = \sum_{i=1}^{4} b_i \mathbf{E}_{\lambda_i} e^{\lambda_i t}$$

The components of the vector $\mathbf{X}(t)$ are the density matrix elements, for example

$$\rho_{11}(t) = (\mathbf{X}(t))_1 = \sum_{i=1}^{4} b_i (\mathbf{E}_{\lambda_i})_1 e^{\lambda_i t}$$

We want to consider the case where the driving field is turned on sharply at $t = 0$. Therefore, we take the initial conditions to be

$$\rho_{11}(0) = 1$$
$$\rho_{22}(0) = 0$$
$$\sigma_{12}(0) = 0$$
$$\sigma_{21}(0) = 0$$

The photocurrent induced by a pulse of duration τ is proportional to $1 - \rho_{11}(\tau)$.

C.6.1 Analytic solution for the resonant case

To make the problem a little easier, I only tried to find analytic solutions for the resonant case $\omega - \omega_0 = 0$, and I assumed that $\gamma_1 = 0$, which is a known to be

a very good approximation.

We find the eigenvectors and eigenvalues of $\mathbf{A}$, and solve for the parameters $\{b_i\}$ such that the initial conditions are satisfied (I did this with *Mathematica*). This gives us the $\{b_i\}$ as functions of the values of V, γ_2, and γ_3. The equation for $\rho_{11}(t)$ is thus an analytic function of the numeric values of V, γ_2, and γ_3, so I could do a curve fit to the photocurrent data to obtain these values (I did this with *Igor Pro*). The results are shown in Figure C.1.

C.6.2   Numerical solution for the nonresonant case

Although an analytic solution is possible for the nonresonant case, I didn't try to find it. In the paper, I used a curve fit for the resonant case to find the parameters V, γ_2, and γ_3, then did a numerical solution for the nonresonant case assuming that these parameters did not depend on magnetic field. The result is shown in Figure C.2.
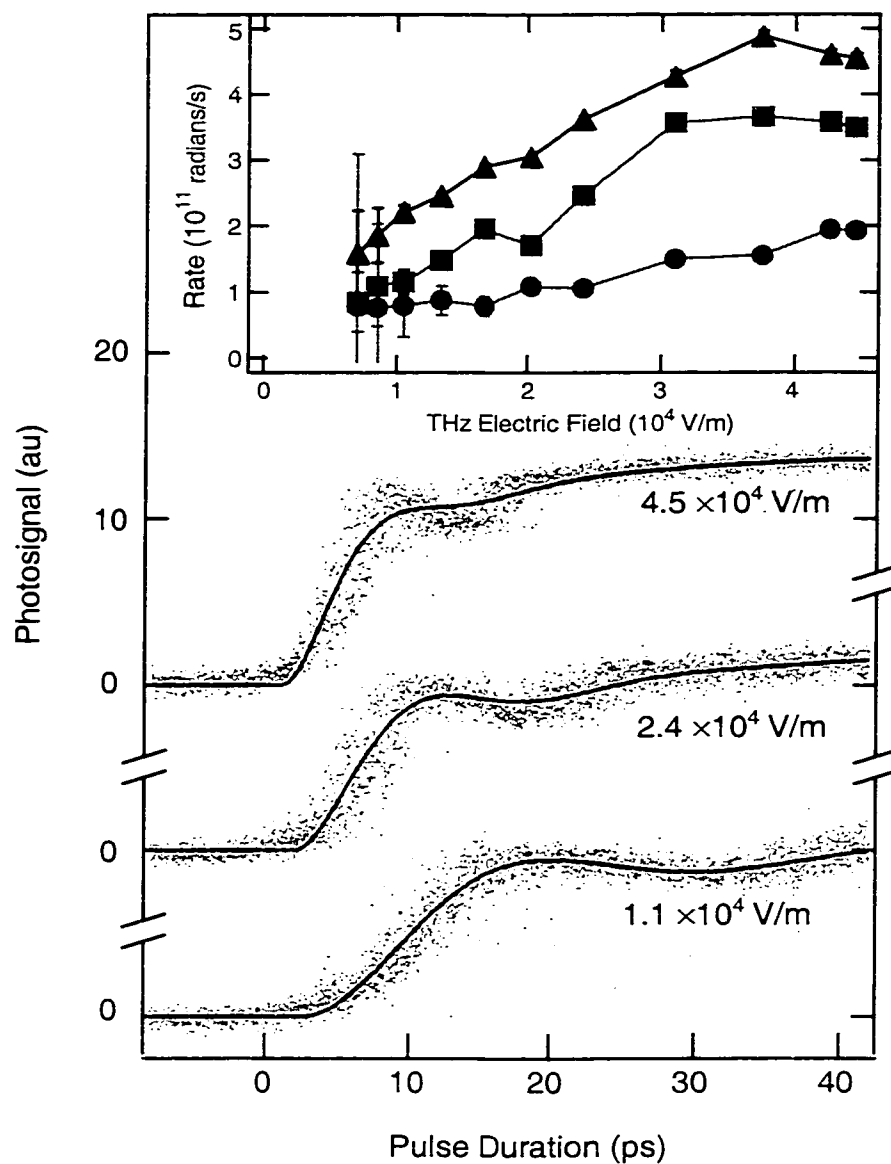
Figure C.1: Photocurrent vs. pulse duration for THz fields of 4.5, 2.4 and 1.1 ×10⁴ V/m. The plots are offset for clarity. Black lines are fits. Inset: Fit parameters vs. THz field strength: Rabi frequency V (triangles), dephasing rate γ_2 (squares), and ionization rate γ_3 (circles).
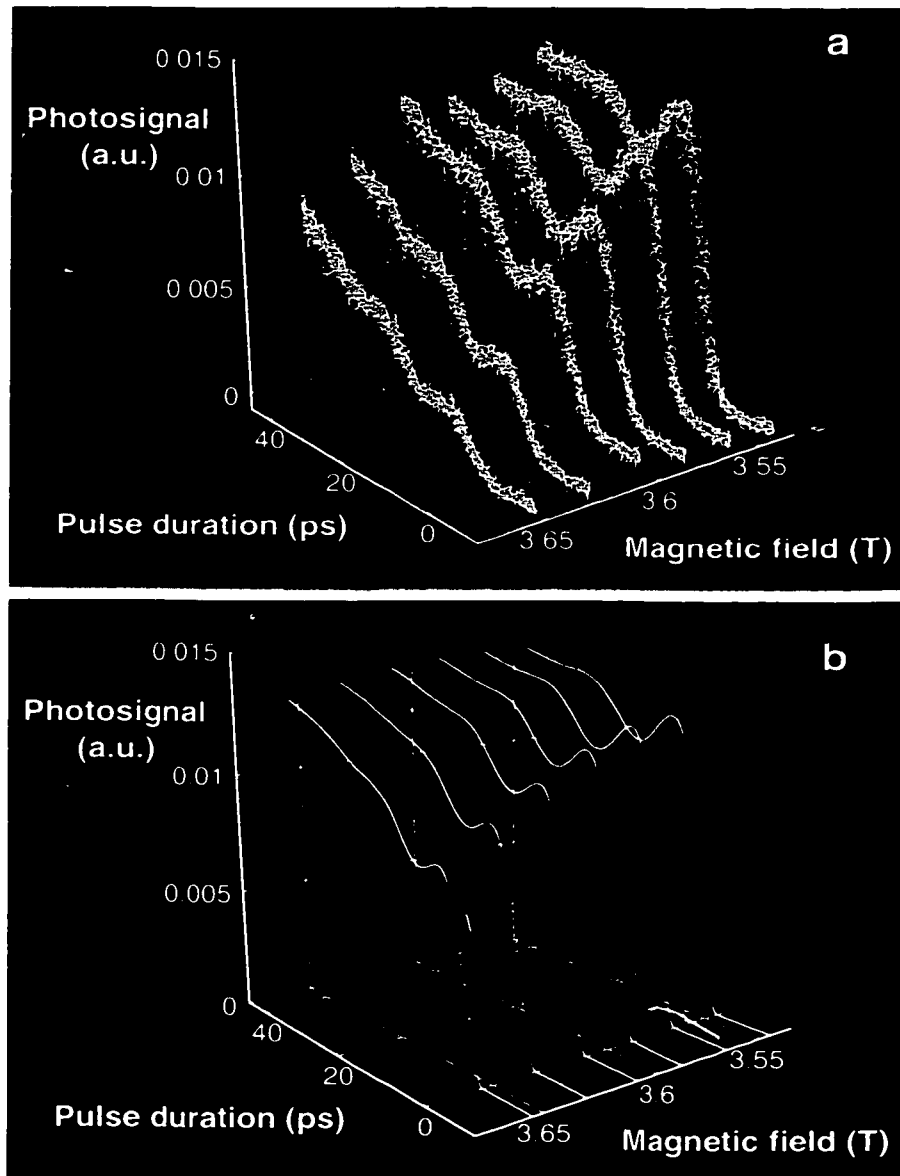
Figure C.2: a) Photocurrent data as a function of magnetic field and pulse duration, for fixed THz field strength of 2.2×10^4 V/m. The largest photosignal occurs for zero detuning, at a magnetic field of 3.54 T. The data were smoothed for this plot. b) Model calculations of the photocurrent as a function of magnetic field and pulse duration, for the same THz field strength.